

**Atmospheric Evolution of Mars Inferred from Argon
Isotopes**

by

Marek Slipski

B.S., University of Rochester, 2011

A thesis submitted to the
Faculty of the Graduate School of the
University of Colorado in partial fulfillment
of the requirements for the degree of
Doctor of Philosophy
Department of Astrophysical and Planetary Sciences

2019

This thesis entitled:
Atmospheric Evolution of Mars Inferred from Argon Isotopes
written by Marek Slipski
has been approved for the Department of Astrophysical and Planetary Sciences

Prof. Bruce Jakosky

David Brain

Shijie Zhong

Brian Toon

Paul Hayne

Date _____

The final copy of this thesis has been examined by the signatories, and we find that both the content and the form meet acceptable presentation standards of scholarly work in the above mentioned discipline.

Slipski, Marek (Ph.D., Geophysics)

Atmospheric Evolution of Mars Inferred from Argon Isotopes

Thesis directed by Prof. Bruce Jakosky

Today, Mars is a cold, dry planet with a thin atmosphere, incapable of sustaining liquid water on the surface. However, there is ample evidence that liquid water once flowed on the surface, which could have been maintained by a warmer and thicker atmosphere. The ancient atmosphere must have either been sequestered into the solid planet or lost to space. Isotopes of major atmospheric species on Mars show an enrichment of heavy isotopes relative to light ones when compared to Earth's atmosphere. Because molecular diffusion is the dominant mixing process at high altitudes, light isotopes are lost more readily from the top of the atmosphere. This thesis focuses on constraining the total amount of atmosphere that has been removed through an investigation of argon isotopes. Two main pieces make up the foundation of this work – determining the fractionation of Ar isotopes in the upper atmosphere and modeling the evolution of Ar isotopes from ancient Mars to the present-day.

To calculate the fractionation of Ar isotopes in the upper atmosphere, I derive homopause altitudes, exobase altitudes, and scale heights from densities of atmospheric species measured by the NGIMS (Neutral Gas and Ion Mass Spectrometer) instrument on the MAVEN (Mars Atmosphere and Volatile Evolution) spacecraft. The homopause is an important concept, and I show that its altitude varies in both time and space. Furthermore, I show that this variation is correlated to changes in gravity wave activity because of the role gravity wave saturation plays in generating turbulence and setting the turbopause level. The derived fractionation of ^{36}Ar and ^{38}Ar is used to estimate total atmospheric loss from Rayleigh distillation.

While Rayleigh distillation provides a useful framework for interpreting Ar isotope measurements, it is unrealistic because it considers removal of Ar from the exobase to be the only process that has altered the isotope ratio over time. By constructing a model for Ar isotope evolution

that includes all of the major sources and sinks, I provide a more thorough analysis to understand Mars' atmospheric history. The processes considered include atmospheric sputtering, outgassing of the interior and crust, and impact supply and erosion. I examine a wide range of parameter space for these time-dependent processes and illustrate how each affects the evolution of the abundances and ratios of ^{36}Ar , ^{38}Ar , and ^{40}Ar . The fractionation derived from NGIMS measurements is used to constrain the model leading to the result that 66% of all the atmospheric ^{36}Ar ever introduced into Mars' atmosphere has escaped to space. Finally, I discuss in detail what this means for loss of Mars' most abundant species, carbon dioxide.

Dedication

To Mom and Dad.

Acknowledgements

I'd like to acknowledge my advisor, Dr. Bruce Jakosky, first for his patience, but also for his support, guidance, and feedback throughout this process. His capacity to integrate subtle details while remaining focused on the big questions is remarkable and I will aim to recreate it in all my future intellectual endeavors. I am indebted to Bruce and the entire MAVEN team for such a successful (nominal?) Mars orbiter. Without their efforts this work would not have been possible.

Mom and Dad, thank you for enabling my curiosity and pushing me to reach for the stars I would not have made it here without all your love along the way. Thanks to my entire family for keeping me sharp and Vik for keeping my dougieball-hallway skills even sharper.

A multitude of people have made my time in Boulder the most transformative of my life. I'm grateful for the welcoming cast of characters that joined the APS department at the same time I did and for the friendships that flourished. Dusting off the drum kit and rocking out with the immensely talented Gluten for Punishment has been an absolute privilege. Past and present Armer inhabitants, thanks for making me feel so special. I most certainly notice when you're not around. To the entire *Jeeps* family, thank you for being the most fun, most positive, most interesting, and downright goofiest human beings I have ever encountered. I am tremendously proud to be part of the team.

Emily, thanks for pretending to let me help you with general relativity homework back in Rochester. You'll find no evidence that I knew what I was talking about in this thesis. I am so happy that you joined me in Boulder. Having you alongside for this journey, and getting to be with you for yours, has been delightful.

Contents

Chapter	
1	Introduction 1
1.1	Evidence for ancient liquid water 2
1.1.1	Geomorphic evidence for past liquid water 2
1.1.2	Mineralogical evidence for past liquid water 8
1.2	Evidence for atmospheric evolution 11
1.2.1	Volatile Inventory 13
1.2.2	Isotopes 15
1.3	Atmospheric Structure 19
1.4	Summary and Outline 22
2	Turbopause/Homopause 24
2.1	Introduction 24
2.2	Data and Methods 27
2.3	Results 41
2.4	Discussion 50
2.5	Conclusions 60
3	Fractionation of Ar isotopes in the upper atmosphere 62
3.1	Introduction 62
3.2	Data and Methods 62

3.2.1	Exobase altitudes	63
3.2.2	Scale heights	64
3.2.3	Fractionation	65
3.2.4	Rayleigh distillation	68
3.3	Results and discussion	70
3.4	Summary and conclusions	78
4	Argon Isotope Evolution Model	79
4.1	Introduction	79
4.2	Model	82
4.2.1	Mantle reservoir and processes	85
4.2.2	Crustal erosion	89
4.2.3	Atmospheric reservoir and associated processes	90
4.3	Results	98
4.3.1	Comparing individual processes	100
4.3.2	Combining processes	103
4.3.3	Constraining the parameter space	107
4.4	Varying the fractionation factor	112
4.5	Discussion and conclusions	113
4.5.1	Sputtering	115
4.5.2	Outgassing of the mantle and crust	116
4.5.3	Early $^{40}\text{Ar}/^{36}\text{Ar}$ values	117
4.5.4	Impacts	119
4.5.5	Early atmospheric pressure	119
4.5.6	“Restored” $^{40}\text{Ar}/^{36}\text{Ar}$ value	122
5	Summary	125

Bibliography

Tables

Table

1.1	Isotope ratios of major atmospheric species on Earth and Mars	16
2.1	Season, location and wave-turbopause altitudes for each month	34
4.1	Ar isotope measurements	80
4.2	Ar isotope box model reservoirs and initial conditions	84
4.3	Ar isotope box model results	108

Figures

Figure

1.1	Mars valley network	4
1.2	Kasei Valles	6
1.3	Eberswalde Crater	7
1.4	“Blueberries” on Mars	10
1.5	Mineralogical epochs of Mars	12
1.6	Reservoirs of Martian volatiles	18
1.7	Thermal structure of Mars’ atmosphere	20
2.1	NGIMS latitude and local time coverage Feb 2015 - Dec 2016	29
2.2	Alitude profiles of CO ₂ , N ₂ , and Ar densities and N ₂ /Ar	31
2.3	Temperature, N^2 , and variability profiles for June 2016	33
2.4	Temperature, N^2 , and variability for each month	42
2.5	Homopause and wave-turbopause altitudes as a function of time	45
2.6	Comparison of homopause altitudes and homopause CO ₂ densities	47
2.7	Turbopause altitudes as a function of time	48
2.8	Monthly averaged temperature standard deviation profiles with high N^2 and low D_{mol}	51
2.9	Homopause altitudes and CO ₂ densities as a function of latitude, local time, and season	53
2.10	Seasonal variability of temperature, standard deviations, N^2 observed by MCS	56

3.1	$^{36}\text{Ar}/^{38}\text{Ar}$ altitude profile measured during deep dip 4	67
3.2	Rayleigh distillation loss values as a function of fractionation factor	69
3.3	Exobase altitude method comparison	71
3.4	Homopause and Exobase altitudes	72
3.5	Scale height temperatures from Ar, CO ₂ , N ₂	74
3.6	$^{36}\text{Ar}/^{38}\text{Ar}$ fractionation values	75
3.7	Variability of exobase altitudes, homopause altitudes, separation distances, and scale heights wit solar zenith angle	77
4.1	Diagram of Ar isotope box model reservoirs and exchange pathways	83
4.2	Models of crustal production evolution	87
4.3	Estimates of CO ₂ loss due to sputtering extrapolated to past epochs	94
4.4	Atmospheric gain and loss due to impactors during the Late Heavy Bombardment	99
4.5	Evolution of ^{36}Ar , $^{36}\text{Ar}/^{38}\text{Ar}$, and $^{40}\text{Ar}/^{36}\text{Ar}$ for isolated processes	101
4.6	Evolution of ^{36}Ar , $^{36}\text{Ar}/^{38}\text{Ar}$, and $^{40}\text{Ar}/^{36}\text{Ar}$ due to sputtering for variable s_f and P_0	104
4.7	Evolution of ^{36}Ar , $^{36}\text{Ar}/^{38}\text{Ar}$, and $^{40}\text{Ar}/^{36}\text{Ar}$ including all processes	106
4.8	Resulting $^{36}\text{Ar}/^{38}\text{Ar}$ as a function of v_f for different s_f	111
4.9	Percentage of total ^{36}Ar loss for various observed $\Delta z/T$ values	114
4.10	Integrated total and sputtered CO ₂ consistent with Ar isotopes	121
4.11	Observed and modeled “Restored” values of $^{40}\text{Ar}/^{36}\text{Ar}$	123

Chapter 1

Introduction

Are humans alone in the universe? Or do lifeforms, unicellular or sentient, exist elsewhere in the cosmos? Such questions remain unanswered, but we know of so many worlds to further explore to seek answers — from Earth-sized rocky exoplanets, to the subsurface oceans of Europa and Enceladus, and the ethane-rich lakes on Titan. No list would be complete, however, without Mars. Even with a rich history of observations, orbiter missions, landers, and rovers, arguments continue about whether Mars hosts extant microbial life in the subsurface today and if any life it might once have hosted early in its history is now extinct. The proposition that Mars could have sustained life in the past rests on the idea that early Mars' climate was much different than it is today.

There is substantial evidence that Mars was a habitable planet 4 billion years ago — namely, that the surface is teeming with features indicative of water, an essential ingredient for life. Only a thin atmosphere remains today, but for liquid water to have once flowed for a long time, a thicker warmer atmosphere must have been present. If a thick early atmosphere existed, much of that gas has been removed; either it has been sequestered in the rocks that make up the planet or it has escaped from the highest altitudes into space. Understanding how strong these processes were and how they changed the atmosphere can help us better assess the conditions of an early habitable Mars. Specifically, the driving question behind this work is: how much of Mars' atmosphere was lost to space throughout its history?

What follows is an effort to quantify the loss to space of Mars' early atmosphere, using the

gas argon as a tracer for the atmosphere as a whole. This entails an investigation of the structure of the middle and uppermost layers of the atmosphere, interpretation of Ar measurements throughout the atmosphere and from meteorites, and modeling the fundamental physical processes that have supplied and removed gas from the atmosphere over time. In the end, this work enhances our ability to understand how Mars' atmosphere has evolved since the planet's formation.

The introduction presents the motivation behind the work contained in this thesis. It begins with a review of the critical lines of evidence pointing to past liquid water on Mars (Section 1.1). A detailed discussion of the evidence for climatological change follows which covers the isotope ratios of gases in Mars' atmosphere (Section 1.2) — the key insight utilized in this thesis to quantify atmospheric loss. I also present the basic vertical structure of the present-day Martian atmosphere (Section 1.3). Finally, I briefly summarize the foundational principles laid out in this chapter and describe the forthcoming chapters (Section 1.4).

1.1 Evidence for ancient liquid water

Water is a crucial ingredient for life, so it has fueled studies of Mars since the first observations of the polar ice caps (and what were thought to be irrigated canals) through the strategy of NASA's Mars Exploration Program: "Follow the water."¹ Because of the low surface temperature and pressure, water cannot exist for extended periods on Mars' surface today. However, there is ever-accumulating evidence that water was prevalent on Mars early in its history. Below I review some of the observations that strongly support this hypotheses, though this is by no means comprehensive.

1.1.1 Geomorphic evidence for past liquid water

Mapping of Mars began in earnest during close approaches between Earth and Mars in the 1800s and continued as telescopes improved. But it was not until images of the surface were beamed back from spacecraft and rocks were examined by landers that an understanding of the geologic

¹ The current Mars Exploration Program strategy is "Seek signs of life," with the Curiosity rover being a bridge between the two strategies.

history was possible. I focus on several discoveries from these missions of the ways in which water has affected the geology of the planet.

Of course, the geology of Mars has not been influenced solely by water – the surface is covered with craters formed from collisions with impactors over billions of years, volcanoes that were once active, and canyons formed from tectonic processes. While I will not describe those features further, it is necessary to introduce the standard geologic periods that have been inferred from the crater densities across the surface. The Amazonian² period extends from the present day to 3 Gyr (billion years) in the past. These regions have few craters and sparse evidence for water. The moderate density of craters in Hesperian period regions correspond to ages of 3 – 3.7 Gyr ago. The Noachian period, 3.7 – 4.1 Gyr, consists of regions that are the most densely packed with craters and also most of the water-derived features. The geologic record of the period prior to the Noachian (pre-Noachian, 4.1 – 4.5 Gyr) has largely been erased, but it corresponds to the global dichotomy³ (Hartmann, 1973) and regions like Hellas basin, upon which Noachian surfaces are seen (Carr and Head, 2010).

Valley networks, incised branching channels, are abundant across the southern highlands of Mars (typically about 100 m deep, 1 km wide, and 10-100 km long). The floors and walls of these channels show evidence of large-scale fluid flow, consistent with water and sediment (Baker, 2001). An example is shown in Fig. 1.1. They resemble drainage basins on Earth, which are areas where water from precipitation runs downslope and collects into a common pool or channel. It is widely believed, due to their number and extent, that these networks were formed by precipitation and surface runoff. Most are dated to the Noachian epoch, though some could have been formed into the Amazonian (Hynek et al., 2010).

In addition to valley networks, larger erosion features called outflow channels appear across

² The names of these periods refer to specific regions that correspond to that period. For instance, the Amazonian period is named after Amazonis Planitia, a smooth, 100 million year old surface. While "Amazonian" may conjure an image of a wet environment (the name dates back to the early days of Mars mapping), the recency of the lava flow that covers this region has left it devoid of evidence of past water

³ The northern hemisphere is low in elevation ("lowlands"), has a thin crust, and is relatively flat, while the southern hemisphere is about 3 km higher ("highlands") and has a thick crust. Both endogenic — plate tectonics (Sleep, 1994) and degree-1 mantle convection (Zhong and Zuber, 2001) — and exogenic — one (Wilhelms and Squyres, 1984) or more (Frey and Schultz, 1988) impacts — have been proposed.

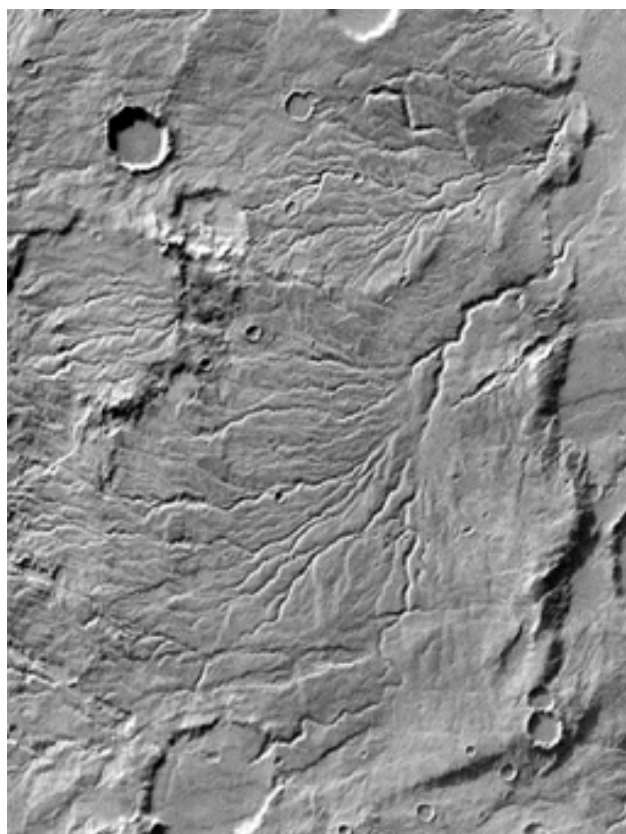


Figure 1.1: An example of a valley network on Mars. Credit: NASA/JPL-Caltech.

the Martian terrain. An example is shown in Fig. 1.2. Outflows were likely caused by the release of water from subsurface aquifers⁴ during episodic events such as impacts or magmatic activity (Carr, 1979; Rodriguez et al., 2005). Catastrophic flooding from these aquifers ensued leading to wide and extensive channels. Most are younger than the valley networks, dating to the Hesperian epoch.

A consequence of stable water on a surface pockmarked with craters is the creation of crater lakes. In fact, past lakes are observed across Mars' surface (Cabrol and Grin, 1999), many fed by valley networks active during the Noachian (Fassett and Head, 2008). Many craters have what appear to be inlet channels from regional valley networks that breach crater rims before terminating. Water from these channels would have begun to fill the craters, creating a lacustrine environment. Some, likely did not amass enough water to cause flow out of the crater (closed-basin lakes, see Fig. 1.3), while others (open basins) show a breached rim corresponding to an outlet in addition to the inlet. Observations from Curiosity corroborate the geochemical evidence (discussed in the next section) that Gale Crater once held water.

The termination of the inlet channel into Eberswalde crater in Fig. 1.3 shows another geomorphic feature indicative of past water on Mars — a delta. Deltas are formed when flowing water terminates in a reservoir of water. The sediment carried by the water is deposited at the entrance in a fan-like shape. This is further evidence that craters such as Eberswalde contained a lake. The resemblance to deltas on Earth is striking, though the timescale for formation of the delta remains debated — some suspect fluid flowed for decades or centuries, while others assert that it may have taken hundreds of millennia (Baker, 2006).

The extensively cratered southern highlands on Mars are reminiscent of the Moon and Mercury, but many craters on Mars are significantly different. The rims of many have been cut by channels, their walls on the inside have been eroded, and their floors are relatively flat. Each of these is consistent with fluvial erosion (Barlow, 2008). Crater infilling can result from volcanism, aeolian

⁴ Originally explained by a global hydrosphere in the megaregolith, the ice is now thought that aquifers existed in buried impact craters or impact-fractured rocks (Rodriguez et al., 2015).

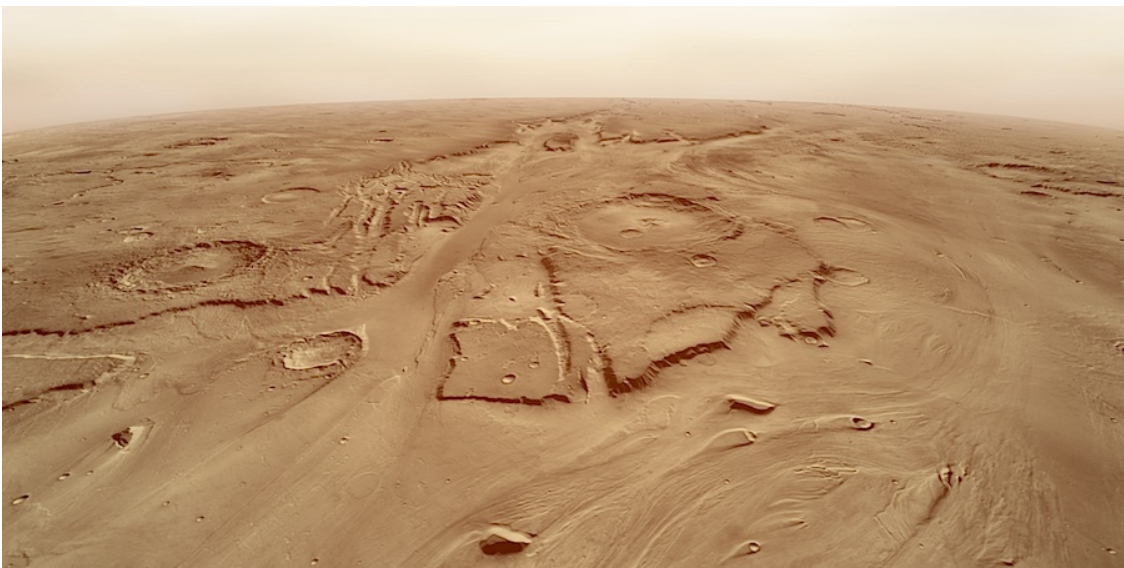


Figure 1.2: The largest outflow channel systems on Mars, Kasei Valles. It is around 2000 km long, 400 km wide, and 2.5 km deep. Credit: NASA/JPL-Caltech/Arizona State.

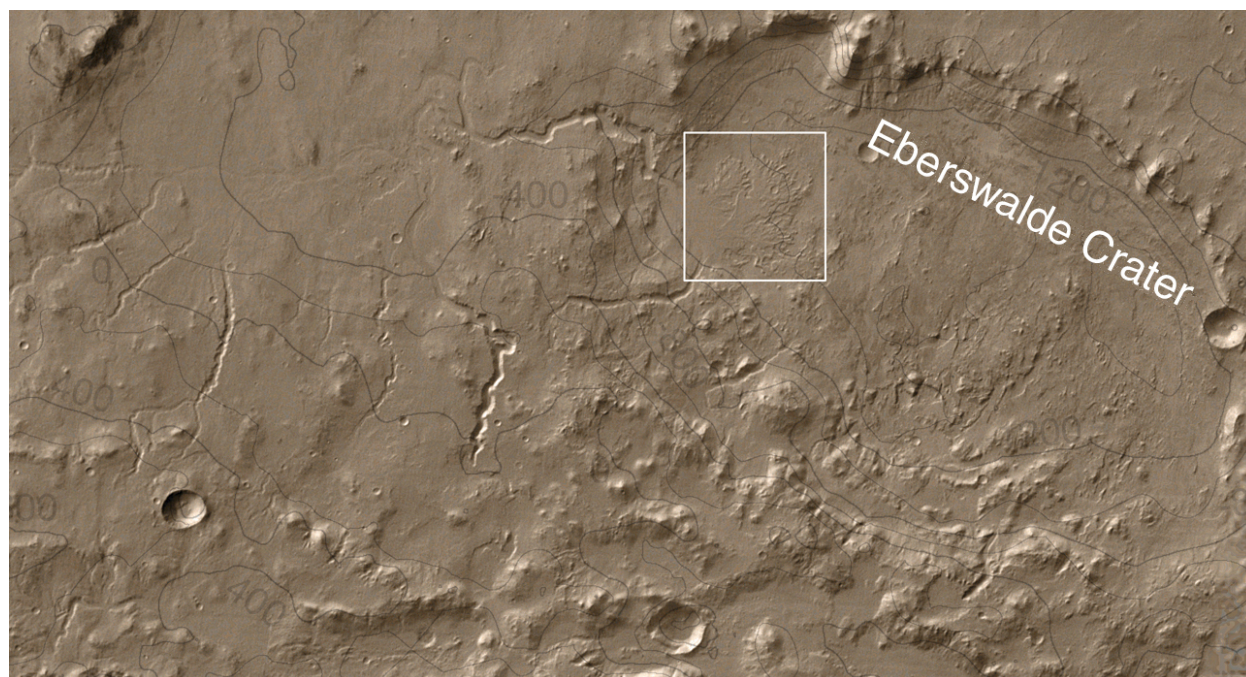


Figure 1.3: Eberswalde Crater, with elevation contours in meters. The craters inlet valley can be seen at the top left of the crater and the alluvial fan deposits from inflowing water are boxed in white. Credit: NASA/JPL/Malin Space Science Systems.

processes, and ejecta from nearby impacts, but the global morphology as well as crater degradation modeling suggests fluvial processes dominated (Craddock and Howard, 2002; Forsberg-Taylor et al., 2004; Irwin et al., 2013). Indeed, erosion rates during the Noachian appear to have been much greater than throughout most of Mars' history (Golombek et al., 2006).

Though controversial, some authors have proposed the existence of an ancient ocean. The northern hemisphere is lower in elevation and free of craters, distinct from the southern highlands, and contains sediment. The contact between them has been interpreted as the shoreline of an ocean (Parker et al., 1993). However, there are vertical variations along the proposed shoreline that are inconsistent with an ocean and the shoreline is more difficult to recognize with more recent imagery (Wordsworth, 2016). The debate continues, as Rodriguez et al. (2016) have argued that lobe features near the shoreline can be explained by deposits from tsunamis that occurred while the ocean was present.

1.1.2 Mineralogical evidence for past liquid water

The geomorphic features are examples of how past water quite literally shaped the surface of Mars, physically carving channels and depositing carried sediment. But, chemical changes to the composition of the rocks with which water interacted have been preserved. These have been observed not only from in-situ sampling by landers and rovers, but also spectroscopically from orbit. In addition to furthering the case for ancient water, they provide insight into the types of environments that existed on early Mars.

Phyllosilicates, clay minerals, have been observed in regions across the planet. The OH or H₂O in the chemical structure of these minerals necessitates the presence of water for formation. They are most widely seen (detections number in the thousands) in Noachian surfaces (Ehlmann and Edwards, 2014). The breadth of locations containing phyllosilicates suggests that water was not restricted to specific locations, but global in extent.

The abundance of observed clays is an indication of ancient water, but it is not unambiguous evidence that early Mars was warm and wet. The clays could have formed in the subsurface and

later been exposed via erosion (Ehlmann et al., 2011). However, in some regions, the stratigraphy is reminiscent of common Earth environments; kaolinite (an aluminum-rich clay) is observed in layers directly above Fe/Mg clays. This can be explained by leaching, a process that transports ions (in this case, Fe and Mg ions) downward. The topmost layers become depleted in Fe and Mg, enabling Al clays to form above and Fe/Mg clays below (Bishop et al., 2008). On Earth, this sequence is seen primarily in wet — particularly, high precipitation — environments (McKeown et al., 2009; Carter et al., 2015).

The observations of carbonates on the surface present a conundrum. They have been observed spectroscopically, e.g. Ehlmann et al. (2008), and by the Spirit Rover (Morris et al., 2010). If surface water was widespread and a warm climate persisted, carbonates should have readily formed from water-rock interactions, given the presumed large abundance of CO₂ in the atmosphere. However, they are not nearly as pervasive across the surface as phyllosilicates. One possible explanation is that, as mentioned above, the water responsible for phyllosilicate formation was mostly in the subsurface such that the CO₂ in the atmosphere was unable to interact with it. Or, the aqueous environments could have precluded carbonate formation due to, for example, acidic conditions (Ehlmann and Edwards, 2014). Carbonates are observed in outcrops of the deep crust, suggesting that the carbon-silicate cycle was active on early Mars and that the crust may still contain a large fraction of Mars’ carbon inventory (Michalski and Niles, 2010).

The crater lakes discussed in the last section also have mineralogies consistent with lacustrine environments. They contain phyllosilicates like the surrounding surface, but also salts, chlorides, and sulfates that likely precipitated out of the lakes (Ehlmann and Edwards, 2014). Their variation between locations may indicate different water chemistries (Ehlmann et al., 2016). Hematite spherules (“blueberries”) observed by the Opportunity rover (Fig. 1.4) could have been formed from acidic groundwater interacting with iron-rich minerals. They are thought to be examples of concretions — spherical objects compositionally distinct from the surrounding material that precipitated out of solution — which suggest an origin from flowing groundwater.

Different mineralogies dated to different geologic periods imply that the dominant surface

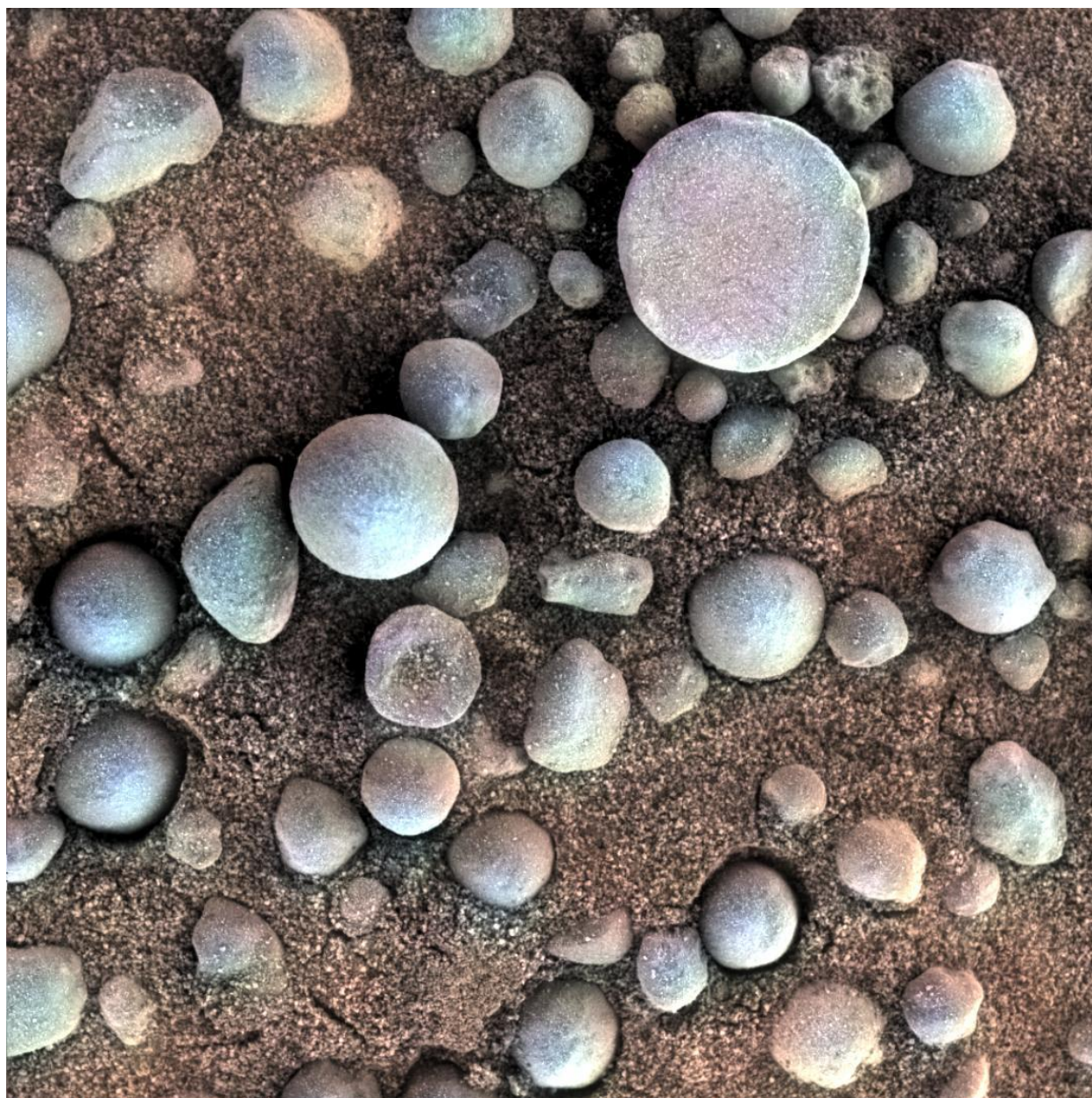


Figure 1.4: Image from Opportunity of hematite-spherules. The length of the region shown is 3 cm across. Credit: NASA/JPL-Caltech/Cornell/USGS.

conditions evolved over time. This prompted an alternative naming convention (shown in Fig. 1.5) for the epochs of Mars based on the mineralogy instead of the geomorphology (Bibring et al., 2006). The earliest period is termed the “phyllosian,” because of the widespread phyllosilicates throughout this terrain. The acidic environments inferred from sulfates observed in slightly younger units represent the “theikian.” The Siderikan (< 3.5 Gya) is dominated by a mineralogy of anhydrous Fe-oxides due to they dry arid environment that persisted after the surface lost its water.

There is an abundance of evidence for water in the past, but most is limited to early Mars (Noachian and Hesperian). Amazonian units tend not to have valley networks or other geomorphic evidence and do not show mineralogies of aqueous alteration, suggesting that water has been largely absent from Mars for the last 3 billion years. So where did the water go? What caused the aqueous activity to stop? While there may be some localized processes which involve surface water today, widespread liquid water cannot exist because of the cold, thin atmosphere. However, we need not accept that the atmosphere has changed significantly from the past based on water alone. In the next section we review some of the main clues pointing to a transition of the atmosphere from when water was widespread to today.

1.2 Evidence for atmospheric evolution

While observations of the surface have enabled a robust conclusion about the past presence of water, they provide less insight into the atmospheric conditions necessary for water to have flowed.⁵ Likewise, the thickness and composition of the ancient atmosphere cannot be gleaned from the geologic record. Further complicating the problem is the oft-cited faint young sun problem (Sagan and Mullen, 1972); the lower luminosity of the Sun early in our solar system’s history leaves ancient Mars with about 3/4 of the solar flux it receives today. This implies that the early atmospheric composition and pressure must have been very different. Several greenhouse warming mechanisms have been proposed that could have generated temperatures above freezing in the past

⁵ That is, those features could not have been formed under present Martian atmospheric conditions. Anders and Owen (1977) called the confirmation of the < 10 mb atmosphere “one of the greatest disappointments of the space age.”

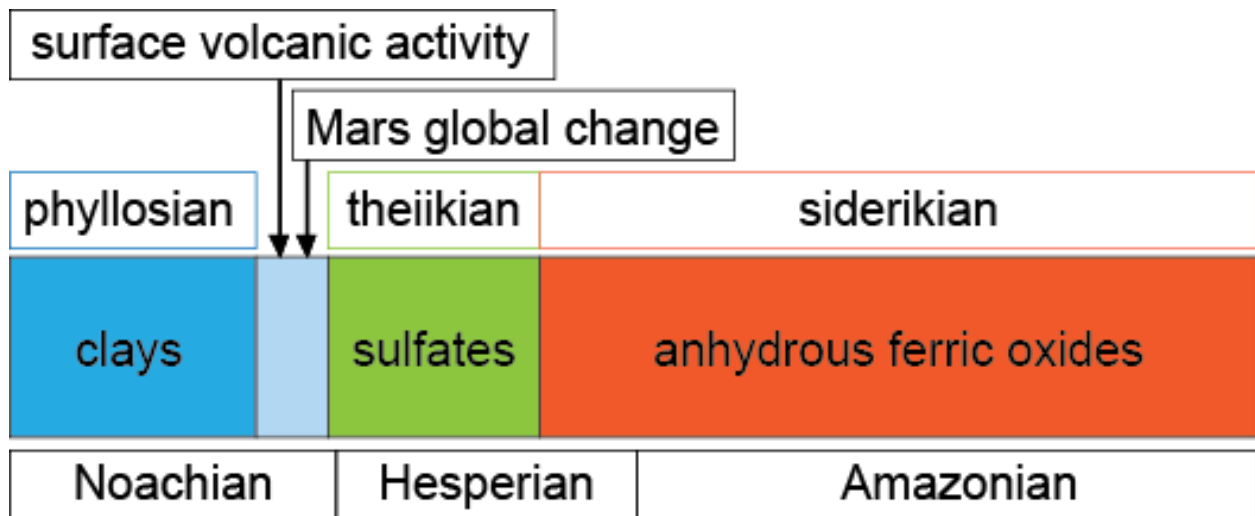


Figure 1.5: Timeline of Mars based on the mineralogical record, and the corresponding geologic periods. Credit: (Bibring et al., 2006).

(Pollack et al., 1987; Johnson et al., 2008; Ramirez et al., 2014). However, none can fully explain the warming, the rainfall production, the sources of required gases, and be sufficiently long-lived (Haberle et al., 2017). Debate continues over whether the observed fluvial features were formed during several hundred million years of warm conditions or shorter transient warm periods generated by large impacts (Segura et al., 2002). Without further exploring the various theories about the composition and stability of the early atmosphere, what evidence (outside of water features) is there that the atmosphere really was different?

1.2.1 Volatile Inventory

A bit of comparative planetology is a fine jumping off point for thinking about the evolution of Mars' atmosphere. The three terrestrial planets all have atmospheres, but show substantial differences in pressure, temperature, and composition. Venus's atmosphere is 90 times thicker than Earth's and more than twice as hot (Basilevsky and Head, 2003). The pressure on Mars is only 6 mbar compared to 1 bar on Earth and the temperature is about 70 K colder on average (Barlow, 2008). Though Mars' atmosphere is the thinnest and coldest and Venus's is the hottest and thickest, they are both about 95% CO₂ and 2% N₂. Here, Earth is the outlier, made up of 78% N₂ and 20% O₂.

The lack of CO₂ in Earth's atmosphere can be attributed to the carbon-silicate cycle. CO₂ is delivered to the atmosphere through volcanic outgassing, falls to the surface as carbonic acid, becomes locked up in rock as carbonate, and returns to the mantle through plate subduction. Accounting for the CO₂ estimated to be stored in carbonate rock and in the mantle of Earth one finds it has a total inventory of 90 bar, nearly equal that of Venus (Sleep and Zahnle, 2001). As a fraction of the total planetary mass, that is about 6×10^{-5} . Mars' mass fraction of CO₂ is estimated only to be 10^{-6} .

N₂ provides a similar story — it makes up a large part of Earth's atmospheric composition due to the lack of CO₂. As a fraction of planet mass, Earth and Venus have a similar amount while Mars has much less (10^{-6} and 10^{-10} , respectively; Bland et al. (2004)). Water content in

the mantles in the terrestrial planets and in the polar caps of Mars are more difficult to measure, but one thing seems clear: Venus and Mars are both depleted relative to Earth. Venus likely lost most of its water through a runaway greenhouse effect in which H was removed, but heavier species were not. For Mars, these depletions in condensible gases are not a smoking gun, but they do point toward an evolution in which volatile loss from the atmosphere was important.

A similar analysis of the noble gas abundances, though once expected to be straightforward, is fairly complicated. As with the other volatiles, estimating the total inventory in the interior of the planets is difficult because of the paucity of samples. In addition, the noble gases may contain remnant signatures of a combination of the primary atmosphere, the escape of that atmosphere, and the secondary outgassed atmosphere. The total abundances of Kr and Xe in the atmospheres of Venus, Earth and Mars relative to solar abundances are depleted with respect to the “planetary” signature (carbonaceous chondrites). Earth and Mars, but not Venus, are also depleted in Ne and Ar (Anders and Owen, 1977; Zahnle, 1993; Pepin, 2006). On Earth, these depletions are unlikely to be due to a large undegassed mantle reservoir because recent estimates suggest >95% of all Earth’s ^{36}Ar is in the atmosphere (Halliday, 2013). Thus, the depletion in noble gases could have been caused by early outgassing into the atmosphere and subsequent early loss through hydrodynamic escape — a process where intense EUV radiation drives an outflow of H atoms strong enough to carry heavier atoms. Whether the depletion in Mars’ atmosphere is a result of early catastrophic outgassing and hydrodynamic escape or due to retention of noble gases in the mantle remains ambiguous. But, the orders of magnitude depletion in all atmospheric noble gases as a fraction of Mars’ mass, in combination with the low abundances of H, C and N strongly point toward loss of the secondary atmosphere to space. Though the total inventories of noble gases do not tell an unambiguous story, we will see in the next section that the isotopes of Ar are more indicative of loss, which we will explore throughout this thesis.

1.2.2 Isotopes

Just as we saw that the inventories of gases across different bodies suggest Mars' atmosphere has changed, so too do the isotopes of those gases. Isotopes of a given element behave quite similarly, but the difference in masses due to additional neutrons in their nuclei can have consequences. If a mass-dependent process adds or removes some volatile to or from a reservoir, the ratio of isotopes in that reservoir will deviate from the initial value. A common example of fractionation is the depletion of heavy H and O in an air mass as it moves poleward from low latitudes on Earth. Water vapor above the ocean surface is fractionated in equilibrium with water. Light isotopes are preferentially moved from the liquid to the vapor phase, such that the warm vapor that rises at low latitudes is depleted in D and ^{18}O . As the air cools, water condenses to form clouds and the liquid is enriched in heavy isotopes (equilibrium fractionation from condensation favors heavy isotopes). Thus, the air mass after precipitation is further depleted in heavy isotopes. As it continues to move poleward, precipitation removes more and more heavy isotopes. This process produces isotope ratios in bodies of water that are latitude-dependent; water near the equator is isotopically heavy and water near the poles is isotopically light (Joussaume et al., 1984).⁶ The focus here will be on the isotopes of main volatiles in Mars' atmosphere compared to Earth's.

As we saw in the last section, the volatile inventories of Venus, Earth, and Mars contain similar mass-fractions of CO_2 , N_2 , and Ar, though Mars is somewhat depleted. Those abundances are similar because the atmospheres are largely a product of outgassing of their interiors and the delivery of gas from comets and asteroids. Because the terrestrial planets formed in a similar region of the solar system, the compositions of their interiors and thus their atmospheres should be similar. This means that the isotope ratios of the initial reservoirs of gases across the planets should have also been the same. Earth's atmospheric H, N, and Ar isotope ratios are nearly identical to ratios found in chondrites, the building blocks of the planets. That is, no mass-dependent processes that affected these isotope ratios have been significant during Earth's history. The isotopic record

⁶ Because this process is temperature dependent, paleoclimate temperatures can be reconstructed from O isotope ratios in ice cores (Jouzel et al., 1983).

Table 1.1: Isotope ratios of major atmospheric species on Earth and Mars. References: Earth H and O are Vienna Standard Mean Ocean Water (VSMOW) values, C is from the Vienna Pee Dee Belamnite (V-PDB) (Kendall and Caldwell, 1998), and N and Ar are from air (Coplen et al., 2002; Lee et al., 2006). All Mars isotope ratio measurements are of the present-day atmosphere made from the Sample Analysis at Mars (SAM) instrument onboard the Curiosity rover (Webster et al., 2013; Mahaffy et al., 2013; Atreya et al., 2013).

Ratio	Mars atmosphere	Earth	Mars/Earth
D/H	9.268×10^{-4}	1.5576×10^{-4}	5.95
$^{13}\text{C}/^{12}\text{C}$	0.012	0.0112	1.07
$^{15}\text{N}/^{14}\text{N}$	0.00578	0.003676	1.57
$^{18}\text{O}/^{16}\text{O}$	0.0021	0.0020052	1.05
$^{38}\text{Ar}/^{36}\text{Ar}$	0.24	0.1885	1.26

implanted in Mars' atmosphere and in Martian meteorites indicate a significant departure from the initial state, however. Isotope ratios of Mars' major atmospheric species are listed in Table 1.1. For each ratio, Mars' atmosphere is enriched in the heavy isotope relative to Earth's atmosphere.

There have surely been a host of processes that have shaped the atmospheric inventory and isotope record throughout Mars' history. Fig. 1.6 from Jakosky and Jones (1997) illustrates the different reservoirs and exchange pathways for volatiles. For example, carbonate formation would have preferentially removed ^{13}C from the atmosphere and condensation or deposition of water can more readily take out D and ^{18}O . The trapping of H and CO_2 in the poles could have happened slowly, preferentially removing heavy isotopes, or rapidly such that it contains isotope ratios of the atmosphere of some past time. Adsorption today pulls atmospheric water vapor out of the atmosphere and stores it in the subsurface. However, those processes would have depleted H, C, and O in heavy isotopes. The cratered surface is evidence that impactors with isotope inventories of the early solar system have delivered gases to the atmosphere, acting to partially reset any changes from the initial isotope inventory. The violent collisions of those impacts, depending on their magnitude, can also remove a significant amount of gas.

And yet, the most straightforward interpretation of the enrichment in all the major species is loss to space. Loss to space preferentially removes light isotopes from the atmosphere. H is lost more readily than D through Jeans escape due to its lower mass. In addition, the dominant mixing process at high altitudes is molecular diffusion. Molecular diffusion is mass-dependent and it enhances the upper atmosphere in light isotopes. Each of the atmospheric species in Table 1.1 has been subject to different atmospheric loss processes, but because of the diffusive separation of species all will act on a region of the atmosphere depleted in heavy isotopes.

So how much atmosphere has been lost based on the isotopes? One must aggregate the effects of all processes that have altered the atmosphere from its original state. Complicating the matter, each process's importance has certainly changed throughout Mars' history as well. Outgassing from the interior was likely strong very early due to a large heat flux from the interior. Impacts that rained down throughout the Late Heavy Bombardment are extremely rare today (Ivanov, 2001;

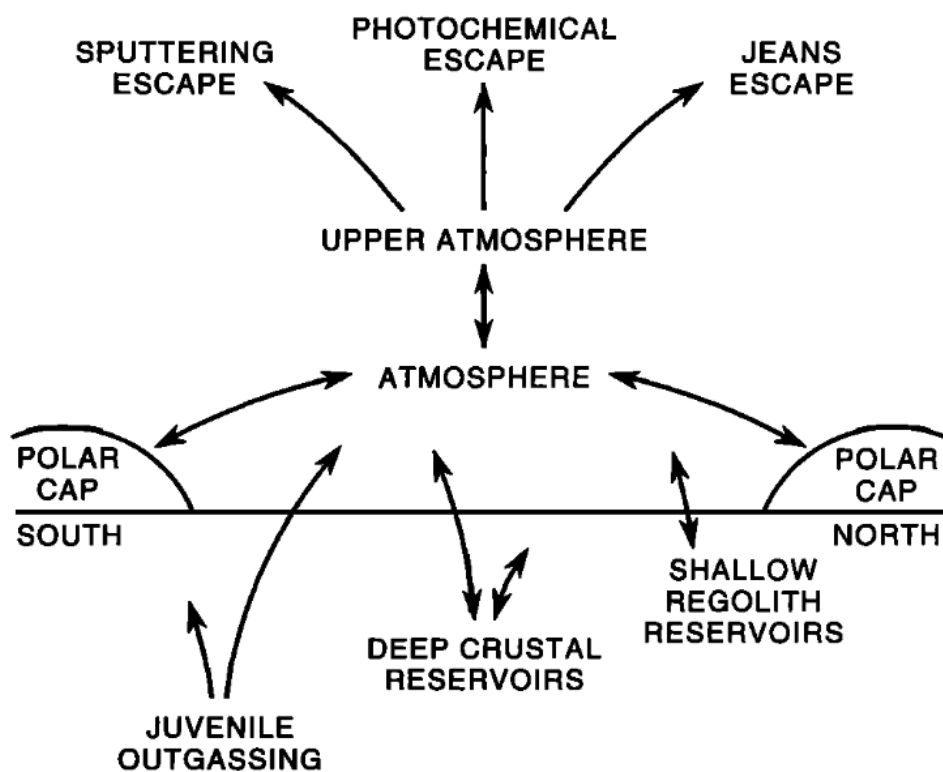


Figure 1.6: Various reservoirs of Martian volatiles and processes that can supply or remove them from the atmosphere. Credit: (Jakosky and Jones, 1997).

Malin et al., 2006). The polar caps' stability depends on the planet's obliquity, which varies on $\sim 50\text{--}100$ Myr timescales (Laskar et al., 2004). Escape to space was stronger early in history when the solar wind and EUV were more intense. EUV intensity was about 2.5 times the present value 2.5 billion years ago and 6 times the present value 3.5 billion years ago (Ribas et al., 2005). Because there is so much uncertainty in the magnitude of planetary scale processes billions of years ago, attempting to model each adds another dial with little constraint.

However, the complexity of the problem is somewhat alleviated for Ar compared to H, C, O, and N because as a noble gas, the available exchange pathways are limited. That is, Ar is chemically inert and non-condensable. While it can be ionized, it is not involved in photochemical cycles. It is not deposited onto the surface on seasonal timescales, and it is relatively heavy making significant loss through Jeans or photochemical escape unrealistic. The main (possibly only) processes driving changes in Ar isotope ratios are degassing of the interior, impacts, and escape to space through sputtering. Thus, Ar is well-suited to study atmospheric evolution as relatively few major processes must be considered.

1.3 Atmospheric Structure

Before concluding this section, a brief description of the structure of Mars' atmosphere is necessary. Several terms defined here will be used throughout the rest of this thesis. Moreover, an understanding of the structure is critical for interpreting the isotope ratios in the context of atmospheric loss.

As already mentioned, the surface pressure is around 6 mbar. The atmospheric scale height,

$$H = \frac{kT}{\mu g} \quad (1.1)$$

is determined by the temperature, T , the mean molecular mass, μ , and the surface gravity, g , and k is the boltzmann constant. It is ~ 11 km on Mars compared to about 8 km on Earth. The scale height is the vertical distance over which the atmospheric pressure decreases by a factor of e . So, at roughly 150 km Mars and Earth have the same atmospheric pressure.

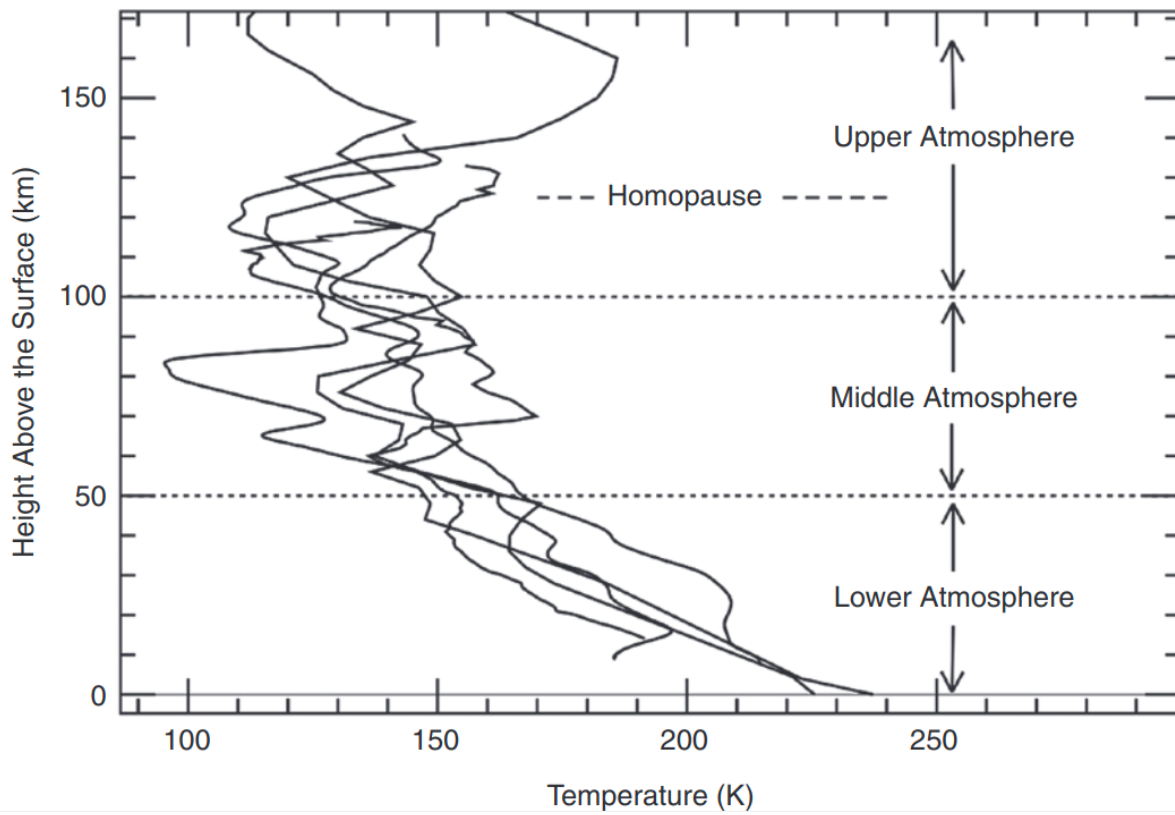


Figure 1.7: Temperature profiles obtained from accelerometer measurements during the descent of landers. Credit: (Smith et al., 2017).

The lower atmosphere of Mars extends from the surface up to ~ 50 km and is characterized by temperatures that decrease with height (see Fig. 1.7). Convection in the lowest scale height is the primary energy transport mechanism and heating is caused by dust greenhouse warming from CO_2 . Of course, the temperatures in the lowest atmosphere depend on the time of day and season. Seasonal changes are a result of not only the obliquity of the planet (an Earth-like 25.2°), but also the eccentricity, which provides Mars with 40% more insolation at its closest point to the sun. Perihelion coincides roughly with southern summer. Daytime surface temperatures are around 230 K, while nighttime temperatures can be less than 200 K (Smith et al., 2017).

Temperatures are more variable in the middle atmosphere. They may be more constant with altitude than in the lower atmosphere, but typically, decrease to a minimum value (the mesopause) between 100 and 150 K at an altitude of 100–120 km (Forget et al., 2009). The mesopause and/or the homopause (see below) marks the top boundary of the middle atmosphere. Near-IR absorption provides heating while non-thermal emission cools the region (Bougher and Dickinson, 1988). Atmospheric tides and planetary waves originating in the lower atmosphere contribute significantly to the variability of the thermal structure at these altitudes (Bougher et al., 1993; Schofield et al., 1997; McCleese et al., 2008; Kleinböhl et al., 2013). Some observations have found mesopause temperatures that dip below the CO_2 frost point such that CO_2 clouds can form (Schofield et al., 1997; Forget et al., 2009).

The temperature increases in the thermosphere (upper atmosphere) due to absorption of solar extreme ultraviolet (EUV) radiation (Bougher et al., 1999) before becoming isothermal. This heating varies with eccentricity and obliquity as well as from solar rotation (~ 27 day period) and solar cycle (~ 11 year period) variations. Molecular conduction transports heat downward that can be radiated away by CO_2 . Dynamical processes, such as large scale winds and gravity waves, can redistribute heat and constituents leading to spatial and temporal variability in the thermosphere (Bougher et al., 2017).

The **homopause**, or **turbopause** (the technical definitions of both are detailed in Chapter 2), separates the well-mixed lower part of the atmosphere (homosphere) from the upper atmosphere.

Below the homopause, turbulent motion dominates such that the composition of the atmosphere stays essentially the same as altitude increases. Above the homopause (heterosphere), there is little mixing and gases are distributed more independently. Each species has its own scale height, such that the density of heavier gases drops off more rapidly with altitude than lighter gases. On Earth, the homopause altitude is around 105 km. On Mars, as will be discussed in Chapter 2, the average is around 110 km.

The **exobase** is the altitude at which the mean free path of a given particle is equal to the scale height of the atmosphere; the average distance a particle travels before colliding with another particle is the same distance by which the density falls by a factor of e . The exobase, then, marks the boundary above which particles can escape to space. Below, a particle is likely to lose its energy through collisions, but above, in the exosphere, it will be on a ballistic trajectory. Earth's exobase is roughly 500 km, but is much lower on Mars, about 200 km. The focus of Chapter 3 will be to use the homopause, exobase, and scale heights in the thermosphere to derive the fractionation of isotopes in the upper atmosphere from which estimates of atmospheric loss can be made.

1.4 Summary and Outline

While I have surely skipped over many important experiments, observations, and reviews, I hope to have presented the reader sufficient detail on the current state of knowledge of Mars' atmospheric evolution and on necessary concepts to understand the motivation behind the work that follows. Below, I quickly summarize some crucial elements of the introduction.

- Mars is cold, dry planet today, but its geology and mineralogy prove it was once warm and wet enough to have sustained liquid water. This requires greenhouse warming from a thicker early atmosphere.
- When compared to Earth, both the mass-fraction and isotope ratios of atmospheric gases point toward the loss of an early atmosphere.
- Light isotopes are relatively more abundant at the exobase, where particles can be lost to

space, than they are the below the homopause, where the atmosphere is well-mixed. Thus, atmospheric escape preferentially removes light isotopes.

- Argon is particularly useful as a tracer of atmospheric evolution because it is one of the major atmospheric species and, as a noble gas, is affected by fewer processes that can obfuscate the isotopic record.

The thesis is organized as follows: In Chapter 2 I derive homopause and turbopause altitudes in Mars' atmosphere and discuss the physical mechanisms responsible for setting these altitudes. I derive exobase altitudes and thermospheric scale heights in Chapter 3. From these, I determine the fractionation of Ar isotopes between the homopause and exobase and use the fractionation to calculate the fraction of Ar lost from the early Mars atmosphere. Then, in Chapter 4, I develop a box model for the evolution of Ar isotopes that includes volcanic outgassing, delivery and blowoff by impacts, crustal degassing, and escape to space. This provides a more detailed analysis of the total integrated Ar loss. Before summarizing and concluding, I discuss what the Ar results suggest about total CO₂ loss and the implications for the early Mars' atmosphere.

Chapter 2

Turbopause/Homopause

2.1 Introduction

The transition between the well-mixed, turbulent lower atmosphere and the diffusive upper atmosphere is a region of coupled physical processes that impact the structure and dynamics of the mesosphere and thermosphere. The turbopause is typically defined as the altitude at which the eddy diffusion coefficient is equal to the molecular diffusion coefficient. It represents the transition from strong turbulent mixing below to diffusive separation and little turbulence above. A similar concept, the homopause (or “mixing turbopause”), is what demarcates the homosphere from the heterosphere — the mean molecular mass changes from a constant value with altitude in the lower atmosphere to altitude-dependent in the upper atmosphere. Additionally, because turbulence is generated by breaking waves in the mesosphere, the turbopause can be approximated by the transition from strong wave dissipation to free propagation (the “wave-turbopause”) (Offermann et al., 2006, 2007). While each of these is measured differently and may occur at a different altitude, each is governed by the same mechanisms. And, of course, they are not infinitesimal boundaries but gradual transition regions. When referring to the generic altitude regime where eddy and molecular diffusion are comparable, we will use either “turbo/homopause,” or “transition region.” When one of “turbopause,” “homopause,” or “wave-turbopause” appears, it is with reference to the definitions given above. In Earth’s atmosphere the transition region has been studied extensively through a variety of techniques. The turbopause has been determined from observations of sodium clouds ejected by sounding rockets (Lehmacher et al., 2011) and through turbulent energy dissipation

rates from radar measurements (Hall et al., 1998, 2016); the homopause from profiles of mixing ratios (Danilov, 1979; Offermann et al., 1981); and the wave-turbopause from studies of wave dissipation (Offermann et al., 2006, 2007). Furthermore, studies of this transition region on Earth have informed our understanding of the dominant processes in the middle atmosphere and their consequences.

Studies of Earth’s mesospheric thermal structure and stability have been particularly important. A static (or convective) instability occurs when the atmospheric lapse rate is greater than the adiabatic lapse rate and can cause waves propagating from below to dissipate through breaking/saturation (Lindzen, 1981). So too can a dynamical instability, which is generated by wind shear. Earth’s mesospheric temperature structure is such that the static stability, as measured by the square of the Brunt-Väisälä frequency, N^2 , is typically low between about 80-90 km (Gardner et al., 2002). While the background atmosphere is generally stable, small perturbations, especially at altitudes with smaller values of N^2 , can induce instabilities. Waves that saturate generate turbulence (Hodges, 1969; Lindzen, 1981; Leovy, 1982; Rapp et al., 2004), which is reflected by an increase in the eddy diffusion coefficient. At these altitudes they also cause a downward heat flux (Walterscheid, 1981; Gardner et al., 2002) and atmospheric drag that can weaken or reverse the winds (Lindzen, 1981) (and are responsible for the warm winter mesopause). Breaking/saturation limits amplitude growth, whereas amplitudes increase exponentially with altitude where waves propagate freely (Fritts, 1984; Rapp et al., 2004; Offermann et al., 2006). This is the case above about 90 km on Earth. Approaching the mesopause, the atmosphere becomes more statically stable (Gardner et al., 2002) and wave amplitudes grow more rapidly (Rapp et al., 2004). The transition from dissipation to freely propagating waves and has been dubbed the “wave-turbopause” (Offermann et al., 2006, 2007). Upward propagation continues until dissipation mechanisms in the lower thermosphere become strong enough to damp the waves. Yiğit et al. (2008) investigated the relative strengths of different dissipative mechanisms throughout Earth’s thermosphere including breaking, Newtonian cooling, ion drag, and molecular viscosity. Gravity wave amplitudes and drag peak in the lower thermosphere where dissipation is substantial. Turbopause altitudes have been

shown to have latitudinal, seasonal, and long term changes (Hall et al., 1998, 2016; Holmen et al., 2016; Offermann et al., 2007). Such changes reflect the spatial and temporal variability of all the processes described above and lead to an altitude and latitude dependent energy budget (Gardner et al., 2002; Yiğit and Medvedev, 2009), seasonal distribution of species (Vlasov and Kelley, 2010), and circulation of the mesosphere and thermosphere (Lindzen, 1981).

Studies of the turbo/homopause region at Mars have been much more limited. Based on in-situ measurements of atmospheric N_2 and Ar from the Viking landers, Nier and McElroy (1977) found Mars' homopause to be near 120 km. Recently, Jakosky et al. (2017) calculated the homopause altitude from MAVEN (Mars Atmosphere and Volatile EvolutioN) measurements of N_2 and Ar densities from the NGIMS (Neutral Gas and Ion Mass Spectrometer) instrument. Particular attention was paid to the separation between the homopause and exobase because the diffusive separation that takes place between these altitudes determines the relative abundance of species at the altitude at which escape occurs. Thus, the homopause altitude is important for inferring total atmospheric loss from the isotope record (Jakosky et al., 1994; Pepin, 1994; McElroy et al., 1977; Wallis, 1989; Leblanc et al., 2012; Hu et al., 2015; Kurokawa et al., 2015; Slipski and Jakosky, 2016; Jakosky et al., 2017). In this paper, we extend the discussion to examine if the physical processes setting Earth's turbopause adequately explain the homopause altitudes derived for Mars from a simple extrapolation from N_2 and Ar density profiles.

Specifically, we investigate whether Mars' atmospheric structure is consistent with strong wave dissipation below the turbo/homopause and free propagation above until molecular dissipation damps wave activity. Evidence for gravity waves in the lower atmosphere has come from images of lee waves (Briggs and Leovy, 1974) and temperature fluctuations (Creasey et al., 2006). Instabilities in the middle atmosphere have been interpreted as consequences of gravity waves (Heavens et al., 2010), as have density perturbations observed in the thermosphere (Yiğit et al., 2015; England et al., 2017; Terada et al., 2017). Fritts et al. (2006) showed that thermospheric perturbations (wavelengths < 200 km) can grow to extremely large amplitudes and that their spectral shape was consistent with gravity waves undergoing dissipation. Here, we use temperature profiles of the

lower atmosphere from the Mars Reconnaissance Orbiter’s MCS (Mars Climate Sounder) and of the upper atmosphere from temperatures derived from NGIMS Ar densities (Stone et al., 2015) (see also Bougher et al. (2015) and Bougher et al. (2017)). The datasets are described in Section 2.2. From the temperature profiles, we calculate monthly averaged profiles of N^2 , the square of the Brunt-Väisälä frequency, and the temperature variances. We use the variances as a proxy for wave amplitudes to investigate wave dissipation and calculate wave-turbopause altitudes (Offermann et al., 2006). We also derive homopause altitudes from N_2/Ar profiles from NGIMS, described in Section 2.2. In Section 2.3, we present the monthly averaged temperature, N^2 , and standard deviation profiles as well as the homopause and wave-turbopause altitudes. We compare the profiles to Mars Climate Database (MCD) simulations (Forget et al., 2009; Millour et al., 2018) and interpret the results in terms of wave dissipation and propagation in different altitude regions in Section 2.4. We also compare the homopause altitudes to the wave-turbopause altitudes and those predicted by the profiles by finding where the eddy diffusion coefficient equals the molecular diffusion coefficient for a given set of wave parameters. In Section 2.5, we summarize our results and conclusions.

2.2 Data and Methods

In this section, we describe the MAVEN and MRO datasets used as well as the techniques to derive homopause, turbopause and wave-turbopause altitudes. First, we briefly discuss neutral density measurements collected by NGIMS and their spatio-temporal extent and how N_2 and Ar number densities are used to find homopause altitudes. Ar densities are also used to derive temperatures, which we use to find monthly-averaged temperature profiles of the upper atmosphere. Then, we describe the MCS temperature measurements and how we bin them to compare with the upper atmospheric profiles. From the temperature and density profiles we calculate Brunt-Väisälä frequencies, which are useful to interpret the altitude regions where waves are likely to break/saturate, as well as eddy and molecular diffusion coefficients and linear saturation and molecular dissipation terms, which enable us to derive turbopause altitudes. We end this section with a discussion of how monthly-averaged temperature standard deviations can be used as a proxy for wave amplitudes and

how the wave-turbopause can be derived from them.

In our analysis we use upper atmospheric neutral densities of Ar, N₂, and CO₂ from the NGIMS instrument on MAVEN (Mahaffy et al., 2015b,a) from Feb 2015 - Oct 2016 (orbit numbers 713 - 4377, MY 32 $L_s = 290^\circ$ - MY 33 $L_s = 300^\circ$). These densities are measured every orbit between about 500 km and periapse (~ 150 km), during both the inbound and outbound segments of the orbit. Periapse was lowered to about 120 km during several “deep dip” campaigns that were performed during this time. The horizontal distance covered along a single periapse pass is around 1500 km. A typical inbound pass spans $\sim 20^\circ$ latitude and a few hours of local time (Fig. 2.1). O atoms interact with the walls of the instrument ante-chamber, building up a layer that reacts with various species to form, for example, additional CO, CO₂, O₂ and NO over the course of each pass. Background levels of reactive species, like CO₂, increase from this process much more significantly on the outbound leg (higher gas load) than the inbound (Mahaffy et al., 2015a) (supplementary info). Thus, we restrict our analysis to only the inbound portions of each periapse pass and avoid outbound phases.

Periapse has swept through a wide range of latitudes and local times as the orbit has precessed (Fig. 2.1) (Jakosky et al., 2015b). Here, we use the available Level 2 (version 07, revision 01) NGIMS data. As can be seen in Fig. 2.1, there are some gaps in the 2015 data due to solar conjunction from May 27 - July 2 ($L_s = 348 - 6$) and from spacecraft safe mode events April 4 - 14 ($L_s = 320 - 325$), and Aug 12 - 21 ($L_s = 26 - 30$). Over the full time range, latitudes within -74° to 74° and all local times were sampled. However, there is limited overlap at a given point in latitude-local time space and repeat observations occur at significantly different seasons.

We derive homopause altitudes calculated following the same method used by Mahaffy et al. (2015a) and Jakosky et al. (2017). Because MAVEN’s periapse does not reach as low as the homopause, we must extrapolate NGIMS densities downward. We do so as a function of altitude and as function of CO₂ number density to the point where the ratio of two species equals the lower atmospheric ratio (Fig. 2.2). Here, we use the ratio of N₂/⁴⁰Ar because CO₂ densities can vary in the lower atmosphere with location and season due to deposition and sublimation, precluding

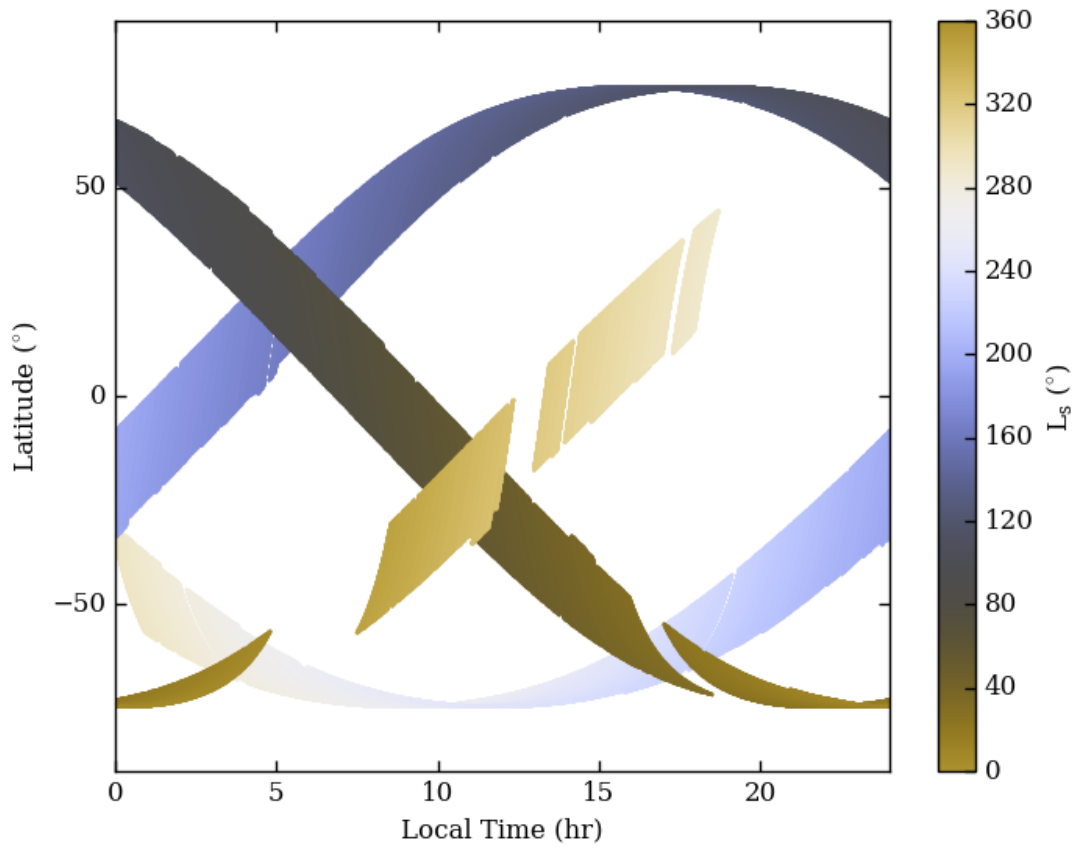


Figure 2.1: Local time and geographic latitude coverage of NGIMS inbound passes below 300 km from Feb 2015 to Dec 2016. Each orbit is represented by a thin line of constant color, where the color represents the L_s of that orbit.

knowledge of expected atmospheric mixing ratios at the turbopause. N_2 and ^{40}Ar are both non-condensable species, so their lower atmospheric ratio remains constant and has been measured at the surface in the past by Viking ($\text{N}_2/^{40}\text{Ar}=1.7$) and more recently by the SAM (Sample Analysis at Mars) instrument on the Curiosity rover. The most recent analysis (Franz et al., 2017) pins the ratio much closer to that measured by Viking (Owen et al., 1977) than previous SAM results (Mahaffy et al., 2013; Franz et al., 2015). We use $\text{N}_2/^{40}\text{Ar}=1.25$ (Franz, personal communication) as the lower atmospheric ratio everywhere and assume it stays constant up to the homopause.

We present homopause altitudes derived from two days of orbits instead of from each individual orbit for a few reasons. First, the homo/turbopause has traditionally been thought of as an average value, not an instantaneous one because local changes in the turbulent energy at any moment would cause the homo/turbopause to fluctuate. We are interested more in long term and global variations and our observations are not frequent enough to discern the conditions driving those short-timescale fluctuations. Though in principle these could be studied. Also, density profiles show variability on orbit-to-orbit timescales (several hours) from specific local conditions (Fig. 2.2). And profiles from individual orbits display significant structure from dynamical phenomena and/or horizontal variations (Fig. 2.2). So, we combine density measurements into two-day bins; each bin contains 7 - 11 orbits. Though local time and latitude of periapse do not change significantly during this interval, the longitude does, meaning that we have smoothed over sun-asynchronous tidal features. For every two-day interval, we fit a line to the log of $\text{N}_2/^{40}\text{Ar}$ below 190 km, as displayed in Fig. 2.2. The altitude at which that extrapolated line intersects 1.25 is assumed to be the homopause altitude.

We also use temperature profiles derived from a hydrostatic integration of NGIMS Ar densities of each orbit as presented in Stone et al. (2015), which follows the method of Snowden et al. (2013) (see also Bougher et al. (2015) and Bougher et al. (2017)). The integration provides an altitude profile of partial pressure for a given species, which can then be converted to temperature using the ideal gas law. An integration constant, the partial pressure at the highest altitude, is determined from the densities between 10^4 and $8 \times 10^5 \text{ cm}^{-3}$ assuming an isothermal atmosphere

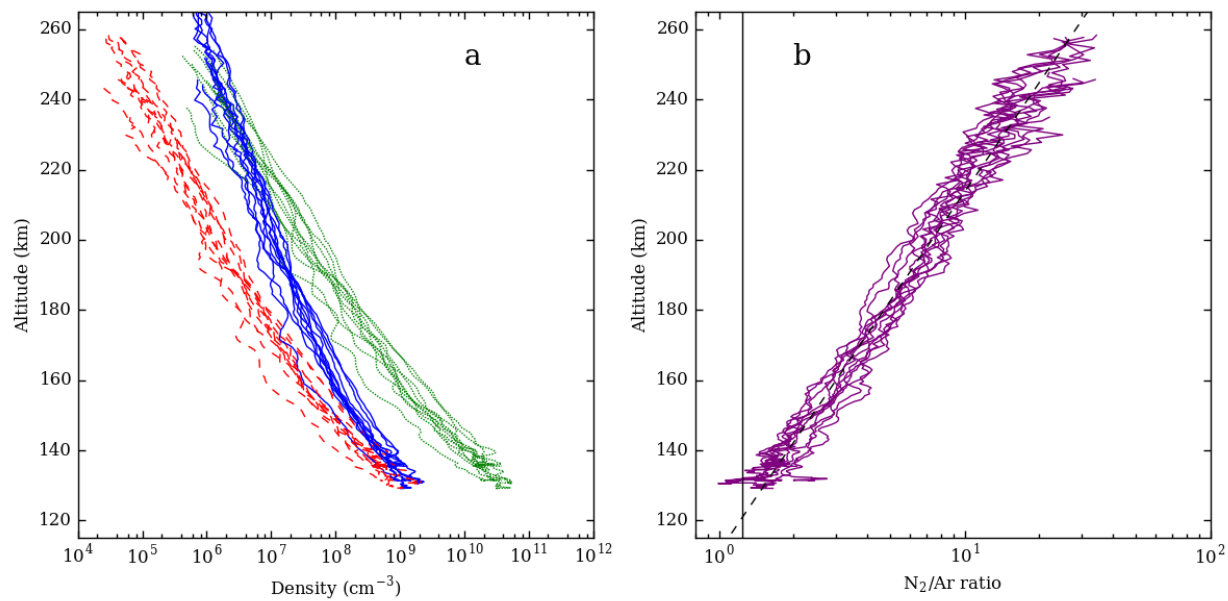


Figure 2.2: (a) Densities of CO₂ (green dotted), Ar (red dashed), and N₂ (blue solid) and (b) the N₂/Ar ratios measured by NGIMS for orbits 714-724. The solid black line and dashed line in (b) are the lower atmospheric N₂/Ar ratio and the fit used to calculate the homopause altitude, respectively.

at these altitudes. The temperatures used in this work are the same as those in Stone et al. (2015) except they have not been corrected for density variations arising from the horizontal motions near periapse, though we have removed the points from the lowest 2 km. Though MAVEN moves horizontally throughout its orbit at all altitudes, the horizontal variations between altitudes are largest near periapse. In the last 2 km, the spacecraft covers roughly 200 km of horizontal distance, which can be 20% of the horizontal change below 200 km but $< 5\%$ of the vertical change. Correcting the NGIMS density measurements at all altitudes for the horizontal motion of the spacecraft is outside the scope of this work, one can read Stone et al. (2015) for such a method and for further discussion on the topic. Because our intention is to look at the variations between profiles, we have also ignored the temperatures at the highest altitudes where each profile is assumed to be isothermal. For all the profiles in an individual month, we binned the data into 0.5 km vertical bins and found the average temperature in each bin to construct an average profile. We ignored any altitude bins with fewer than 20 points in each bin. By averaging over many profiles covering a wide region we further alleviate temperature differences due to horizontal variations as the spatial region is roughly as large as the horizontal variations in a single orbit. A single example temperature profile is shown in Fig. 2.3a (red curve) for June 2016. The shaded region represents the 1-sigma standard deviation of temperature in each altitude bin. The latitude range of periapse passes in the example shown is 18° to 40° and the local time range is 3 - 6 AM (Table 2.1). We repeated this for each month, again averaging over all longitudes during that period.

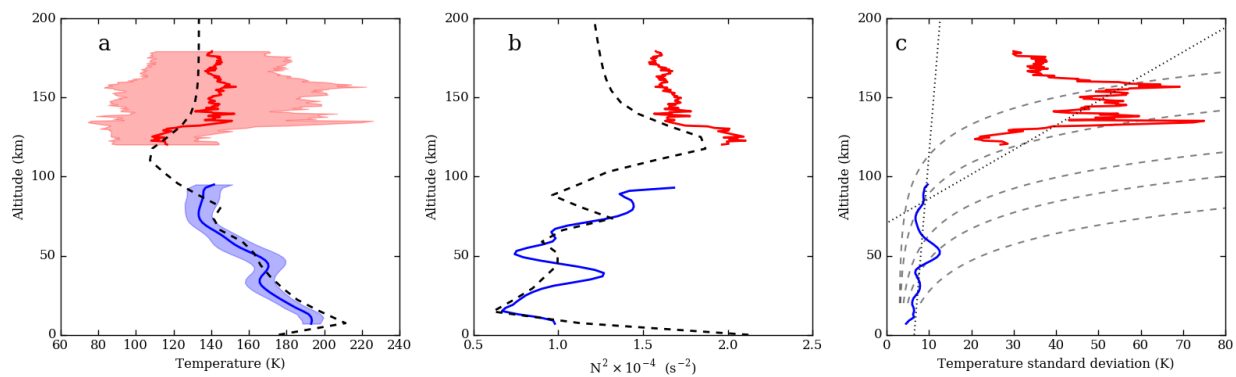


Figure 2.3: Monthly averaged (a) temperature (b) N^2 (Brunt-Väisälä frequency), and (c) temperature standard deviations for June 2016. MCS data is shown and blue and NGIMS in red. The black dashed lines in (a) and (b) are taken from an MCD simulation with the same average latitude, local time, and season. Black dashed lines in (c) represent exponential increases and the dotted lines are linear fits as described in Section 2.2.

Table 2.1: Monthly latitudes, local times, and wave-turbopause altitudes. The NGIMS ranges given are the ranges of the periaipse locations of the course of that month’s orbits. MCS ranges are the bins where data is available and there is substantial overlap in latitude and local time with the NGIMS data.

Month	NGI Latitude ($^{\circ}$)	MCS Lat ($^{\circ}$)	NGI LT (hr)	MCS LT (hr)	L_s ($^{\circ}$)	W-T Alt (km)
Feb 2015	(32, 45)	(30, 50)	17 – 19	16 – 20	289 – 300	134
Mar 2015	(10, 32)	(10, 30)	14 – 17	12 – 16	300 – 318	107
Apr 2015	(–12, 10)	(–10, 10)	11 – 14	12 – 16	318 – 335	117
May 2015	(–30, –12)	(–30, –10)	9 – 11	12 – 16	335 – 348	
Jul 2015	(–73, –56)	(–70, –50)	0 – 5	0 – 4	7 – 21	107
Aug 2015	(–73, –67)	(–70, –50)	17 – 24	20 – 24	21 – 35	115
Sep 2015	(–66, –48)	(–70, –50)	13 – 16	16 – 24	35 – 49	99
Oct 2015	(–47, –26)	(–50, –30)	10 – 13	8 – 12	49 – 62	122
Nov 2015	(–26, –5)	(–30, –10)	7 – 10	4 – 8	62 – 75	124
Dec 2015	(–5, 17)	(–10, 10)	5 – 7	4 – 8	75 – 89	
Jan 2016	(17, 40)	(10, 30)	2 – 5	4 – 8	89 – 102	82
Feb 2016	(40, 60)	(30, 50)	22 – 2	0 – 4	102 – 116	
Mar 2016	(61, 74)	(50, 70)	16 – 23	0 – 4	116 – 130	
Apr 2016	(63, 74)	(50, 70)	10 – 16	16 – 20	130 – 145	
May 2016	(41, 62)	(50, 70)	6 – 9	8 – 12	145 – 161	
Jun 2016	(18, 40)	(10, 30)	3 – 6	0 – 4	161 – 178	90
Jul 2016	(–5, 18)	(–10, 10)	0 – 3	4 – 8	178 – 196	116
Aug 2016	(–27, –5)	(–30, –10)	21 – 24	0 – 4	196 – 214	97
Sept 2016	(–47, –28)	(–50, –30)	18 – 21	16 – 20	214 – 233	
Oct 2016	(–67, –48)	(–70, –50)	14 – 18	12 – 16	233 – 252	

In order to examine temperature profiles through the full atmosphere, we used MCS measurements collected over the same time period. MCS is an infrared thermal emission radiometer that uses 9 channels to measure radiance profiles of the Martian atmosphere (McCleese et al., 2007). From these profiles vertical temperature profiles are retrieved (Kleinböhl et al., 2009, 2011), typically ranging from the surface to ~ 80 km with ~ 5 km resolution. The instrument’s standard “forward in-track” viewing observes at two local times — 3 AM and 3 PM. However, “cross-track” (90° to the left or right of the orbit track) and “forward off-track” (between 0° and 90° of the orbit track) viewing has allowed for observations at a much wider range of local times (Kleinböhl et al., 2013). Here, we use temperature profiles from Feb 2015 – Oct 2016 (Version 4) (McCleese and Schofield, 2006). These data are used in conjunction with monthly averaged temperatures derived from NGIMS, so we separated each month of MCS profiles into 20° latitude \times 4 hr local time bins. For each month, we only used that bin with the most latitude and local time overlap with the NGIMS data of the same month (Table 2.1). We binned all the profiles into 2 km vertical bins (up to 80 km where the uncertainty in an individual MCS temperature profile becomes large) and calculated the monthly mean temperature and standard deviation in each altitude bin. Fig. 2.3a and c (blue curves) show examples for a single month.

We note that measurement geometries of the NGIMS and MCS instruments are substantially different. NGIMS samples in-situ and the horizontal path covered through the orbit path have not been removed from the data. MCS integrates over each ray path to produce vertical profiles of the tangent point. Though I assume the NGIMS profiles to be representative of the periapse point and MCS of the tangent point, they are not truly vertical profiles of those points. Also, the measurements used here were not coordinated campaigns between the two instruments; no pair of individual profiles is an instantaneous snapshot of the full atmosphere. To that end, we do not attempt to compare individual profiles. Furthermore, as stated above, we average months’ worth of profiles within a large, $20^\circ \times 4$ hr spatial area so the comparisons we make are between regionally distinct locations. While the horizontal averaging of each instrument surely adds some uncertainty to the profiles presented here, this is outside the scope of this work.

To compare the lower and upper atmospheric profiles, we used simulations from the Mars Climate Database (MCD) (Forget et al., 1999; Millour et al., 2015; González-Galindo et al., 2009). For each month we pulled a single simulation from the MCD Web Interface with the mean latitude, local time, and L_s of the MAVEN periapse values during that month (Table 2.1). Our goal was not to do a thorough analysis of the agreement between the MCD simulations and the temperatures from MCS and NGIMS, but to guide us at altitudes where there are no simultaneous measurements. The simulated profiles provide an intuition about the altitude and temperature of the mesopause and a check on whether the highest altitude MCS temperatures are compatible with the lowest altitude NGIMS temperatures. In addition, we use the MCD profiles to calculate various parameters in the middle atmosphere where we do not have measurements from NGIMS or MCS.

Wave dissipation occurs in regions of instabilities. From a temperature profile, the static stability of the atmosphere can be examined through the square of the Brunt-Väisälä frequency, N^2 , at a given altitude, z :

$$N^2(z) = \frac{g}{T(z)} \left(\frac{\partial T(z)}{\partial z} + \frac{g}{C_p} \right) \quad (2.1)$$

where g is the gravitational acceleration, T is the temperature, and C_p is the specific heat at constant pressure. We calculate the specific heat following Magalhães et al. (1999): $C_p = 0.0033T^2 - 0.2716T + 656.3$. The atmosphere is stable for values of $N^2 > 0$ (the adiabatic lapse rate is greater than the atmospheric lapse rate) and unstable for $N^2 < 0$. We also use N^2 to calculate parameters related to wave dissipation (see below). Though it is primarily indicative of where convective instabilities can occur, N^2 is also useful in assessing where dynamical instabilities are likely to occur (Gardner et al., 2002). The criterion often used to determine if the atmosphere is dynamically unstable is $0 < Ri < 0.25$, where Ri is the Richardson number (Lindzen, 1981).

$$Ri = \frac{N^2}{\left(\frac{\partial u}{\partial z}\right)^2 + \left(\frac{\partial v}{\partial z}\right)^2} \quad (2.2)$$

where u is the zonal wind speed and v is the meridional wind speed. While we do not have corresponding measurements of the wind profiles, Ri will be small for very low N^2 . So, evaluating the static stability is a useful tool for studying dissipation at different altitudes.

We have computed N^2 for each monthly averaged temperature at low and high altitudes (see Fig. 2.3b). These values represent the background atmosphere, averaging perturbations from waves and tides. Though the background atmosphere may be stable, smaller values represent regions that can more readily become unstable from small perturbations. At Earth, gravity wave induced instabilities occur even when $N^2 \sim 4 \times 10^{-4} \text{ s}^{-2}$ (Gardner et al., 2002). Unfortunately, our data set does not have the spatial resolution or temporal resolution to determine whether or not static instabilities occurred for each individual profile. Heavens et al. (2010) showed that the resolution of MCS profiles is sufficient to find some instances of instabilities. However, our goal is not to find specific instances of instabilities; rather, it is to use the mean static stability profiles to assess the relative likelihood of wave propagation or wave breaking. This aids in interpreting profiles of the temperature standard deviations (discussed below). We recognize that gravity wave induced instabilities can occur at any of these altitudes (all our N^2 values are less than $2.5 \times 10^{-4} \text{ s}^{-2}$), especially where the wind shear is strong.

While a detailed analysis of individual waves in the thermosphere (see e.g. Fritts et al. (2006), Yiğit et al. (2015), England et al. (2017), and Terada et al. (2017)), is outside the scope of this work, we did calculate four parameters related to wave dissipation throughout the atmosphere for each month: the molecular diffusion coefficient, D_{mol} , the eddy diffusion coefficient, K , the dissipation due to Hodges-Lindzen breaking/saturation, β_{lin} , and the dissipation due to molecular viscosity, β_{mol} . These parameters allowed us to find the classical turbopause by finding the altitude at which $K = D_{mol}$ and $\beta_{lin} = \beta_{mol}$.

The altitude dependence of D_{mol} is calculated from NGIMS CO_2 number density, n (in m^{-3}), following Leovy (1982):

$$D_{mol} = 1.2 \times 10^{20} n^{-1} (\text{m}^2/\text{s}) \quad (2.3)$$

We extrapolated the NGIMS densities downward to derive a full profile, though D_{mol} is very small below 120 km. The eddy diffusion coefficient that will balance the exponential growth of a wave is

given by

$$K = \gamma \frac{k(c-u)^4}{2HN^3} \quad (2.4)$$

where k is the horizontal wavenumber, c the phase speed, u is the zonal wind, H the scale height, and γ is an efficiency parameter, which we set to 0.1 (Imamura et al., 2016). H and N^3 are calculated from the MCD temperature profiles because they span the full range of altitudes. We let k be $\frac{2\pi}{200}\text{km}^{-1}$ and c equal to 50 m/s, consistent with gravity waves expected in the middle atmosphere (Yiğit et al., 2008; Imamura et al., 2016; Terada et al., 2017). We assumed a small background wind such that $u = 0$, though this is obviously a simplification and is discussed further in Section 2.4. It is clear from Eq. 2.4 that the choice of c will significantly influence the turbopause altitude. Order of magnitude differences in the assumed values of k and c would be reasonable given the lack of observations of waves between 50-120 km. We discuss the uncertainty associated with our assumptions in Section 2.3.

The dissipation due to saturation, assuming a convective instability and constant background winds (Yiğit et al., 2008), is

$$\beta_{lin} = \frac{1}{H} + \frac{3}{c-u} \frac{\partial u}{\partial z} + \frac{1}{N} \frac{\partial N}{\partial z} \quad (2.5)$$

and the dissipation due to molecular viscosity is:

$$\beta_{mol} = \frac{\nu_{mol}N^3}{k(c-u)^4} \quad (2.6)$$

where ν_{mol} is the molecular viscosity given by $\nu_{mol} = 3.563 \times 10^{-7}T^{0.69}\rho^{-1}$ and we have assumed a large Prandtl number (a value near 1 adds a factor of 2 to the equation and does not change our results) (Yiğit et al., 2008). Again, we utilized the temperature profiles from the MCD simulations and the CO₂ densities from NGIMS.

Furthermore, we used the monthly standard deviations in temperature as representative of the real square-root of geophysical variations over a background temperature profile due to wave activity — whether from planetary or gravity waves — during that time. This assumption ignores that some variation is certainly due to changes in the solar EUV intensity, small changes in local

time and latitude, and large longitudinal changes. Unless these generate large altitude-dependent temperature variations, our interpretations will not be significantly affected. For instance, we determined the contribution from longitudinal variations in the MCS data enabled by the large number of profiles available. For each month, we binned the data into 16 longitude bins and calculated the standard deviation as a function of altitude for each bin. We found that those mean standard deviations were typically about 2 K less at all altitudes than the standard deviations across all longitudes.

The amplitude (ϕ) of a (non-dissipative) vertically propagating wave will increase exponentially,

$$\phi = \phi_0 e^{(z-z_0)/(2H)} \quad (2.7)$$

where z and z_0 are the height and a reference height, and H is the scale height. Examples of the expected amplitude of temperature of freely propagating waves are shown by the dotted lines in Fig. 2.3c.

Offermann et al. (2006) defined the wave-turbopause as the altitude at which the two lines fit to the regions of small temperature fluctuations at low altitudes and high fluctuations at higher altitudes intersect (see also Offermann et al. (2007); John and Kishore Kumar (2012); Hall et al. (2008, 2016)). The standard deviations are a proxy for wave amplitudes, so where they increase less than exponentially, dissipation is significant. Dissipation in the lower-middle atmosphere from saturation/breaking causes turbulence. So, the wave-turbopause is an estimate of the turbopause because the transition from strong to weak wave dissipation causes the transition from strong to weak turbulence. Though, again, the turbopause is a transition region; a single point is an approximation —John and Kishore Kumar (2012) have extended the concept of the wave-turbopause to a wave-turbopause layer.

Because we lack temperatures between 80 – 120 km in months with deep dips and often between 80 – 160 km, we do not have continuous profiles of the temperature standard deviations.

This makes it difficult to interpret for some cases whether we can reliably determine the wave-turbopause. Based on the temperature, N^2 , and standard deviation profiles (that sample different altitudes and vary with latitude and local time), we split the data into four groups.

The first group consists of the months where there is no clear increase in standard deviations at the lowest NGIMS altitudes (2015: May, Oct; 2016: Mar, Apr, Oct), an increase spanning $\lesssim 10$ km (Feb 2016, May 2016), or a decrease in the standard deviations with altitude below 80 km (Sep 2016) such that reliable fits to the standard deviations can not be obtained.

The second group are those months where the wave-turbopause can be calculated most reliably. That is, at the lowest NGIMS altitudes there is an unambiguous, steep increase in temperature, N^2 is large (up to $1.5 - 2.0 \times 10^{-4} \text{ s}^{-2}$) near the maximum predicted by the MCD, and the temperature standard deviations increase dramatically (from ~ 20 K to > 50 K below the isothermal region). These conditions suggest that lowest altitudes reached by NGIMS are approaching the mesopause and that the waves are freely propagating through this region, meaning that we are observing the transition region. The months in this group are July 2015 and Jan, Jun, Jul, and Aug 2016. We fit the lower atmospheric variations from 25 km to 80 km. For the upper atmospheric standard deviations, we restricted the altitude range to where the atmosphere is statically stable and molecular viscosity is not too high. That is, because the standard deviations do not increase with altitude over the full range (discussed further in Section 2.4), we know that not all altitudes are reflective of the freely propagating waves assumed in the wave-turbopause calculations. Therefore, we only used those points for which $N^2 > 1.3 \times 10^{-4} \text{ s}^{-2}$ and $D_{mol} < 5 \times 10^6 \text{ m}^2/\text{s}$. An example is shown in Fig. 2.3c. The dotted lines represent the fits to the MCS and NGIMS temperature standard deviations and the intersection gives the altitude of the wave-turbopause.

For several months at the lowest NGIMS altitudes, we see temperature standard deviations that increase (often not nearly as significantly as those months in the first group) and have N^2 values that are larger than in the isothermal. These months (group three) are Feb, Apr, Aug, Sep, and Dec 2015. In the last group (Mar and Nov 2015), there is an increase in thermospheric temperature standard deviations, but N^2 remains low ($\lesssim 1.0 \times 10^{-4} \text{ s}^{-2}$) even at the lowest NGIMS

altitudes. We found wave-turbopause altitudes for the months in these two groups as well, but we distinguish between these two groups and the second group because it is not as clear that temperature fluctuations are due to freely propagating waves. Additionally, we must choose individual altitude limits for each month by truncating where the atmosphere becomes isothermal and where there is a clear increase in the standard deviations with altitude.

2.3 Results

Here, we first describe the general temperature structure and static stability of the upper and lower atmosphere. We also remark on altitude regions with different temperature standard deviations. Then we present homopause, turbopause and wave-turbopause altitudes, briefly comparing some of the similarities and differences between them.

Each monthly averaged temperature profile of the lower and upper atmosphere is shown in Fig. 2.4. In some months, often when a deep-dip was performed, there is a strong positive temperature gradient with height between 120–160 km (e.g., Feb 2015, Apr 2015, Jul 2015, Sep 2015, Jul 2016). At the highest altitudes, the temperatures are isothermal. We find that months with measurements on the dayside transition to isothermal temperatures at higher altitudes (150–170 km) than on the nightside (140–150 km). These differences are in agreement with predictions by Valeille et al. (2009). A low transition to isothermal (140 km) is seen, for example, in Fig. 2.3 for June 2016 where the local time was around 4AM. These are also the coldest exospheric temperatures observed. Variations in the thermospheric temperatures are discussed in more detail in Stone et al. (2015).

The temperature gradient in the lower atmosphere decreases with increasing altitude up to around 60 km. This marks the transition to the middle atmosphere (Smith et al., 2017) For those months where MAVEN’s periapse is low enough to see a large change in temperature from the upper isothermal temperature, we find the temperatures at the lowest MAVEN altitudes and those from MCS are close to the simulated MCD profiles. This is visible in Fig. 2.3 for June 2016 and is generally the case in the lower atmosphere and lowest MAVEN altitudes for other months. However,

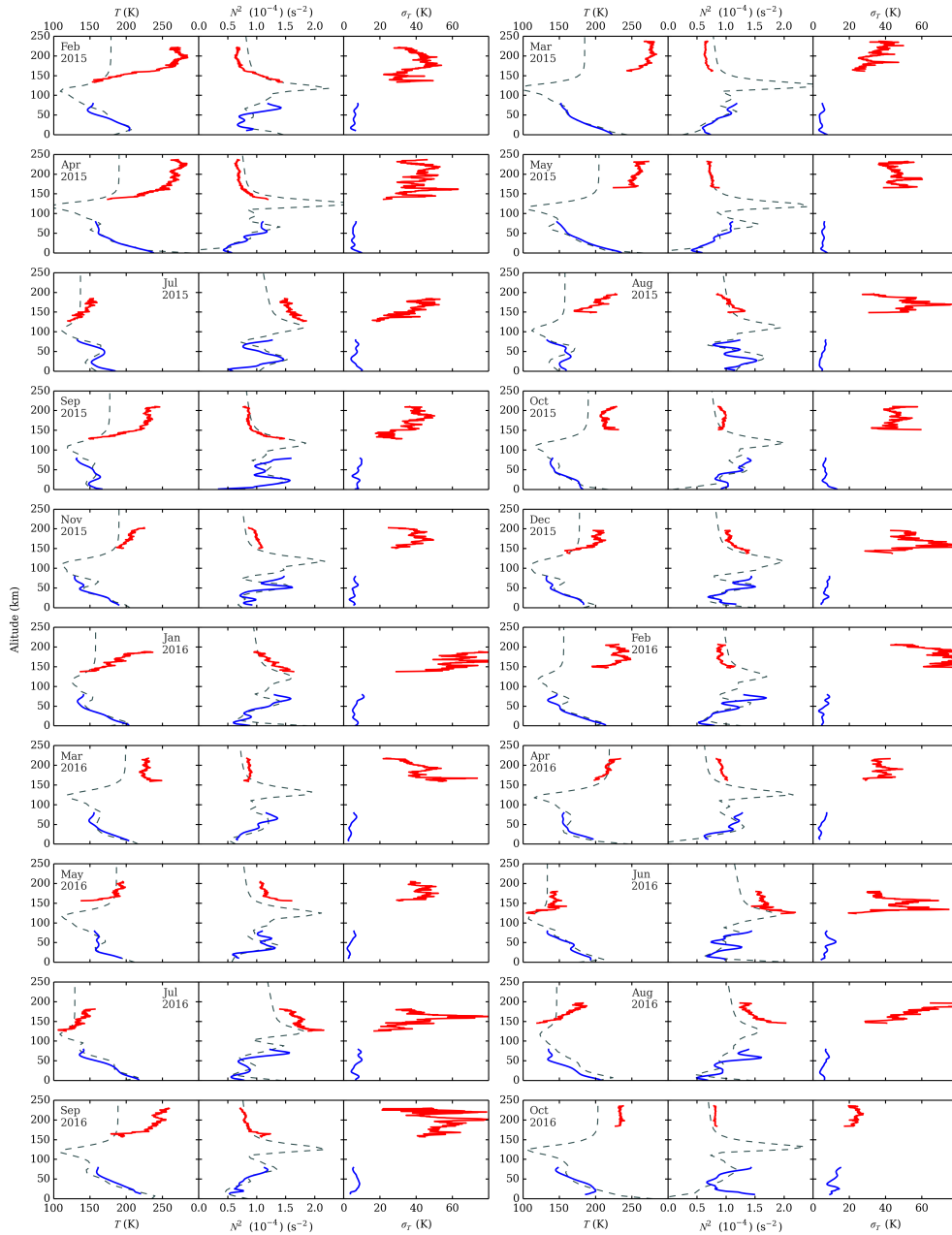


Figure 2.4: Monthly averaged temperature (columns 1 and 4), N^2 (columns 2 and 5), and temperature standard deviations (columns 3 and 6) for each month. MCS data are shown and blue and NGIMS in red. The dashed lines are taken from an MCD simulation with the same average latitude, local time, and season.

for many months the model isothermal temperatures are much cooler than observed, sometimes up to 100 K.

The square of the Brunt-Väisälä frequency, N^2 , for June 2016 is shown in Fig. 2.3b and for all months in Fig. 2.4. There are several things to note: 1) The isothermal region (> 160 km) is characterized by low static stability, 2) the atmosphere is more stable in the lower thermosphere (120 - 160 km) where the temperature is increasing significantly with altitude, and 3) the middle atmosphere is less stable than from 120 -160 km, generally becoming more stable closer to the mesopause. In the MCD profiles (Fig. 2.4) the maximum N^2 values (about $2 \times 10^{-4} \text{ s}^{-2}$) are seen just above 100 km.

Similar to Earth (Offermann et al., 2006), we find a region of low temperature variability at low altitudes (here, 20-80 km) and high variability at high altitudes (>120 km). This can be seen in Figs. 2.3c and 2.4. The MCS standard deviation profile in Fig. 2.3c has magnitudes typical of all those shown in Figs. 2.4 and 2.8, about 5-10 K. This is consistent with the amplitudes of Kelvin waves (1 – 3 K) and planetary waves (5-10 K) between 40 – 80 km observed previously by MCS (Guzewich et al., 2012). Modeling of convectively-generated gravity waves by Imamura et al. (2016) predict amplitudes of up to about 5 K below 30 km and up to 50 K from 50 – 100 km. These have dominant horizontal wavelengths of about 10 km, so MCS is not sensitive to them. Together, these ranges suggest that the perturbations observed below 80 km are the superposition of gravity waves, Kelvin waves, and planetary waves.

The upper atmospheric standard deviations are > 20 K. More specifically, they increase between $\sim 120 - 160$ km from about 20 K to 40 – 60 K and reach constant values between 30 – 60 K above 160 km. The density perturbations from which the thermospheric temperatures are derived (Yigit et al., 2008; England et al., 2017) and from accelerometer data (Fritts et al., 2006) have been interpreted as gravity waves, though tides also drive density perturbations (Liu et al., 2017; Gröller et al., 2018). To test the effect of longitudinal structures we binned all the NGIMS temperature profiles in the data set into 12 longitude bins. There wave 1-3 structures in the temperatures, N^2 values, and temperature standard deviations up to around 160 km. The standard deviation in any

given longitude bin may vary up to ± 10 K from the total standard deviation at the lowest altitudes and ± 5 K above 160 km. However, the standard deviation profile of each bin has the same generic shape — it grows from around 20 K to 60 K from 120 – 160 km before decreasing to about 40 K at 220 km.

Between both 40 – 80 km and 120 – 150 km there is a roughly linear increase in the standard deviation, with a steeper increase between 120 – 150 km. The lower altitude amplitudes are not fit well by an exponential (Fig. 2.3c), but they do vary substantially at a given altitude. In Fig. 2.5, we show the month-to-month variability in the standard deviations at 70 km. The increase in the standard deviation of temperature with altitude is much more rapid at higher altitudes, especially where there is a large positive increase in temperature and N^2 , suggesting waves are likely propagating more freely.

Homopause altitudes derived from N_2/Ar densities are between 60 – 140 km (Fig. 2.5, orange circles); extrapolating as a function of CO_2 density, the homopause levels are between $n_{CO_2} \sim 10^{10} \text{ cm}^{-3}$ (~ 135 km) and 10^{13} cm^{-3} (< 80 km) and vary through the mission in the same manner (Fig. 2.6). The large dips in the homopause altitudes could be a result of the extrapolation procedure ignoring the large temperature gradient in the thermosphere. We can try to understand this effect by choosing a different temperature for the downward extrapolation. Though of course, the temperature change to mesospheric temperatures does not happen instantaneously. For instance, in Dec 2015, if instead of extrapolating the fit below periapse, we assume a background temperature much colder than that inherent in the fit (150 K instead of 250 K), the homopause altitude can increase by up to 30 km. Similarly in July 2015 and Jun 2016 the homopause altitudes below 90 km may increase by 10 km if 120 K is used instead of 170 K. The N_2/Ar values near periapse in Deep Dip 1 (Feb 2015) approach 1.25, so they are negligibly altered by an alternative extrapolation. However, determining exactly how the thermospheric temperature causes an underestimation in the homopause altitudes is difficult. First, a wide range of temperatures below periapse may be feasible to use. Using the MCD as a guide is instructive, but that introduces large uncertainty as well because nearly 100 K differences exist between MCD and the derived NGIMS temperatures.

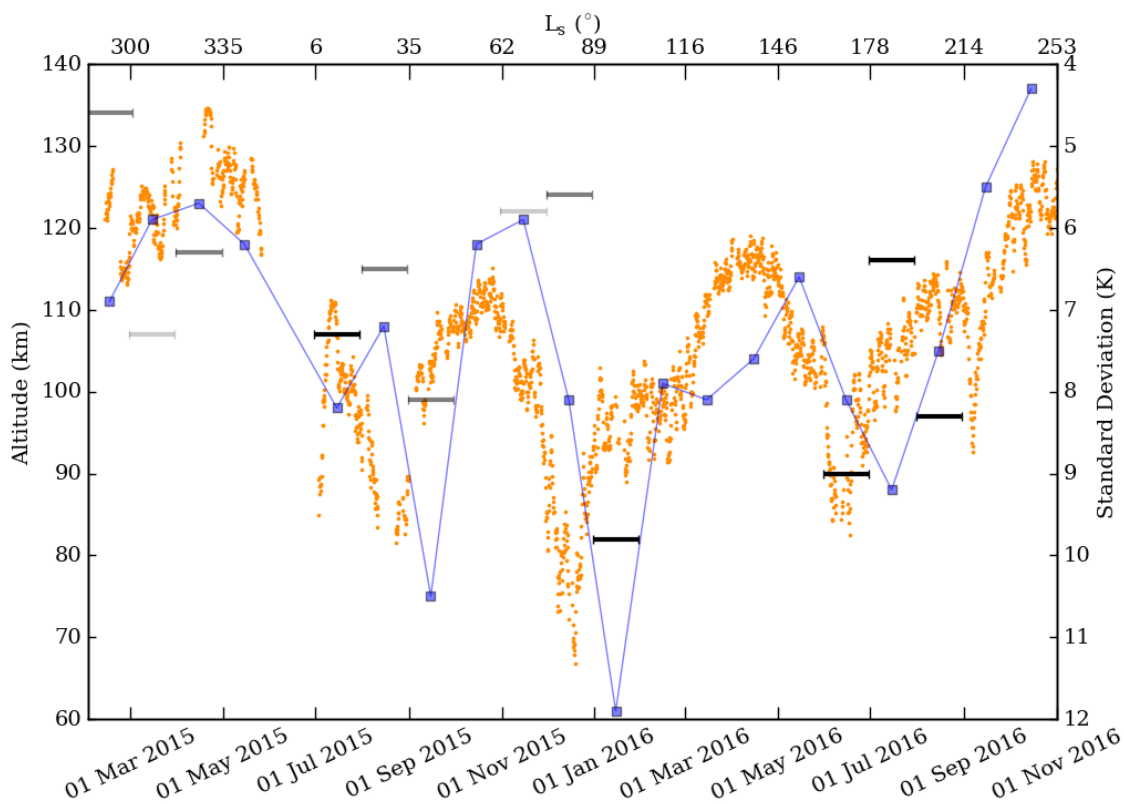


Figure 2.5: 2-day averages of homopause altitudes from Feb 2015 - Oct 2016 (corresponding L_s values are shown at the top) are shown with orange dots. Horizontal bars show the wave-turbopause altitudes calculated for various months. Black bars are those months for which a wave-turbopause could be reliably calculated (group 2 as described in Section 2.2). Dark gray are for those in group 3 and light gray for group 4. The blue squares show the standard deviations at 70 km for each month (right axis, inverted).

Additionally, the temperature and altitude of the mesopause will ultimately determine the lower limit of the temperature choice that is reasonable in the lower thermosphere. But again, we would be forced to completely rely on the MCD profiles as we lack data at those altitudes. Extrapolating down with a different temperature ignores the data we do have from NGIMS and only considers the N_2/Ar value at periapse. Furthermore, it is not clear that the lower altitudes sampled by the changing periapse lead to higher homopause altitudes. One would expect that cooler temperatures sampled by a lower periapse should lead to steeper slopes of N_2/Ar and higher homopause altitudes. For example, in June 2016 the homopause drops below 100 km when periapse is around 150 km. Then, periapse lowers to below 130 km but the homopause remains around 87 km; the fits to the N_2/Ar profiles are nearly identical even though colder temperatures are sampled. In fact, as discussed in the next section, dramatic decreases in the CO_2 densities at 180 km accompany these low homopause altitudes which may imply that the atmosphere is contracting significantly and the aberrant homopause altitudes are real. It may still be the case that below 120 km the temperature drops to ~ 120 K and the homopause altitudes are still underestimated by about 10 km, but it is not obviously so. Thus, we acknowledge that the homopause altitudes below 90 km are likely lower than the true value and present them here with caution.

The same changes through time are seen in the homopause altitudes and the standard deviation curve in Fig. 2.5. The lowest homopause altitudes occur when the standard deviations at 70 km are highest. The altitudes at which $K = D_{mol}$ and $\beta_{lin} = \beta_{mol}$ for the given set of gravity wave parameters described in Section 2.2 are shown in Fig. 2.7 and are higher than the homopause altitudes, though they show roughly the same trend with time as the homopause altitudes. The highest homopause altitudes occur near $L_s \sim 300^\circ$ around 6 PM and the lowest altitudes are found near 90° and $160^\circ L_s$ around 6 AM.

The high turbopause altitudes are a consequence of our choice of wave parameters. For each month, the systematic uncertainty in the homopause due to those parameters can be estimated by assuming different values. The turbopause altitudes for both $K = D_{mol}$ and $\beta_{lin} = \beta_{mol}$ depend on the term $H \ln[k(c - u)^4]$. Decreasing $c - u$ from 50 m/s to 5 m/s will decrease the turbopause by

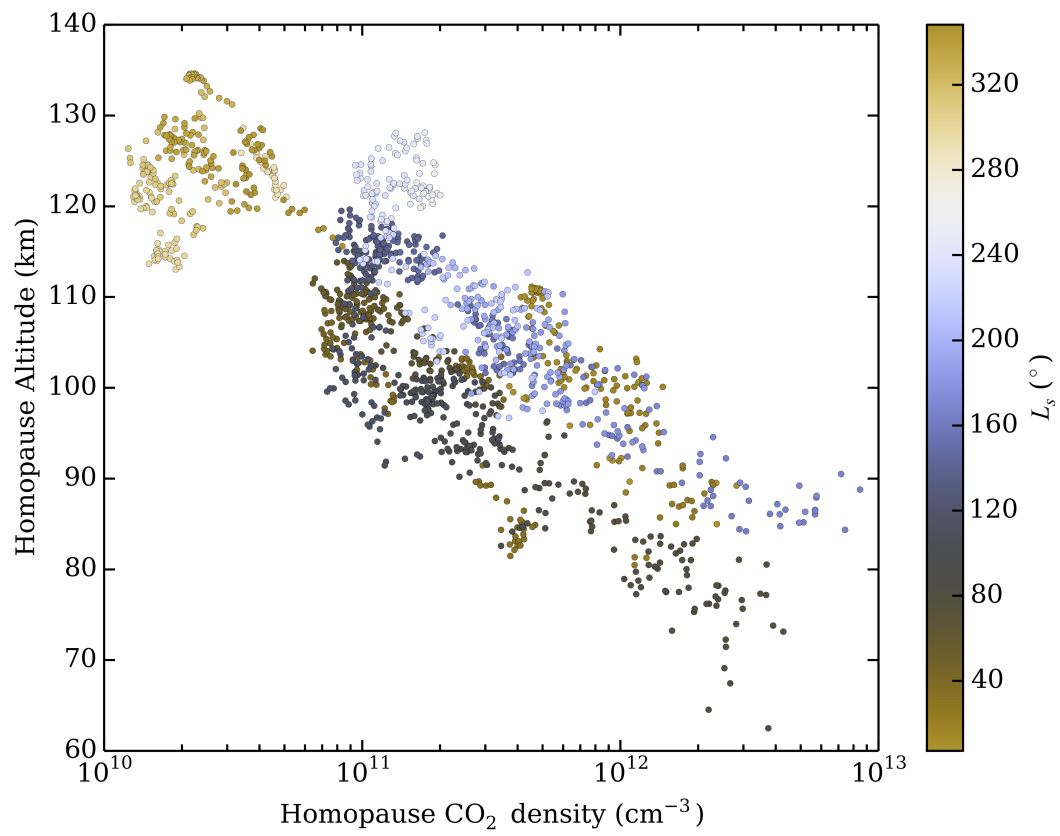


Figure 2.6: Comparison of derived homopause altitudes (same as in Fig. 2.5) and homopause CO₂ densities.

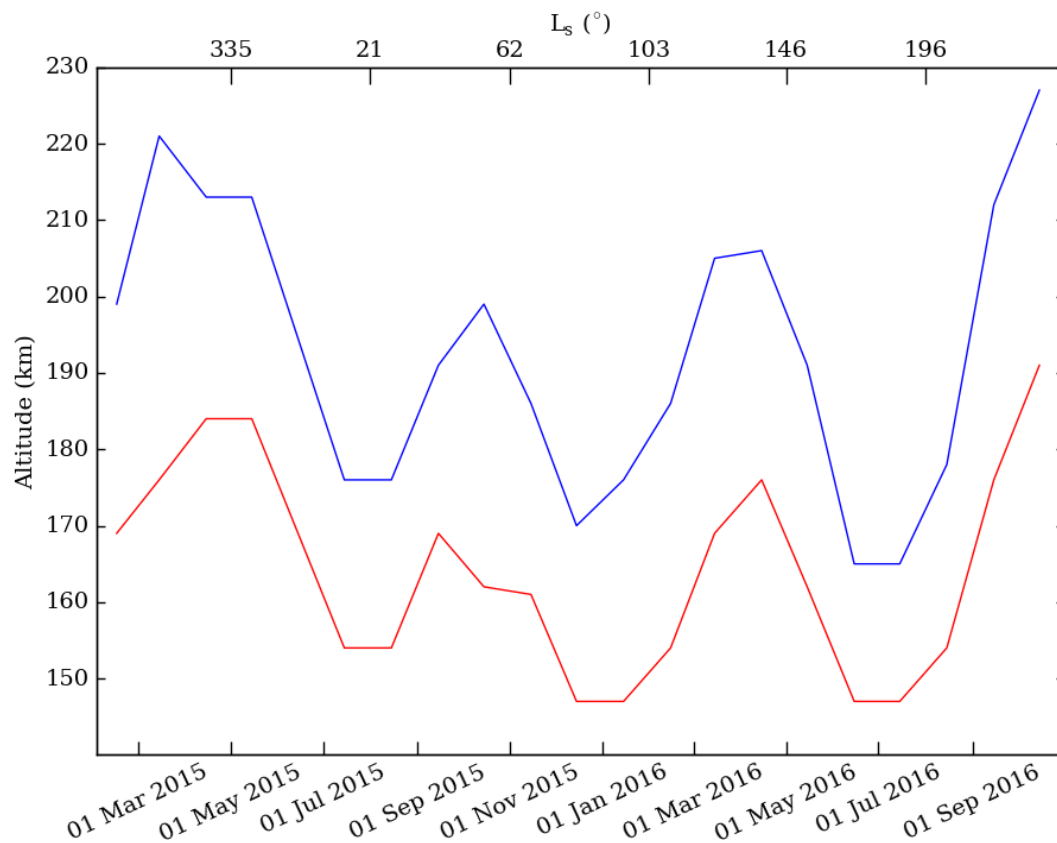


Figure 2.7: Turbopause altitudes derived from $K = D$ (red) and from $\beta_{lin} = \beta_{mol}$ (blue) from Feb 2015 - Oct 2016 (corresponding L_s values are shown at the top). See text for specific parameters used.

about 100 km, assuming a constant H of 10 km. Increasing to $c-u = 100$ m/s raises the turbopause by 30 km. A factor of 10 change in the horizontal wavelength only varies the turbopause altitude by 2 – 5 km in either direction. Thus, we do not believe the turbopause altitudes shown in Fig. 2.7 to be representative of the true turbopause altitude. However, if the phase speed of the waves that break/saturate in the middle atmosphere do not vary wildly from the locations and seasons of our data set, these altitudes will be higher or lower by the same amount each month, meaning the variability is real. We discuss both the high turbopause altitudes and trends in time of both the homopause and turbopause altitudes in more detail in Section 2.4.

So far we have shown that the background atmosphere at low altitudes is characterized by a negative temperature gradient, such that it is reduced in stability. Additionally, standard deviation in temperature increase less than exponentially with altitude. This suggests that dissipation, and thus the generation of turbulence, is strong in this region. There is strong month-to-month variability in the standard deviations at 70 km. Between about 120 and 160 km, there is a large, positive temperature gradient and the atmosphere is statically stable. This allows waves to propagate freely, which is reflected in the large increase in wave amplitudes with altitude. Above 160 km the temperature becomes isothermal such that its stability is reduced and β_{mol} is large, causing wave amplitudes to decrease less than exponentially.

From these distinct vertical regions, we have estimated the altitude at which the atmosphere changes from strong to weak dissipation using the profiles of temperature standard deviations, described in the previous section. Linear fits to the two regions in June 2016 result in a wave-turbopause altitude of 90 km, as shown in Fig. 2.3. Unfortunately, because periapse is often too high to make measurements below the isothermal region, we cannot calculate the wave-turbopause for every month individually. Our results range from 82 – 135 km. As described in Section 2.2, the months were divided into four groups. The wave-turbopause altitudes for months with a strong indication of freely propagating waves in the lowest altitudes measured by NGIMS (increasing T , large N^2 , and large positive gradient in the temperature standard deviations) are shown by the black bars in Fig. 2.5 alongside the homopause altitudes. If we vary the top and bottom altitude

boundaries of the fit to the MCS data we find the wave-turbopause can change by about 10 km. Raising the top altitude of the fit to the NGIMS temperatures can have a drastic effect because the standard deviations do not continue to increase above that altitude. If it is lowered, the variation is about 5 km. There is also some uncertainty in the wave-turbopause because we do not have full profiles of the standard deviations in the middle atmosphere, which we take to be at least 5 km. Additionally, as mentioned above, the standard deviation at a given altitude in the thermosphere may deviate by about 10 K, which acts to increase or decrease the wave-turbopause by 10 km. Taken in quadrature, this represents an uncertainty of 16 km. For those months, the wave-turbopause and homopause altitudes are within about 15 km. The wave-turbopause altitudes for the other groups are shown by the gray bars. For these, 16 km should be considered the lower limit of the uncertainty in the wave turbopause. We display all data where $N^2 > 1.3 \times 10^{-4} \text{ s}^{-2}$ and $D_{mol} < 5 \times 10^6 \text{ m}^2/\text{s}$ and the combined fits in Fig. 2.8, which produce an "average" wave-turbopause altitude of 93 km .

2.4 Discussion

The results presented in the last section are consistent with the established view for Earth with regard to stability and wave propagation in the middle and upper atmosphere. That is, below the transition region (<80 km), the atmosphere is reduced in stability and waves dissipate; N^2 is low and wave amplitudes (assessed by standard deviation in temperature profiles) increase less than exponentially with altitude. In the lower thermosphere, where the atmosphere has high static stability and molecular viscosity is not too high, wave amplitudes increase exponentially with height as waves propagate more freely. The fact that the highest standard deviations at 70 km occur when the homopause is low (60 – 90) km suggests that we may be seeing the transition to steeply increasing wave amplitudes near the homopause altitude. Above about 160 km, N^2 decreases as the atmosphere becomes isothermal and molecular viscosity becomes larger than eddy diffusion. These changes lead to further wave dissipation which results in temperature standard deviations that remain approximately constant with altitude. The standard deviations do not drop off precipitously because some waves are still present, even at 200 km (Yiğit et al., 2015; Terada

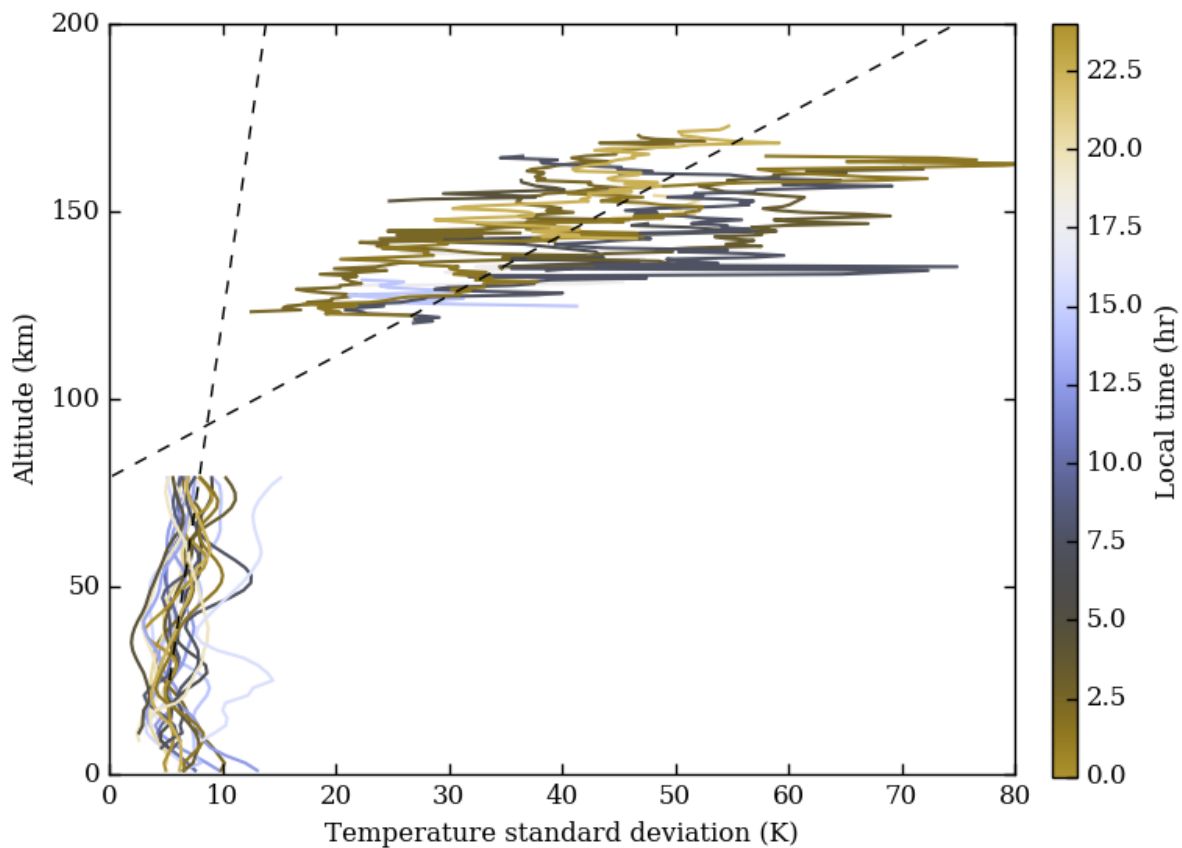


Figure 2.8: Monthly averaged temperature standard deviations where $N^2 > 1.3 \times 10^{-4} \text{ m}^2/\text{s}$ and $D_{mol} < 5 \times 10^6 \text{ m}^2/\text{s}$ for all months. Black dashed lines are fits to the data where the intersection marks the wave-turbopause (see text for more details).

et al., 2017). The homopause and wave-turbopause lie in this transition region, between 80 – 140 km. While this general picture explains the observations of stability and wave amplitudes, differences in local conditions can lead to much different turbo/homopause altitudes, which may be important for understanding the effects of waves in the upper atmosphere. Below, we discuss how the homopause and turbopause correlate with CO₂ densities. That the homopause does not sit at a fixed density level has implications for the strength of eddy diffusion at the homopause, which may be driven by differences in the waves that break/saturate in this region. We briefly remark on how this relates to our very high turbopause altitudes and effects these waves may have on the mesosphere and thermosphere.

The CO₂ densities at 180 km are between 10⁶ and 10⁹ cm⁻³. They are plotted as a function of local time, latitude and season in Fig. 2.9. The minimum CO₂ densities are seen between 0 - 5 AM. The CO₂ distribution generally mimics the background temperature — low on the nightside and near the morning terminator and high on the dayside decreasing at the evening terminator (Bougher et al., 2015; Valeille et al., 2009). Such systematic trends in solar zenith angle have been observed in thermospheric densities and in models (e.g., Zurek et al. (2017); Bougher et al. (2017)) and are due primarily to solar EUV variation.

The correlation between the CO₂ densities at 180 km and the homopause altitudes is clear. A maximum in both the CO₂ densities and homopause altitudes is observed near noon (Fig. 2.9). Fig. 2.9 demonstrates the possibility of a seasonal change in densities and homopause altitudes as well. Around noon the largest values are observed between 240° – 360° L_s (lighter and gold colors) and the lowest values are between ~50° – 180° L_s (darker colors). The variation across seasons at that local time is about 30 km. The CO₂ densities at $L_s \sim 280^\circ$ around the morning terminator are much higher than for other seasons where the latitudes sampled are much nearer to the southern pole (-50° to -70°). Around midnight for $L_s \sim 90^\circ$ (latitude ~50°), CO₂ densities are much higher for those nearer equinox, but the homopause does not show a relative increase even though one might be expected in the northern hemisphere at this season from reinforced general circulation (González-Galindo et al., 2009).

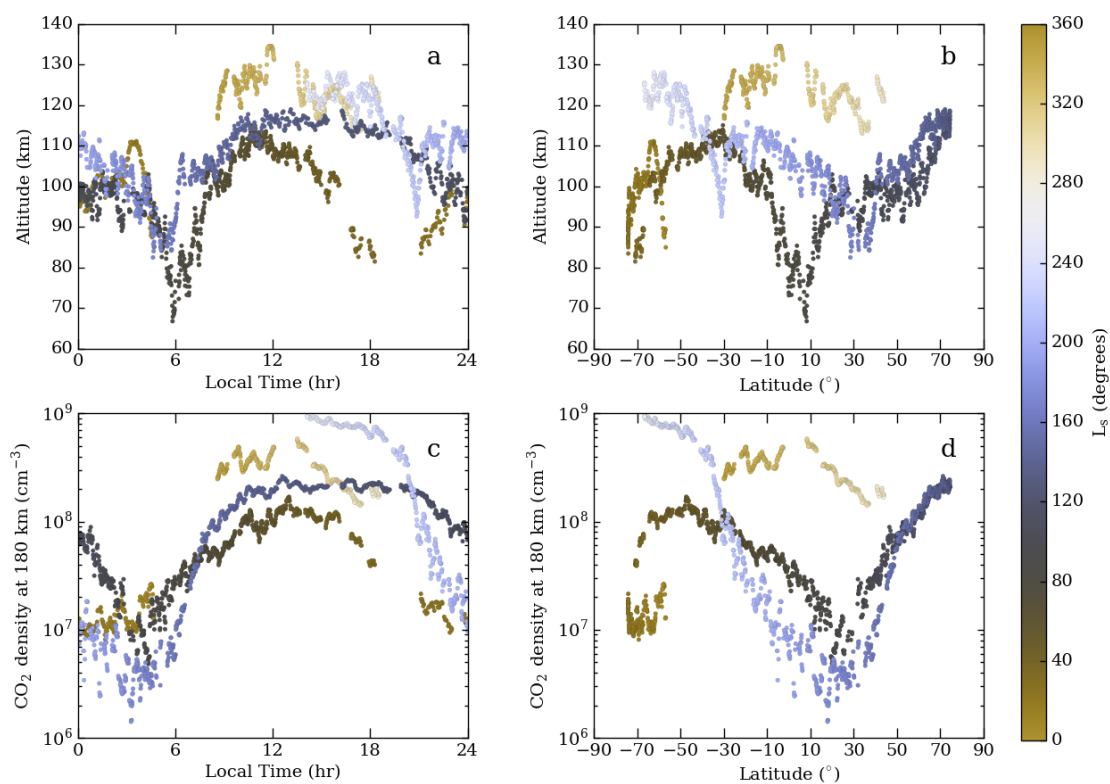


Figure 2.9: Homopause altitudes (top) and CO₂ densities (bottom) shown in Fig. 2.5 as a function of local time (left) and latitude (right). Colors correspond to seasons.

We interpret this to mean that the variability we see in both the homopause and turbopause altitudes is, as expected, controlled by the strength of molecular viscosity in the middle atmosphere (proportional to n^{-1}). Where the density at a given altitude is much lower than average, the molecular viscosity is much higher. The profiles of the eddy diffusion coefficient — as calculated by Eq.2.4 — vary much less month-to-month than the densities; H and N^3 do change, which affects the turbopause altitude, but this is small compared to the order of magnitude changes in densities (Fig. 2.9). Thus, there is a straightforward relationship between the density variations (driven by solar forcing) and the homopause altitude variations. However, a few observations suggest that thermospheric density variations do not fully explain the long term trends in the turbopause level. For instance, the wave-turbopause altitudes rely only on the temperature standard deviation profiles, which are not obviously explained by solar EUV variations. In addition, the homopause density level is not constant. If the homopause and turbopause altitudes were merely a response to the variation of densities with altitude as the thermosphere expands or contracts, then while their altitudes move up and down, the density or pressure levels at which they occur should not. That is, because the altitude at which $K = D$ is governed by n (discussed below), variability of thermospheric densities should change the turbopause altitude but not the density level. However, we see homopause density levels that differ by three orders of magnitude.

Lower and middle atmospheric processes likely play a role as well. Changes in the solar forcing, dust loading, and global circulation are responsible for spatial and temporal variations in thermal structure at middle altitudes. These drive variations in the static stability profile of the atmosphere. Fig. 2.10 demonstrates how these conditions vary throughout the course of a Mars year (on the dayside at 30° N). The seasonal temperature change is shown in Fig. 2.10a. The cold temperatures near the aphelion season around 50 – 70 km are accompanied by an increase in the static stability (Fig. 2.10c) and an increase in the temperature standard deviations (Fig. 2.10b). Conversely, the higher temperatures and lower stability for $L_s > 200^\circ$ at those altitudes have lower standard deviations. Because the homo/turbopause altitudes are inversely correlated with high standard deviations at 70 km, we would expect the homo/turbopause to be lower in summer and

higher in winter for the example in Fig. 2.10. While measurements of the mesosphere are limited, changes in mesosphere altitudes and temperatures with season and latitude are clear in Forget et al. (2009). Indeed, N^2 at 70 km shown in Fig. 2.4 can differ by up to a factor of 2 and the maximum N^2 values vary in the MCD profiles by 25%. Because the static stability affects wave dissipation and propagation, changes in those profiles will affect the temperature standard deviation profiles and lead to variations in the turbopause. When the region of reduced stability is lower, waves dissipate at lower altitudes. And when the stability increases rapidly at lower altitudes, waves that propagate into the thermosphere will grow more rapidly at lower altitudes. This causes the standard deviation at a given altitude in the middle atmosphere to be larger at times when the N^2 minimum is lower, which is shown in Fig. 2.10. So, we argue that the homo/turbopause level is set by the generation of turbulence from wave dissipation and the strength of molecular viscosity. We attribute the variations in those levels to the changing mesospheric and thermospheric conditions brought about by heat flux, solar EUV, and global circulation.

The variability in homopause densities may shed light on the which waves break/saturate in the middle atmosphere. If, instead of relying on our calculated turbopause altitudes (discussed below), we assume that the homopause is equal to the turbopause, then, using Eq. 2.3, we find eddy diffusion coefficients between $12 \text{ m}^2/\text{s}$ at the lowest homopause levels to $1.2 \times 10^4 \text{ m}^2/\text{s}$ at the highest levels. Table I in Leovy (1982) lists predictions of expected values of K near the homopause if governed only by the breaking of a particular tidal mode. He calculated that the sun-asynchronous semi-diurnal wave-4 mode would meet the breaking conditions to produce a dominant eddy diffusion coefficient of $4.5 \times 10^3 \text{ m}^2/\text{s}$. While this is consistent with some of the homopause altitudes, that we find a range of three orders of magnitude suggests that this mode is not always responsible for setting the turbopause altitude. Leovy (1982) concluded that several wave modes with smaller temperature and velocity perturbations were unlikely to break. It may be that in some locations, those modes that can generate $K \sim 10^4 \text{ m}^2/\text{s}$ do indeed break, such as the sun-asynchronous semi-diurnal wave-3 mode or the topographically generated semi-diurnal eastward wave-2 mode. And, for the lowest homopause levels (highest CO_2 densities), modes that produce

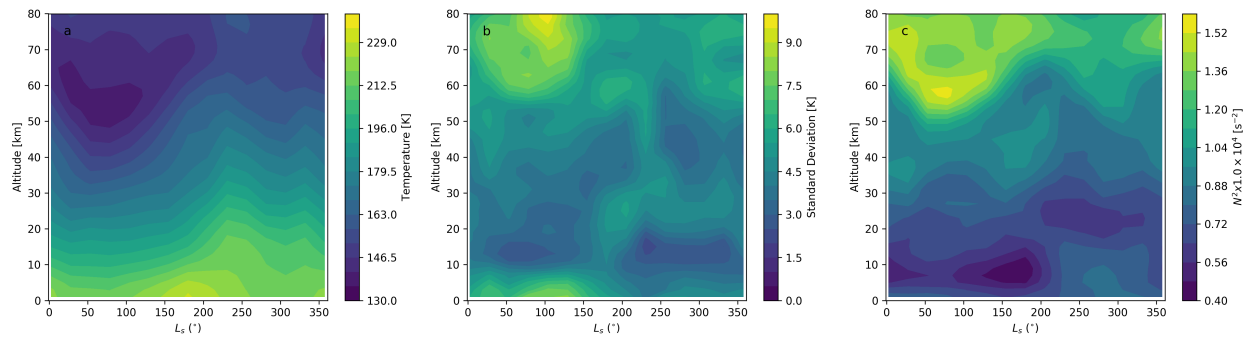


Figure 2.10: (a) Temperature, (b) temperature standard deviations, and (c) N^2 at 30° N around 3 PM as a function of L_s from MCS.

lower values of K (solar driven diurnal tides or gravity waves) between 10 – 100 m²/s may be the dominant breaking modes.

Our derived turbopause altitudes are always above our homopause and wave-turbopause altitudes. As noted in Section 2.3 the uncertainty in the turbopause altitudes is due to the strong effect of $(c - u)^4$. The 70 – 100 km (50 – 70 km for $\beta_{lin} = \beta_{mol}$) difference between the turbopause and homopause altitudes can be accounted for if $c - u$ is about an order of magnitude lower than the assumed 50 m/s. This suggests that smaller phase speeds are more likely to be the dominant waves undergoing saturation and dissipation below the turbopause. It may also mean that winds on the order of 10 m/s are important for reducing $c - u$, though a paucity of wind measurements preclude quantifying their role here. However, the turbopause and homopause altitudes need not be equal. In fact, Chabrilat et al. (2002) showed that for Earth, the impact of molecular diffusion of CO₂ on the temperature structure just below the turbopause ($D_{mol} < K$) is important enough to force the homopause to be below the turbopause. It may be that some of the disagreement between the turbopause and homopause altitudes is real, though likely not the magnitude we have found here.

Gravity waves that dissipate near the turbopause or propagate into the thermosphere can be formed by a variety of mechanisms: topography, convection, wind shear, and wave-wave interactions. Though work has been done to understand the expected wavelengths and amplitudes of topographically generated gravity waves (Fritts et al., 2006; Spiga et al., 2012), observations show no significant correlation with topography (Creasey et al., 2006; Wright, 2012). Imamura et al. (2016) showed gravity waves generated by boundary-layer convection can propagate into the thermosphere. Observations by Yiğit et al. (2015) and Terada et al. (2017) demonstrated that waves are present high in the thermosphere. Yiğit et al. (2008) have shown that waves with higher phase speeds and directed against the zonal mean wind are more likely to avoid selective filtering below the transition region and propagate upward into the thermosphere. So, our results suggest that the waves propagating with a near exponential increase in amplitude between 120 – 160 km have high speed and are moving against the background wind. Of course, it need not be the case that

the waves that influence the lower-middle atmosphere standard deviations have the same origin as those that influence the thermospheric deviations. And, the standard deviations are the average of the perturbations of the background atmosphere over the course of a full month where any individual profile may contain a superposition of waves — the averaged profiles do not show the vertical propagation of any single wave.

The waves that propagate into the thermosphere with high phase speeds will produce greater gravity wave drag and have a larger effect on dissipative heating and differential gravity wave heating or cooling. Whether the dissipation in the thermosphere is predominantly due to molecular viscosity (or possibly ion drag) as opposed to convective instability is unclear. Models suggest molecular viscosity is more important than linear saturation in the thermosphere and show a decrease in wave amplitudes (Yiğit et al., 2008, 2015). However, we see relatively constant standard deviations in temperature above 160 km from dissipation. It could be that breaking/saturation occurs in addition to dissipation due to molecular viscosity. Indeed, the waves observed up to 250 km at Mars show an inverse relation with temperature which may suggest that saturation is damping the waves' amplitudes (Terada et al., 2017). We see a decrease in the static stability with altitude above 140 km which fits with this interpretation — the atmosphere is reduced in stability again in the thermosphere causing waves to dissipate from saturation, limiting their amplitudes.

MCS is insensitive to short wavelengths, so temperature perturbations below 80 km may be biased to those from long wavelength waves. Models predict that gravity wave amplitudes in the lower atmosphere should be ~ 5 K (Imamura et al., 2016), a few K less than the typical standard deviations we observe at those altitudes. Unless many short-wavelength features are frequently superposed, these should only slightly increase the standard deviations observed in the lower atmosphere. We know that short wavelength waves grow to very large amplitudes in the thermosphere (Fritts et al., 2006) and models estimate the perturbations may be as high as 50 K from 50-100 km (Imamura et al., 2016). Thus, the standard deviations at the highest MCS altitude — where short wavelength amplitudes begin to grow very large — may be too low. If the MCS standard deviations above 50 km are lower than reality due to insensitivity to short wavelengths,

the wave-turbopause altitudes will be systematically high. However, the perturbations from longer wavelength waves should also grow exponentially, so we still see a lack of freely propagating waves in the lower-middle atmosphere. Furthermore, visibility — the insensitivity to short-wavelengths — is a well known problem for limb sounders of Earth’s atmosphere and has been shown to have little effect on the increase in temperature fluctuations with altitude (Preusse et al., 2006). Performing a similar analysis for the MCS observations would be necessary to conclude the same here, though that is beyond the scope of this work. Indeed, a better understanding of the wave spectrum at all altitudes will help in interpreting dissipation and its effect on the turbopause as well as wave-coupling and wave sources.

N_2/Ar ratios give homopause altitudes assuming the transition to diffusive separation happens instantaneously. This essentially constitutes the topmost altitude in the transition from eddy diffusion to diffusive separation. Within the transition region, K must be comparable to D_{mol} , though they need not be equal. Lindzen (1981) found that the turbulent diffusion may decrease rapidly after the breaking region, which occurs as $|c - u|$ approaches 0. This may explain why some waves can propagate freely after dissipation is strong, but before molecular viscosity is large enough to dissipate. However, measurements of the zonal winds and more observations of wave activity between 80 and 140 km will be necessary to investigate this further. We expect that the waves in this region will have phase speeds close to the background zonal wind. Larger wave amplitudes at lower altitudes lead to earlier breaking. If waves break earlier the turbopause will occur at a lower altitude and the gravity wave drag produced by the dissipation should be stronger at lower altitudes. This should produce turbulence at lower altitudes and reduce the altitude of the maximum zonal wind (Rapp et al., 2004). So, where we observe the lowest turbo/homopause, we expect there should be an accompanying reduced altitude of maximum zonal wind.

It is worth noting that in July and Aug 2015 (L_s 7 – 35°) measurements were made below 48°S and in each of those months we see the temperature inversion that enables a region of low static stability above 50 km studied by Heavens et al. (2010). The reduction in stability is accompanied by a slight decrease in temperature standard deviations due to damping. A similar sharp reduction

in stability is seen for June 2016 (L_s 161–178°) in Fig. 2.3, though here the measurements are from midlatitudes. The homopause altitudes derived for these months are below the average homopause altitude. It is possible that the strong dissipation from these unstable regions at low altitudes lowers the turbopause altitude. However, more information is needed between 80 and 100 km to draw any further conclusions.

2.5 Conclusions

To summarize, we have used temperatures from MCS and densities from NGIMS to investigate the transition from strong to weak wave dissipation and from turbulence to molecular diffusion. Our homopause altitudes, derived from a simple extrapolation of N_2/Ar , are between 60 – 140 km. The variability in homopause altitudes is a direct result of observed CO_2 densities in the lower thermosphere, which vary with local time, latitude, and season (highest at high summer latitudes near noon, lowest on the nightside especially near 5 AM). A lower density implies that at a given altitude the molecular viscosity is larger such that the altitude where molecular diffusion becomes more dominant than eddy diffusion is lower. This means a lower turbopause altitude. We showed this by choosing a set of wave parameters and estimating the the turbopause using CO_2 densities measured by NGIMS and comparing to our derived homopause altitudes. The homopause is not set at a constant value of n_{CO_2} and the variation of the density at the homopause suggests that K can vary from $10 - 10^4$ m^2/s in the transition region, likely from changes in the dominant breaking waves.

While the variability of the homopause is determined by changes in molecular viscosity, the precise altitude at which the turbopause or homopause occurs is related to both the molecular viscosity and wave propagation in the middle atmosphere. We have shown that below 80 km the atmosphere is reduced in stability such that breaking/saturation damps wave amplitudes characterized by low temperature standard deviations (~ 10 K) increasing slowly with altitude. This dissipation produces turbulence. Below 160 km in the thermosphere, the atmosphere is much more stable, and waves can propagate more freely, such that their amplitudes increase rapidly; temper-

ature standard deviations increase ~ 30 K from 120 – 160 km. The highest standard deviations at 70 km are seen when the homopause is lowest, indicating that the region of rapidly increasing wave amplitudes extends down to 70 km. The lack of dissipation implies that turbulence generation is much less than it is at lower altitudes. The standard deviations at 70 km are inversely correlated with the homopause altitudes and thus are highest on the nightside and near 5 AM and lowest near noon near $L_s > 200$. Their variability is driven by the temperature profile and static stability of the lower atmosphere, so conditions that lead to colder temperatures near 50 km and corresponding lower altitudes of higher stability (nightside, $L_s \sim 90^\circ$), generate higher standard deviations at 70 km. So, we have used changes in wave amplitudes as an estimate for the turbopause — we have extended the wave-turbopause concept of Offermann et al. (2006) to Mars, calculating the altitude reliably for 5 individual months and finding agreement within about 15 km of the corresponding monthly averaged homopause altitudes. Above about 160 km, the atmosphere is again reduced in stability and the molecular viscosity is high, which suggests that there is some dissipation so that amplitudes, on average, cease to grow exponentially with altitude. Wave damping could be due to molecular viscosity or breaking/saturation. However, waves continue to propagate, as the temperature standard deviations are still large (40-80 K).

The variation in turbopause altitudes means that energy, mass, and momentum transported vertically are deposited at different altitudes across the planet. This can have an effect on the thermal and dynamical state of the middle-upper atmosphere. Though we cannot identify the sources of the vertically propagating waves, their dissipation below 80 km and above 160 km will deposit momentum and cause drag on the background winds. Additionally, lower homopause altitudes will cause species to diffusively separate out at much lower altitudes, increasing the relative abundance of lighter constituents at the highest levels of the atmosphere. Thus, neutral loss processes, like sputtering, will fractionate isotopes more readily at these locations. Or, if sputtering is restricted to specific spatial locations, those homopause altitudes will be the most important for inferring total atmospheric loss from isotopic ratios.

Chapter 3

Fractionation of Ar isotopes in the upper atmosphere

3.1 Introduction

While the variability of the homopause has implications for the dynamics and thermal structure of the mesosphere and thermosphere, it also suggests that the relative abundances of isotopes at the exobase changes with time and space. Here, we use MAVEN NGIMS data to derive two other quantities, the exobase altitude and the scale height of ^{40}Ar to determine the fractionation of ^{36}Ar and ^{38}Ar in the upper atmosphere (Section 3.2). We show that the derived scale heights are consistent with diffusive separation above the homopause. In addition, direct sampling of ^{36}Ar and ^{38}Ar measured during one deep dip verify this holds for Ar isotopes as well. Using the concept of Rayleigh distillation, we estimate the total amount of ^{36}Ar and ^{38}Ar (Section 3.3). The variability in the derived quantities leads to fractionation values and loss estimates that are spatially and seasonally dependent.

3.2 Data and Methods

Here, the data used is nearly identical to the NGIMS data used in Chapter 2. To restate, these are densities of major atmospheric species in the upper atmosphere measured every orbit. While data is taken during both inbound and outbound (relative to periapse) segments, we restrict our use to inbound data because of increased background levels from CO_2 adsorption after periapse. We only consider data from Feb 2015 - July 2016, a few months short of the time period used in the previous chapter. Instead of using a rolling average of 2 days (7-11 orbits), in this chapter we

consider each orbit individually. This increases the orbit-orbit variability in some of the derived quantities due to a more pronounced effect of waves and horizontal motion in single profiles. While the spatial and seasonal results are unaffected, by not averaging over several orbits our range of estimates for the total loss of Ar remains conservative. Homopause altitudes are derived by extrapolating $N_2/^{40}\text{Ar}$ downward to the lower atmospheric value of 1.25 as described in Section 2.2.

3.2.1 Exobase altitudes

From the neutral density measurements, we can calculate the exobase altitude using simply the definition, where the scale height of the atmosphere, H , equals the mean free path, λ . The mean free path is the average distance a particle travels between collisions and is given by

$$\lambda = 1/(n\sigma) \tag{3.1}$$

where n is the number density of colliding particles in the gas and σ is the collisional cross-section, the effective area for collisions between the traveling particle and the particles in the gas. So, the exobase is defined to be where the average distance a particle travels before a collision is an e -folding distance in density. Essentially, above this altitude, particles are on ballistic trajectories and do not collide frequently with other particles.

To derive this altitude from the data, we consider the total number density of the atmosphere at a given altitude, $n(z)$. At the altitudes in the vicinity of the exobase, the atmosphere is primarily CO_2 and O. In truth, σ will be different for every collisional pair and will be dependent on the abundances of each colliding species. However, due to large uncertainty in the O NGIMS measurements, we choose to only use CO_2 in our analysis. Because our focus is on Ar, we use a single value, $3 \times 10^{-15} \text{ cm}^2$ as an approximation of σ for Ar- CO_2 (Lewkow and Kharchenko, 2014; Tian et al., 2013). This effectively provides an estimate of the Ar exobase, since each species will really have its own exobase (as is also the case for the homopause).

To validate this approach, we also derive exobase levels through an analogy with the Beer-Lambert Law for the attenuation of light. That states that the optical depth (τ) is given by:

$$\tau = \sum_{i=1}^N \sigma_i \int_0^l n_i(l') dl' \quad (3.2)$$

where each attenuating species is given by i , σ is the attenuation cross-section, n is still the number density, and l is the path length. Here, the top of the atmosphere is $l = 0$ ($\tau = 0$) and l increases with distance toward the surface. Again, CO_2 and O dominate the density at these altitudes, so we consider CO_2 to be the only attenuating species. We use the same collisional cross-section described above for σ . While any given particle moving through this region will have its own collisional cross-section, this exobase altitude will be valid for any particle with a CO_2 collisional cross-section of about $3 \times 10^{-15} \text{ cm}^2$. Starting from very low densities at high altitudes (300 km), we integrate downward to the altitude where $\tau = 1$. This is essentially one mean free path from the top of the atmosphere, where a particle is unlikely to undergo collisions, and is therefore comparable to the formal exobase definition.

3.2.2 Scale heights

The number density of the atmosphere is given by:

$$n(z) = n_0 e^{-z/H} \quad (3.3)$$

where z is some above some reference altitude, n_0 is the density at that reference altitude, and H is the scale height of the atmosphere. The equation for the scale height is $H = \frac{kT}{\mu g}$, where k is the boltzmann constant, T is the temperature, μ is the mean molecular mass, and g is the gravitational acceleration. Above the homopause, molecular diffusion is much larger than eddy diffusion, so species diffusively separate. Thus, each species has its own scale height above the homopause, and we can rewrite equation 3.3 for an individual species above the homopause:

$$n_i(z) = n_{0_i} e^{-z/H_i} \quad (3.4)$$

We derive scale heights by fitting a line to the log of Eq. 3.4 for a given species,

$$\ln n_i(z) = -\frac{1}{H} z + \ln n_{0_i} \quad (3.5)$$

where the slope of the fitted line gives the scale height. We are interested in the fractionation between the homopause and exobase, but because periapse is usually above 140 km, we use an upper limit for the fit 30 km above the exobase. With periapse as the lower limit, the full range is roughly 150–200 km extending to ~ 125 –200 km during deep dips. The upper boundary varies by about ± 20 km. The $\text{N}_2/^{40}\text{Ar}$ ratio shown in Fig. 2.2 increases with increasing altitude as expected for diffusive separation above the homopause. We validate that this is indeed the case by deriving scale heights for N_2 , CO_2 , and ^{40}Ar and comparing the temperatures.

3.2.3 Fractionation

Because the low abundance of ^{36}Ar and ^{38}Ar ($\sim 10^3$ smaller than ^{40}Ar) precludes accurate determinations of their densities at MAVEN’s nominal altitudes we cannot simply measure their ratio at the exobase during each orbit. However, during deep dip campaigns MAVEN’s lowered periapse enables NGIMS to sample higher density regions (about 25 times higher) where its sensitivity is sufficient to determine the ratio of $^{36}\text{Ar}/^{38}\text{Ar}$. The ratio measured during 25 orbits from deep dip 4 (Sept 2–10 2015) is displayed in Fig. 3.1. There is significant noise above 145 km because of the low count rates. At the highest densities sampled below 125 km collisional scattering inside the instrument leads to an increased background level of all mass channels (Stone et al., 2015). This results in an increase in the noise in the isotope ratio below 125 km. Between 125–145 km the data appear to behave as expected from the observations in Section 3.2.2. The purple line shows the fractionation from the two species calculated from Eq. 3.4 with a temperature consistent with the scale heights of N_2 , CO_2 , and ^{40}Ar . The green line is the best fit to the data between 125

and 145 km. That fit confirms that ^{36}Ar and ^{38}Ar diffusively separate above the homopause in agreement with the scale heights derived from the major atmospheric species. Thus, we can use those atmospheric species to determine the fractionation of Ar isotopes from the homopause to the exobase for all orbits in the data set.

The ratio of two species, x and y at some altitude is

$$R_{x/y}(z) = \frac{n_x(z)}{n_y(z)} = \frac{n_{0x}}{n_{0y}} e^{-z(\frac{1}{H_x} - \frac{1}{H_y})} \quad (3.6)$$

We are interested in the fractionation between species from the homopause to the exobase, which is just the ratio of their ratios that at the exobase, $R_{x/y}(z_{exo})$, to the homopause, $R_{x/y}(z_{hp})$. Letting the homopause be the reference altitude and $\Delta z = z_{exo} - z_{hp}$, the fractionation, which we will define as a , is:

$$\frac{R_{x/y}(z_{exo})}{R_{x/y}(z_{hp})} = a = e^{-\Delta z(\frac{1}{H_x} - \frac{1}{H_y})} \quad (3.7)$$

Because the scale heights are related by temperature and μ is just the mass for a given species, we can rewrite equation 3.7 as

$$a = e^{-\Delta z \frac{g}{kT}(\mu_x - \mu_y)} = e^{-\Delta z \Delta \mu \frac{g}{kT}} \quad (3.8)$$

where $\Delta \mu$ is the mass difference between the two species. In terms of a scale height of some arbitrary species w (instead of temperature),

$$a = e^{-\Delta z \Delta \mu (H_w \mu_w)^{-1}} \quad (3.9)$$

Thus, for any two species we can calculate the fractionation between the homopause and the exobase given the separation between those altitudes (Δz) and the scale height of some species (or temperature) in that region.

For ^{36}Ar and ^{38}Ar , $\Delta \mu = -2$ amu (atomic mass units). In the chapters above we calculated Δz and the ^{40}Ar scale height, so we can calculate the fractionation of ^{36}Ar and ^{38}Ar :

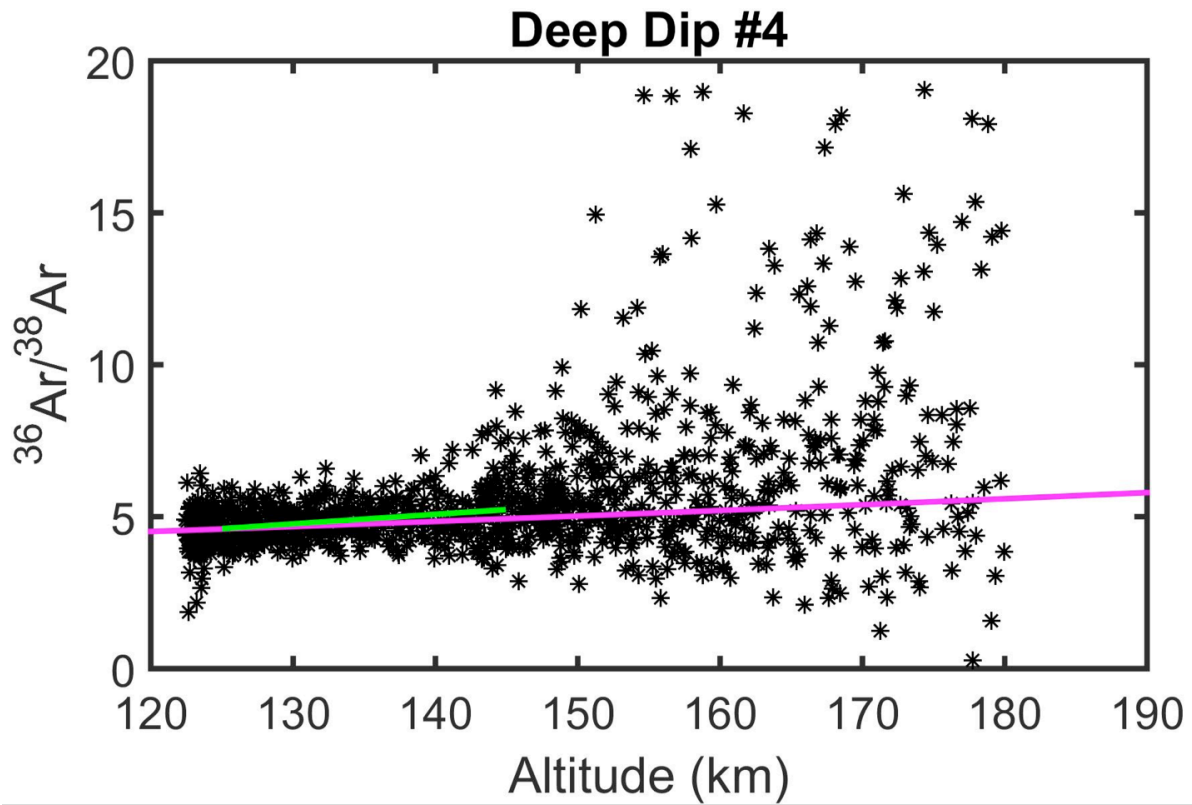


Figure 3.1: Measured ratio of $^{36}\text{Ar}/^{38}\text{Ar}$ as a function of altitude during deep dip 4 (black stars). Overplotted are a best fit line (green) and the expected fractionation assuming a temperature consistent with those observed during the Deep Dip 4.

$$a_{36/38} = e^{\Delta z / (20H_{40})} \quad (3.10)$$

3.2.4 Rayleigh distillation

To estimate the total amount of Ar lost to space, we will use the concept of Rayleigh distillation. Rayleigh distillation, or Rayleigh fractionation, describes a system with isotopes of a given atom or molecule where atoms or molecules are lost from the system. The ratio of isotopes in the remaining reservoir relative to the initial reservoir is given by:

$$R/R_0 = (N/N_0)^{a-1} \quad (3.11)$$

where R is the ratio of the heavy isotope to the light isotope, N is the abundance of the light isotope (which is typically much larger than the concentration of the heavy isotope), the subscript 0 indicates initial values, and a is the fractionation factor. The fractionation factor is the ratio at which isotopes are removed from the system. The system has been enriched in the heavy isotope for $R/R_0 > 1$ and depleted for $R/R_0 < 1$. The fraction of gas remaining, $f = N/N_0$, can be expressed in terms of the percent of gas lost from the initial inventory by $1 - f$. In Fig. 3.2, I show the dependence of gas loss as a function of the fractionation factor for different enrichments of Martian isotopes.

The bulk atmosphere represents a reservoir with some present-day isotopic ratio of a given atom or molecule. We assume that particles are removed in proportion to their abundance at the exobase because model results have found Ar and CO₂ sputtering yields per concentration around unity (Jakosky et al., 1994). the fractionation factor is simply the isotopic ratio at the exobase divided by the ratio in the bulk atmosphere, $a = R_{exo}/R_{hp}$. Thus, given the present ratio in the bulk atmosphere and the initial ratio, the fraction of gas lost can be determined. This, of course, neglects any sources or sinks to the bulk atmosphere including outgassing of the interior, impacts, and surface-atmosphere exchanges. Chapter 4 explores this in much more detail.

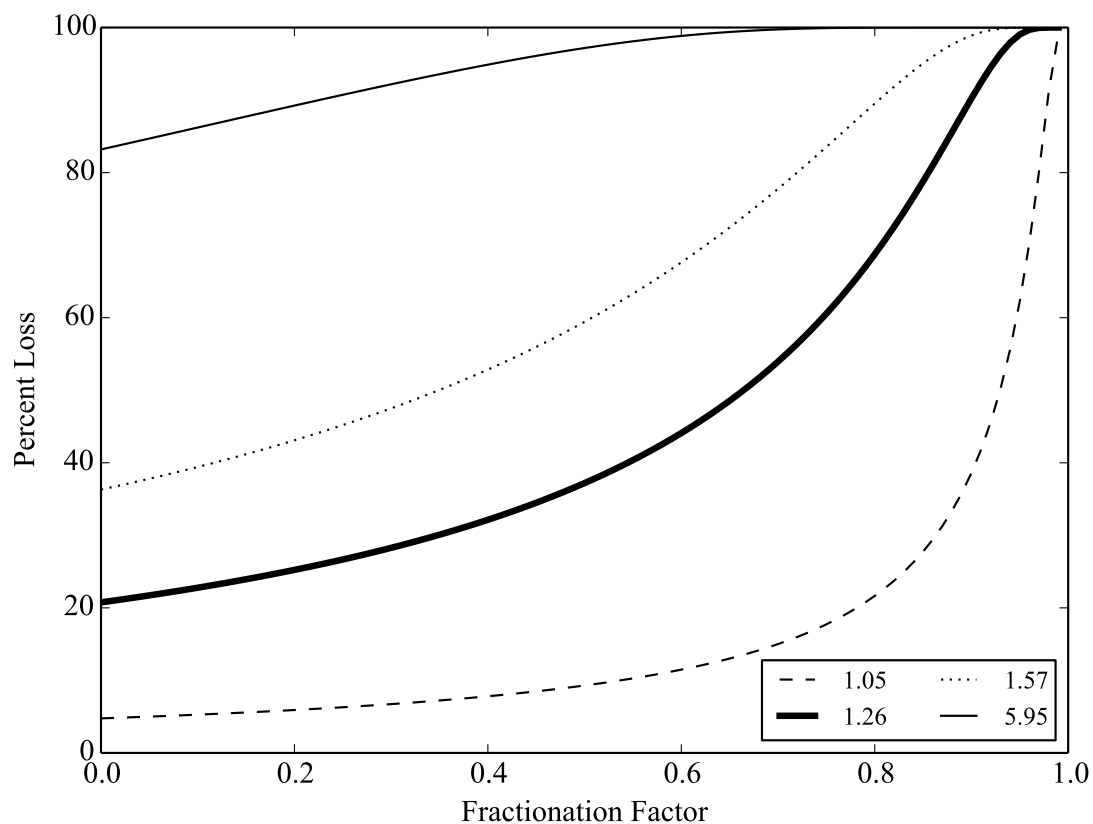


Figure 3.2: Percent of gas lost as a function of fractionation factor for different R/R_0 values (given in legend). Fractionation factors are given in terms of the heavy-to-light isotope ratio. The thick solid line ($R/R_0 = 1.26$) represents the case for Mars' $^{38}\text{Ar}/^{38}\text{Ar}$. Other ratios used correspond to other Martian volatiles (C or O, N, and H) (see Table 1.1).

The present-day isotope ratios for several major volatiles have been measured in-situ from mass spectrometers onboard landers and rovers (Table 1.1), telescopically through spectrometry, and from gases trapped in Martian meteorites. We cannot measure the initial isotope ratio of the atmosphere, R_0 , but we can make reasonable assumptions based on observed isotope ratios in Earth’s atmosphere, the solar wind, and other primitive solar system objects like comets and asteroids. The remaining parameter is the fractionation factor, or the isotope ratios at the homopause and exobase. The ratio of $^{36}\text{Ar}/^{38}\text{Ar}$ in Earth’s atmosphere (Table 1.1) is the same as in primitive solar system objects (see Chapter 4 for a more detailed discussion). Therefore, we assume this was also the ratio in Mars’ ancient atmosphere.

3.3 Results and discussion

In Fig. 3.3 we plot the exobase altitudes derived for every orbit for both methods. The altitudes from the methods show quite good agreement with averages ~ 170 km; they differ on average by about 2 km – the altitudes from the formal definition are systematically higher. This could be due to calibration issues, but is more likely due to the fact that the atmosphere is not isothermal which produces uncertainty in the scale heights. From here on, we use the exobase altitudes from the integration method. The 2 km difference in exobase altitudes does not affect our results. Exobase altitudes are shown along with homopause altitudes across the mission in Fig. 2.5.

The temperatures from each scale height between Feb 2015 and July 2016 are plotted in Fig. 3.5. There is very good agreement between the N_2 and ^{40}Ar temperatures. Variability due to wave activity and the horizontal motion of the spacecraft on a given orbit (as in Fig. 2.2) is evident, up to ~ 10 K. The CO_2 temperatures are systematically lower than the other temperatures, likely resulting from CO_2 adsorption on the walls of the instrument at high altitudes during the inbound segments. The walls become saturated as the spacecraft approaches periapse, but at high altitudes CO_2 can be adsorbed reducing the measured CO_2 count rate and density (Stone et al., 2015). The agreement between all three temperatures confirms diffusive separation of these species through

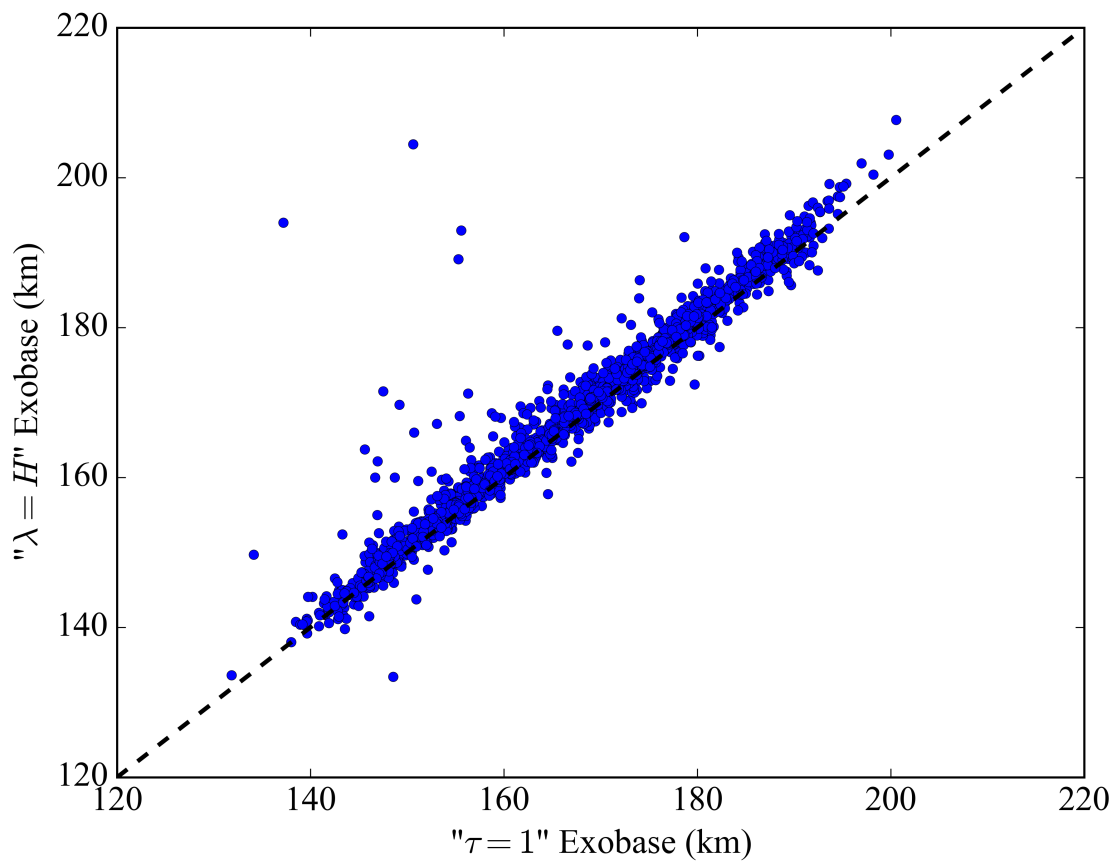


Figure 3.3: Exobase altitude derived from where the scale height equals the mean free path and integrated to where $\tau = 1$. Methods described in text. The dashed black line shows a one-one line.

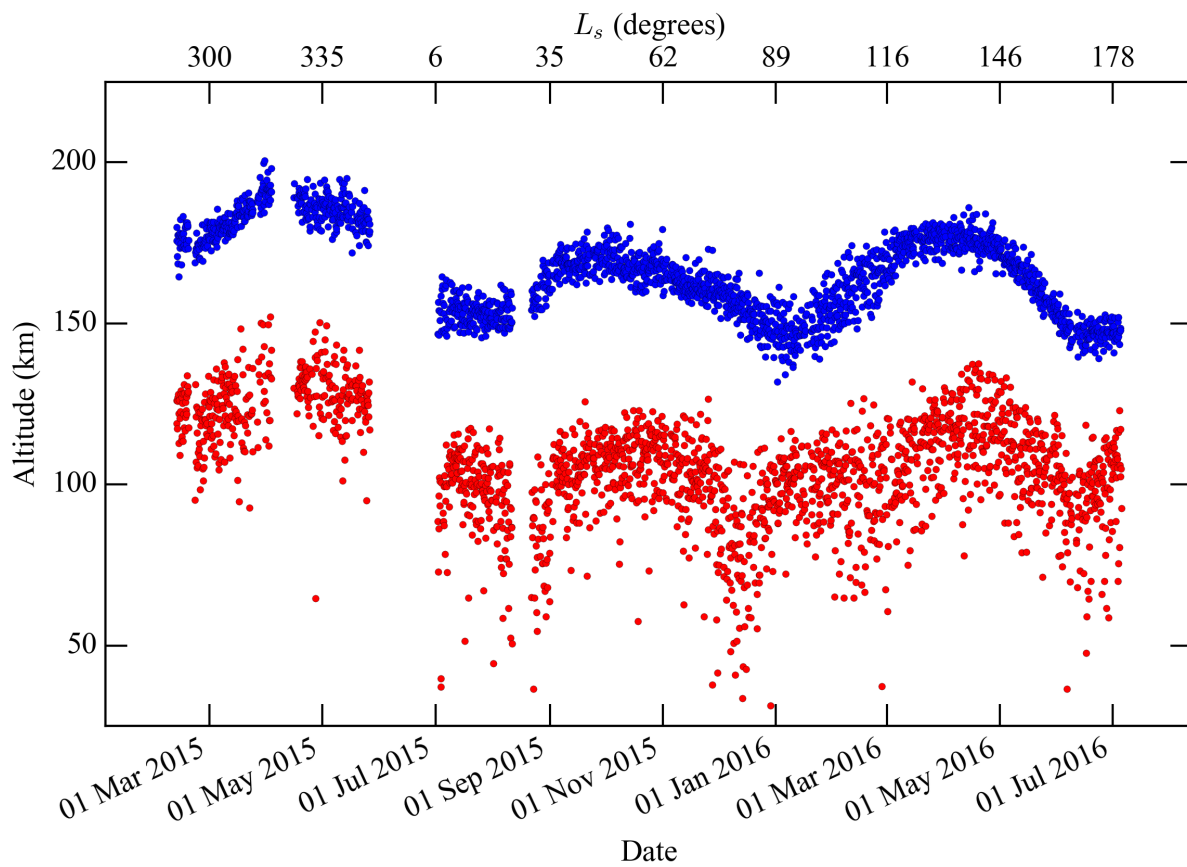


Figure 3.4: Homopause altitudes (red) and exobase altitudes (blue) from Feb 2015 to July 2016.

the entire dataset, suggesting that ^{36}Ar and ^{40}Ar will behave similarly.

In Fig. 3.6 I show how the derived exobase-homopause separation distances and the ^{40}Ar scale heights map to values of $a_{36/38}$. 80% of the points fall between $a_{36/38} = 1.2$ and $a_{36/38} = 1.4$, with a mean value of 1.3.

The largest fractionation occurs when the separation between the homopause and exobase is largest – more distance over which the density of the heavier species falls off more rapidly – and when the scale height (or temperature) is small – a higher drop off in density. The ratio of lengths $\Delta z/H_{40}$ is simply the number of ^{40}Ar scale heights above the homopause. The fractionation increases with more scale heights above the homopause.

In Fig. 3.2 the fraction of ^{36}Ar lost is shown as a function of the fractionation factor. A slight enrichment ($R/R_0 \sim 1$) does not require significant loss (Fig. 3.2, thin solid line) if the gas removed is significantly fractionated; if the gas removed contains only a small proportion of light isotopes, only a small total amount of gas needs to be removed to produce a slight enrichment. Even so, the amount of gas removed must be high if the isotopes are removed from the reservoir at nearly the same ratio as that in the reservoir. For more significant enrichment (higher R/R_0 , dashed line in Fig. 3.2), more loss is required at all fractionation factors.

The thick solid line in Fig. 3.2 shows the percent loss of ^{36}Ar for the observed enrichment on Mars (Table 1.1). Because 80% of orbits fall between $a=1.2$ and $a=1.4$, the corresponding loss values range from 55–75%. The mean value of a corresponds to 63% of ^{36}Ar lost from the initial reservoir. The uncertainty in this value due just to the observed 1-sigma variability in the fractionation is 6%. There is also $\sim 10\%$ 1-sigma uncertainty in the lower atmospheric $\text{N}_2/^{40}\text{Ar}$ value measured by SAM. We have derived homopause values and recalculated the loss estimates and find the mean loss varies by $\sim 1.5\%$. Added in quadrature, the uncertainty in the total loss is $\pm 6\%$.

The highest loss values occur for the smallest Δz and largest H_{Ar} values. For the large Ar scale heights (higher temperature) at low solar zenith angles (dayside, typically from 12 – 18 local time – see Fig. 2.9) and $L_s > 280^\circ$, densities drop off less rapidly, so the fractionation at the

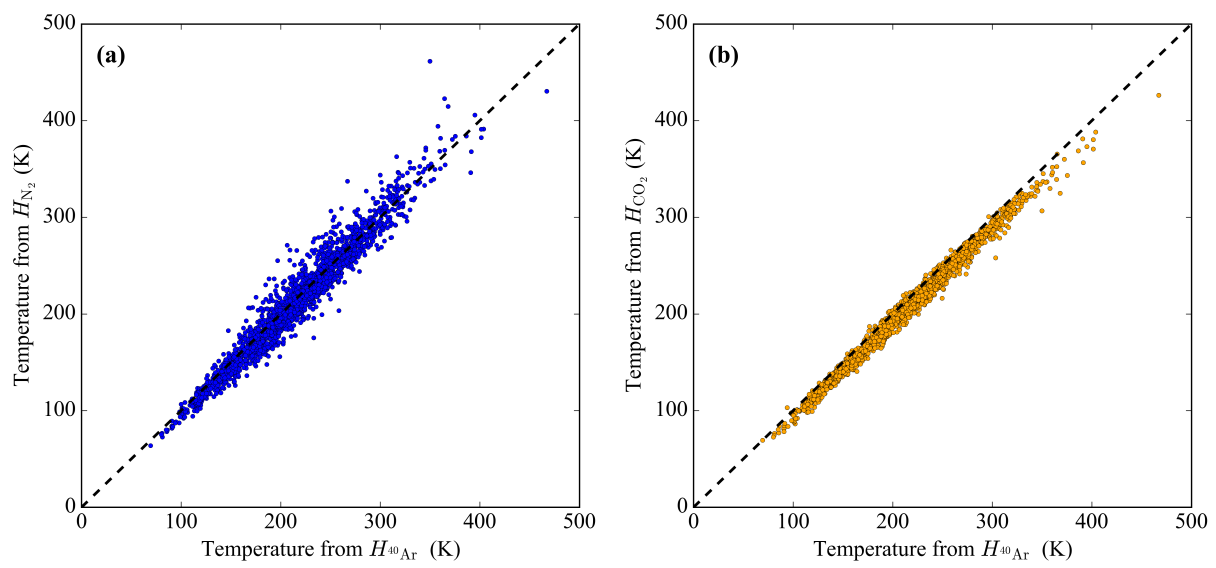


Figure 3.5: Comparison of scale height temperatures derived from (a) Ar and N_2 densities (b) and Ar and CO_2 densities. The dashed black lines are one-one correspondence.

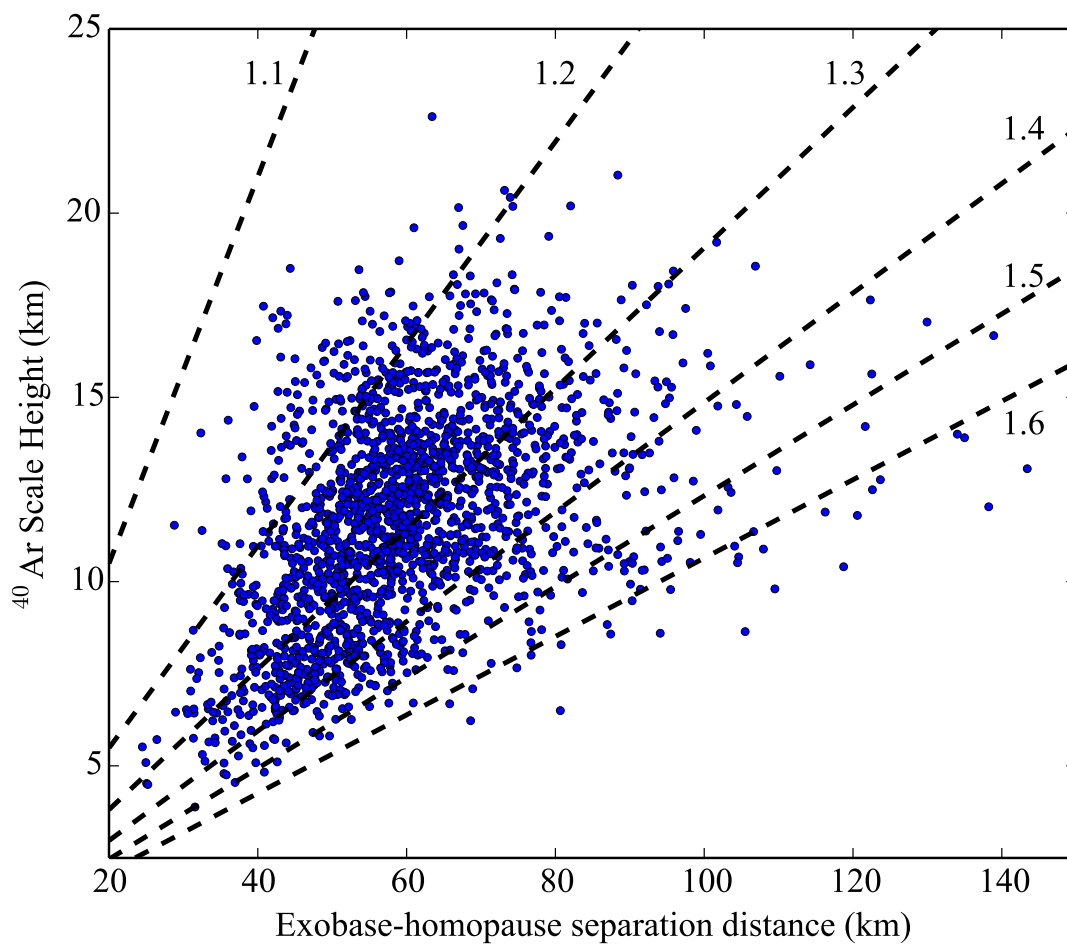


Figure 3.6: Derived exobase-homopause separation distances and H_{40} values from Feb 2015 to July 2016. Black dashed lines show $^{36}\text{Ar}/^{38}\text{Ar}$ fractionation values for $a = 1.1, 1.2, 1.3, 1.4, 1.5, 1.6$ from Eq. 3.10.

exobase is weak. With little fractionation, more total amount of gas must be removed to drive changes in the atmospheric isotope ratio. Similarly, small separations leave little vertical distance for fractionation to occur and necessitating higher loss.

The Rayleigh distillation technique has several limitations. First, it bears repeating that the exobase is really a transitional region and not a sharp boundary, so particles are certainly lost from above and below (where the fractionation will be different). Rayleigh distillation is agnostic to the physical process that remove Ar from the atmosphere, but it assumes the isotopes are removed strictly in proportion to their abundance at the exobase. Any processes that removes Ar at some other ratio are ignored.

Furthermore, we have assigned equal weight to all fractionation factors, though they vary substantially with location and season. If particles are preferentially removed from some region or during some season, then that particular fractionation factor is more representative of the loss through time. As will be discussed in the following chapter, the escape mechanism for Ar is atmospheric sputtering. However, sputtering is not likely to be globally uniform. Models of heavy ion precipitation, the process that leads to sputtering, predict higher fluxes on the dayside at high latitudes (Lillis et al., 2015) and recent MAVEN observations, though limited in coverage, are in agreement (Leblanc et al., 2015) This means that sputtering may preferentially occur at some latitudes and/or local times. Thus, it would be more appropriate to use Δz and H_{40} from those locations in the Rayleigh distillation calculation than the average values. For instance, dayside scale heights are larger (Fig. 3.7) and produce smaller fractionation at the exobase, implying our mean total loss may be an underestimate.

Rayleigh distillation also ignores any process that adds gas to the atmospheric reservoir. However, the presence of volcanic structures and resurfaced regions indicate that outgassing of the interior has occurred since the onset of the geologic record even if it does not today. Sporadic delivery by asteroids and comets has almost certainly played a role as well.

Finally, we have neglected to consider any time dependence of the removal of Ar from an initial reservoir (and the time-dependencies of processes that have been ignored). Has the fractionation

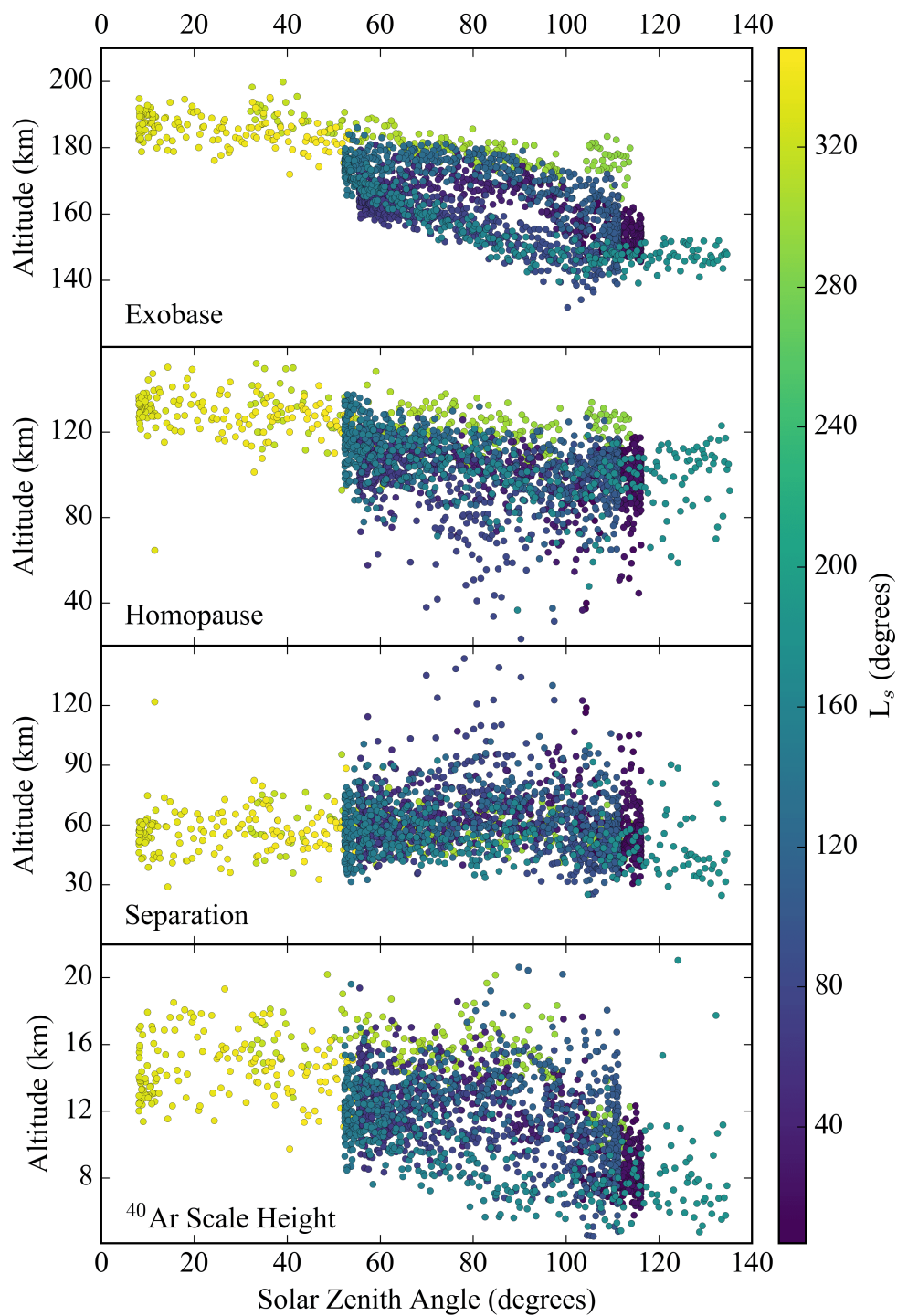


Figure 3.7: Variability of (top) exobase altitudes, (second from top) homopause altitudes, (third) separation distances, and (bottom) scale heights with solar zenith angle.

factor varied through time? If so, the derived values, while instructive for understanding loss in the current epoch, may not represent the fractionation when the most substantial loss occurred. In the next chapter, we improve upon a simple estimate of loss from Rayleigh distillation to gain insight into how major planetary processes altered Ar isotope ratios over time and provide a more accurate determination of the integrated Ar escape.

3.4 Summary and conclusions

- Exobase altitudes derived from Ar and CO₂ densities from Feb 2015 - July 2016 are ~170 km on average and they vary together with homopause altitudes.
- Scale height temperatures between species and ³⁶Ar/³⁸Ar measured during deep dip 4 show diffusive separation above the homopause.
- There is a range of variability of ³⁶Ar/³⁸Ar fractionation at the exobase due to changes in the separation distance between the homopause and exobase and the thermospheric temperature.
- Using Rayleigh distillation, we find that the observed Ar isotope fractionation requires that $63 \pm 5\%$ of ³⁶Ar has been lost to space.
- Rayleigh distillation ignores any processes that have supplied Ar to the atmosphere or removed it at some ratio other than in proportion to the isotopic ratio at the exobase. We explore this further in the following chapter.

Chapter 4

Argon Isotope Evolution Model

4.1 Introduction

There is no doubt that Mars' atmosphere has changed drastically from its initial state 4.5 Gyr ago as a result of several important processes such as volcanic outgassing, interaction with the surface, and escape to space. Isotopic ratios of various atmospheric volatiles are fractionated through these processes, leaving an imprint of the atmosphere's evolution. Measurements of atmospheric H, C, O, N, and Ar (see Table 1.1) show an enrichment in heavy isotopes relative to Earth isotopic ratios (Owen et al., 1977; Bogard et al., 2001; Krasnopolsky et al., 1998; Webster et al., 2013; Atreya et al., 2013). This is striking evidence that loss of Mars' atmosphere to space has occurred (Jakosky, 1991; Jakosky et al., 1994). Lighter isotopes diffusively separate and are preferentially removed either by thermal processes (Jeans escape) in the case of H, or non-thermal processes such as dissociative recombination and collisions via impingement of the solar wind (Chassefière and Leblanc, 2004).

Indeed, measurements of the ratios of ^{36}Ar , ^{38}Ar , and ^{40}Ar in the present-day atmosphere (by Viking and the Mars Science Laboratory, MSL) and of the past atmosphere (through meteorites) are robust indications of significant Ar loss (Jakosky et al., 1994). These observations are displayed in Table 4.1. The value of $^{36}\text{Ar}/^{38}\text{Ar}$ in Earth's atmosphere is nearly equivalent to the ratio in the solar wind, asteroids, and Jupiter's atmosphere; that is, Earth's $^{36}\text{Ar}/^{38}\text{Ar}$ is primordial. Assuming the source of atmospheric argon on both planets was the same (be it volcanic outgassing or asteroids and comets) the lower ratio of $^{36}\text{Ar}/^{38}\text{Ar}$ in the Martian atmosphere can only be explained by loss

Table 4.1: Measurements of the atmospheric Ar isotope ratios and abundances from various sources. The meteorite measurements come from the trapped gas impact melts. Earth’s atmospheric values are shown for reference.

	Ar mixing ratio	$^{36}\text{Ar}/^{38}\text{Ar}$	$^{40}\text{Ar}/^{36}\text{Ar}$	Age
MSL	$0.0193 \pm 0.0003^{\text{a}}$	$4.2 \pm 0.1^{\text{b}}$	$1900 \pm 300^{\text{a}}$	present-day
Viking ^c	0.016	5.5 ± 1.5	3000 ± 500	present-day
Shergottites ^d		4.1 ± 0.1	1800 ± 100	<0.2 Gya
Nakhlites ^d			1615 ± 203	1.33 ± 0.02 Gya
ALH 84001 ^e			626 ± 100	4.16 ± 0.04 Gya
Solar wind ^f		5.501 ± 0.014		present-day
CI Chondrites ^g		5.30 ± 0.05		primitive
Jupiter ^h		5.6 ± 0.25		present-day
Earth ⁱ	0.0093	5.305 ± 0.002	298.56 ± 0.31	present-day

^a Mahaffy et al. (2013); ^b Atreya et al. (2013); ^c Owen et al. (1977);

^d Bogard et al. (2001); ^e Cassata et al. (2010); ^f Pepin et al. (2012), see also Vogel et al. (2011); ^g Pepin (1991); ^h Mahaffy et al. (2000); ⁱ Lee et al. (2006)

to space. The ratio of $^{40}\text{Ar}/^{36}\text{Ar}$ in the Martian atmosphere today also shows an enrichment in the heavy isotope ($^{40}\text{Ar}/^{36}\text{Ar} \sim 6$ times the value in Earth's atmosphere), though interpreting this ratio is slightly more complicated as ^{40}Ar is produced by the decay of ^{40}K in the mantle and crust and is supplied to the atmosphere over time.

Motivated by recent confirmation of the enrichment of heavy isotopes in Mars' atmosphere and ongoing measurements of the upper atmosphere by the Mars Atmospheric and Volatile Evolution (MAVEN) mission, we sought to investigate atmospheric loss by modeling the evolution of Ar isotopic ratios through time. To do this, exchanges of volatiles between the atmosphere and other reservoirs – the mantle, the crust, and impactors – must be considered in addition to escape processes because they have certainly affected the atmospheric ratios as well, whether they have operated throughout Mars' history or only for a brief period. The complexity of the problem is somewhat alleviated for Ar compared to H, C, O, and N because as a noble gas, the available exchange pathways are limited; a model of the other gases would also need to include interactions of the atmosphere with the polar caps and the regolith. Since the time-variability of all the processes mentioned are poorly constrained, each one further amplifies the uncertainty in the model. Thus, by studying Ar we can build an understanding of a few important drivers of atmospheric evolution, how they have affected isotopic ratios through time, and what the present-day ratios imply about total atmospheric loss.

We constructed a box model in which Ar is exchanged between various reservoirs through time, considering several processes. ^{40}Ar is produced by radioactive decay of ^{40}K in the mantle and the crust and is volcanically outgassed along with ^{36}Ar and ^{38}Ar . Once in the atmosphere, all the isotopes are subject to removal through interaction with the solar wind. In addition, impactors during the Late Heavy Bombardment (LHB) and thereafter act as both a source, as gases are supplied to the atmosphere, and a (non-fractionating) sink from impact erosion. We assume a range of time-variable intensities for each of these processes and march from 4.4 Gya to the present.

The remainder of this paper is structured as follows: We first describe the model in Section 4.2, explain how it improves upon past models, detail the initial conditions of the various reservoirs,

and justify the use of the time-dependent rates assumed for each exchange process. Then in Section 4.3 we explain outputs of the model by (a) building an intuition for the various processes by showing how each affects Ar isotope ratios in the absence of any other processes, (b) showing the interplay between various processes as they are combined in the model together, and (c) using present-day atmospheric measurements as model constraints to determine the parameter space consistent with observations. Finally, in Section 4.5 we discuss a few noteworthy consequences of the model.

4.2 Model

In this section, we explain the details of our box model (illustrated in Fig. 4.2) which consists of three main reservoirs in the system through which Ar is exchanged: the mantle, crust, and atmosphere. We describe the mantle reservoir and the processes that affect its Ar inventory – radioactive decay of ^{40}K , volcanic outgassing, and growth rate of the crust. Similarly, we discuss the initial conditions of the crustal reservoir and how ^{40}Ar is released into the atmosphere. This is followed with a justification of the range of escape rates of atmospheric Ar used and an explanation of how we include impact delivery and impact erosion in the model. All initial conditions and rates described in this section are listed in Table 4.2 for reference.

The abundance of Ar in each reservoir, r , evolves according to:

$$\frac{d^{\text{X}}\text{Ar}_r}{dt} = \sum_n [S_n(t) - L_n(t)] \quad (4.1)$$

For each isotopic species of argon – $^{\text{X}}\text{Ar}$ where X can be 36, 38, or 40 – the change in abundance with time of that species in a particular reservoir is equal to the supply rate of argon to that reservoir, S , minus the loss rate from the reservoir, L for each process, n , at time t . This allows for investigation of the evolution of ^{36}Ar , ^{38}Ar , and ^{40}Ar abundances and isotopic ratios in each reservoir. The model progresses forward in time for 4.4 Gyr (gigayears) in steps of 1 Myr. The argon isotopic abundances are calculated at each timestep and the content of each reservoir is updated. Similar approaches have been taken by Pepin (1994), Hutchins and Jakosky (1996) (two-reservoir system),

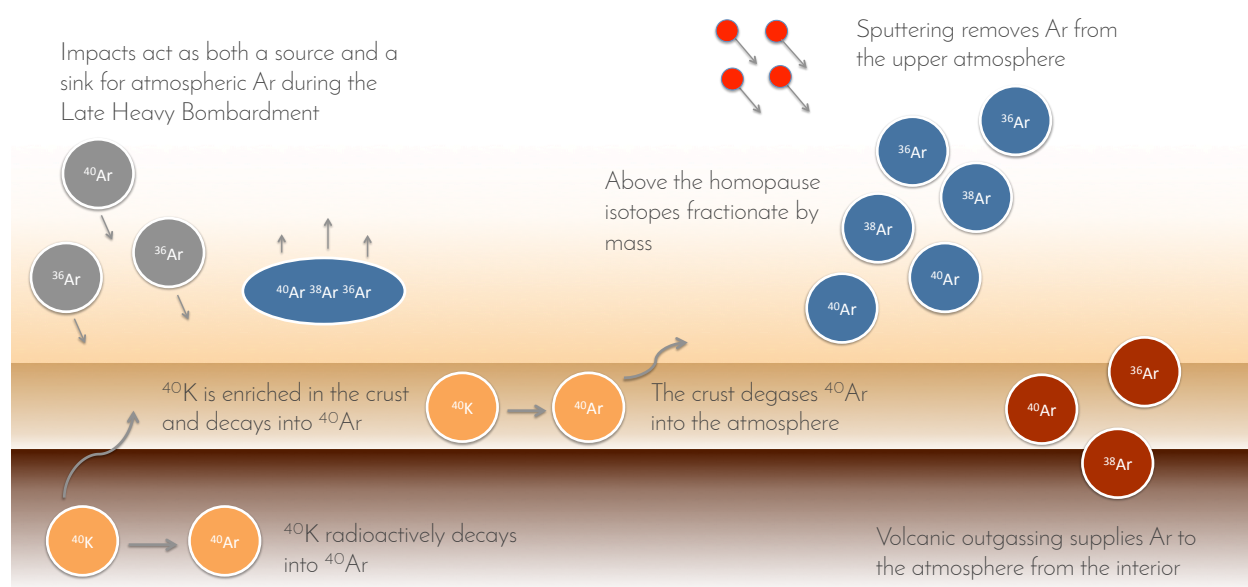


Figure 4.1: A schematic diagram of the reservoirs and exchanges considered in the box model described in detail in the text.

Table 4.2: Initial conditions of reservoirs (4.4 Gya unless noted otherwise) and rates used for the parameters considered.

Parameter	Value, range, or rate used
<i>Mantle</i>	
[⁴⁰ K]	0.4 ppm
[³⁶ Ar], ³⁶ Ar/ ³⁸ Ar, [⁴⁰ Ar]	6.0×10^{-5} ppm, 5.305, 0
Crustal Production Rate	$0.3 - 5 \times$ Morschhauser et al. (2011) & Jakosky and Shock (1998)
Extrusive : Intrusive outgassing	1:8.5
K Crustal Enrichment	$5 \times$
<i>Atmosphere</i>	
³⁶ Ar Abundance	0 mbar 4.4 Gya, 9.3×10^{-5} mbar 4.0 Gya for the sputtering only case (Section 3.1.3)
³⁶ Ar/ ³⁸ Ar	5.305
⁴⁰ Ar Abundance	0 mbar 4.4 Gya, 6.2×10^{-3} mbar 4.0 Gya for the sputtering only case (Section 3.1.3)
CO ₂ Pressure (P_0)	$6 - 10^4$ mbar
CO ₂ Evolution	linearly decreasing or exponentially decreasing to 6 mbar
Sputtering Rate	$1 - 100 \times$ Chassefière and Leblanc (2011), scaled to Ar
<i>Impactors</i>	
⁴⁰ K/K	1×10^{-3}
[³⁶ Ar], ³⁶ Ar/ ³⁸ Ar	1.3×10^{-3} ppm, 5.3
[C]	2% by mass
Delivery and Erosion Model	Heath and Brain (2013)

Cassata et al. (2012) (early $^{40}\text{Ar}/^{36}\text{Ar}$), Leblanc et al. (2012) (^{40}Ar only), and Pujol et al. (2013) (Earth). However, none have considered all three isotopes simultaneously, used broad ranges of escape, outgassing, and CO_2 histories, or included the effects of impact delivery and erosion.

4.2.1 Mantle reservoir and processes

Here, we explain the initial concentrations of Ar and ^{40}K used in the mantle reservoir, the conversion of ^{40}K to ^{40}Ar through radioactive decay, the rate at which radiogenic and non-radiogenic Ar species are transported to the atmosphere, and the rate at which mantle K is supplied to the crust. Given these processes, the changes in abundances of Ar isotopes in the mantle are given by:

$$\frac{d}{dt} {}^{40}\text{Ar}_m = S_{decay} - L_{out} \quad (4.2)$$

for ^{40}Ar and

$$\frac{d}{dt} x_{\text{Ar}_m} = -L_{out} \quad (4.3)$$

for ^{36}Ar and ^{38}Ar . Ar_m is the abundance of Ar in the mantle reservoir at some time, S_{decay} is the rate at which ^{40}Ar is generated from radioactive decay, and L_{out} is the rate at which Ar is lost to the atmosphere through volcanic outgassing.

To determine the initial concentration of ^{40}K in the mantle, we use two methods: (1) we estimate a ^{40}K concentration for the Earth 4.5 Gya and assume Mars would have had a similar value and (2) we assume Mars' present-day bulk $^{40}\text{K}/\text{K}$ is equal to present-day Earth's bulk $^{40}\text{K}/\text{K}$ and determine the amount of ^{40}K that has decayed. The concentration of K in the bulk silicate Earth is 280 ± 60 ppm, which has not changed significantly over 4.5 Gyr, with $^{40}\text{K}/\text{K} = 1.2 \times 10^{-4}$ (Arevalo et al., 2009). If all the ^{40}Ar in Earth's atmosphere (1.6×10^{18} mol (Ozima and Podosek, 2002)) has decayed from ^{40}K (the decay constant for ^{40}K is $\lambda = 5.543 \times 10^{-1} \text{ Gyr}^{-1}$ and the branching ratio for decay into ^{40}Ar is $\beta = 0.1048$) and has been released to the atmosphere over 4.5 Gyr while none has been lost, the initial bulk silicate ^{40}K concentration would have been

$[^{40}\text{K}] = 0.2$ ppm. However, about 50% of Earth’s total ^{40}Ar abundance may reside in the interior (see Marty (2012)) increasing the initial concentration to $[^{40}\text{K}] = 0.4$ ppm and $^{40}\text{K}/\text{K} = 1.4 \times 10^{-3}$. Alternatively, one could estimate Mars’ initial mantle ^{40}K concentration from its present-day bulk or mantle and crust K, 250–315 ppm (Dreibus and Wanke, 1985, 1987; Wanke and Dreibus, 1994), assuming the same ratio of ^{40}K to K as present-day Earth, and calculating the amount of ^{40}K that would have decayed over 4.4 Gyr. This results in $[^{40}\text{K}] = 0.36\text{--}0.45$ ppm, indicating that $[^{40}\text{K}] = 0.4$ ppm is a reasonable choice. We discuss the impact of this value further in Section 4.5.2.

^{40}Ar is produced in the mantle according to:

$$S_{decay} = \lambda^{40}\text{K}_m\beta \quad (4.4)$$

where S_{decay} is the rate of ^{40}Ar added to the mantle.

We assume a negligible amount of ^{40}Ar existed in the mantle as little would have been produced by ^{40}K in such a short time after formation (1.2 Gyr half-life) and any ^{40}Ar in the mantle would have been subject to early catastrophic outgassing. The initial abundances of ^{36}Ar and ^{38}Ar in the mantle at 4.4 Gya are based on present-day concentrations in Earth’s atmosphere, which we assume are the result of efficient outgassing from the interior (Pujol et al., 2013). Thus, as in Hutchins and Jakosky (1996), we use an initial concentration of ^{36}Ar in the Martian mantle equal to 3.45×10^{-11} g/g-planet, which Pepin (1991) estimates for Earth’s atmosphere, with $^{36}\text{Ar}/^{38}\text{Ar} = 5.305$.

4.2.1.1 Outgassing and crustal production

To estimate the amount of Ar released to the atmosphere through volcanic outgassing we assume some volume of mantle per unit time undergoes partial melting and produces crust, the concentration of Ar in this volume is equal to the mantle Ar concentration, and that all of this Ar is released to the atmosphere. Similar to the approach in Leblanc et al. (2012), we calculate the amount of volatiles released to the atmosphere from the mantle using rates of crustal production through time of Morschhauser et al. (2011) and Jakosky and Shock (1998), before and after 3.8

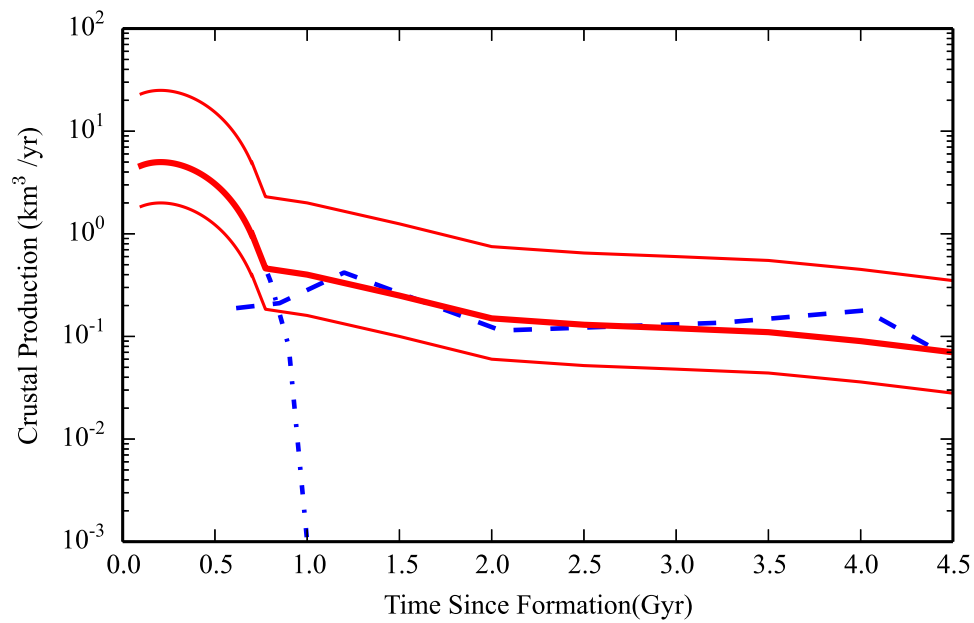


Figure 4.2: Models of crustal production from Morschhauser et al. (2011) (dashed-dotted line), Greeley and Schneid (1991) (dashed line), and a combination of Morschhauser et al. (2011) before 0.7 Gyr after formation and Jakosky and Shock (1998) after 0.7 Gyr used in this work (red solid) for $v_f = 0.3, 1$ (heavy), and 5.

Gya, respectively. The rate from 3.8 Gya on is based on photogeological analyses of Viking images performed by Tanaka et al. (1988) and Greeley and Schneid (1991) of volcanic eruptions through different Martian epochs. For each epoch, Greeley and Schneid (1991) assumed a 1:8.5 ratio of extrusive to intrusive volcanism (similar to that on Earth) in order to infer the total amount of crust produced. However, this method likely underestimated volcanism rates during the Noachian because resurfacing during Mars’ early history has inhibited study of the oldest eruptions. A recent global study of volcanic provinces utilizing high-resolution images from Mars Express suggests that volcanism was widespread and all volcanic provinces had formed prior to 3.6 Gya. Since then, volcanism has been localized (with only a few active regions) while the intensity has decreased (Werner, 2009).

To compensate for the underestimation of Noachian volcanism by geological methods, we base our crustal production and outgassing rates on results from a thermochemical evolution model of the interior (Morschhauser et al. (2011)) for the early crustal production rate (see Grott et al. (2013) for detailed review of the evolution of the mantle and crust). This model predicts high rates until ~ 700 Myr after Mars’ formation followed by a rapid decrease in which volcanism shuts off after 1 Gyr. Since the geological evidence suggests there has been volcanism until very recently, we adopt crustal production rates of the thermochemical evolution model from 4.4–3.8 Gya and stratigraphically derived values from 3.8 Gya–present assuming a ratio of extrusive to intrusive volcanism of 1:8.5 (Fig. 4.2).

In our model, at each time step, a volume of mantle determined by the crustal production rate, F_c , is transported to the crust and the volatiles in that volume are assumed to degas from the magma efficiently, such that 100% of the volatile mass is released into the atmosphere. We also include a term, v_f – the “volcanic factor” – which is simply a multiplicative factor that can account for a different volcanism rate from the models described, a different ratio of intrusive to extrusive volcanism, depletion or enrichment in ^{36}Ar or ^{38}Ar , or other factors. The nominal value used is $v_f = 1$, and (as discussed in Section 4.3) we chose a minimum of $v_f = 0.3$ and a maximum of $v_f = 5.0$. The proportion of argon species removed from the mantle is equal to the proportion

in the mantle at that time. So the amount of Ar released into the atmosphere per unit time from mantle outgassing, L_{out} , is:

$$L_{out} = X_{Ar_m} \frac{F_c}{V_m} v_f \quad (4.5)$$

where V_m is the total mantle volume.

Similarly, a fraction of mantle K is incorporated into the melt and transferred to the crust. K is an incompatible element, meaning it prefers to be concentrated in the melt. So we assume (following Leblanc et al. (2012)) that the volume of crust produced is enriched in K by a factor of 5, though factors as high as 20 are reasonable (Morschhauser et al., 2011). ^{40}Ar is produced in the crust in a higher proportion than the mantle as a result. This is important, as we will discuss later, because we also must consider release of crustal ^{40}Ar to the atmosphere. The rate of change of mantle K abundance, $^{40}\text{K}_m$ is given by:

$$\frac{d}{dt} ^{40}\text{K}_m = -^{40}\text{K}_m \lambda - 5 \times ^{40}\text{K}_m \frac{F_c}{V_m} v_f \quad (4.6)$$

4.2.2 Crustal erosion

Our model contains a crustal reservoir that grows through time as described above. The crust is produced from partial melts of mantle material, so ^{40}K accumulates in the crust and radioactively decays producing ^{40}Ar that can be released to the atmosphere. In the model, nothing is transferred from the atmosphere to the crust and only K is emplaced from the mantle during crustal production, so ^{36}Ar and ^{38}Ar do not interact with the crust whatsoever. Thus, the governing equations are:

$$\frac{d}{dt} ^{40}\text{K}_c = 5 \times ^{40}\text{K}_m \frac{F_c}{V_m} v_f - ^{40}\text{K}_c \lambda \quad (4.7)$$

where $^{40}\text{K}_c$ is the crustal abundance of ^{40}K , and the change in crustal ^{40}Ar is

$$\frac{d}{dt} ^{40}\text{Ar}_c = S_{decay} - L_{cd} \quad (4.8)$$

where the supply of ^{40}Ar from decay is $S_{decay} = {}^{40}\text{K}_c\lambda\beta$ and L_{cd} is the loss from crustal erosion.

The mechanism through which argon and other light noble gases can be released from the crust is not well understood, but has been recognized as an important process for Earth's atmospheric volatile inventory (Torgersen, 1989; Watson et al., 2007). Argon may be released from crustal minerals through diffusion or through chemical alteration facilitated by groundwater. Upon release, such gases are dissolved and transported to the surface by advecting groundwater, where they can enter the atmosphere (Hutchins, 1998). We will show in Section 4.3 that the present-day abundance of ^{40}Ar in the Martian atmosphere cannot be produced from volcanic outgassing alone, but it can be if crustal release is included. Since we do not consider any of the Ar isotopes to be transferred from the mantle to the crust, the only equation describing the amount of supply to the atmosphere from the crust, L_{cd} , at some time is $L_{cd} = {}^{40}\text{Ar}_c\gamma$, such that:

$$\frac{d}{dt} {}^{40}\text{Ar}_c = {}^{40}\text{K}_c\lambda\beta - {}^{40}\text{Ar}_c\gamma \quad (4.9)$$

where ${}^{40}\text{Ar}_c$ is the abundance of ^{40}Ar in the crust and γ is the efficiency of ^{40}Ar degassing. γ is wholly unconstrained because the release mechanism is not well understood, so we consider any value between 0 and 1 to be plausible. This essentially acts as an increased v_f for ^{40}Ar without affecting other isotopes.

4.2.3 Atmospheric reservoir and associated processes

In this section, we will give the initial conditions used in the atmospheric reservoir, show the governing equations of exchange, and explain how loss to space and impact processes are built into the model. The evolution of the atmospheric reservoir for the isotopes is given by:

$$\frac{d}{dt} x_{\text{Ar}_a} = S_{out} - L_{sput} + S_{imp} - L_{imp} \quad (4.10)$$

where the rate of Ar supplied by outgassing to the atmosphere, S_{out} , is equal to $-L_{out}$ from the mantle. L_{sput} is the rate of Ar lost to space through collisions with pickup ions, described in detail

in the following subsection. S_{imp} and L_{imp} are the rates of impact supply and removal, respectively. These are explained further in Section 4.2.3.2. Additionally, for ^{40}Ar , supply of Ar from crustal erosion, S_{cd} (equal to the loss rate from the crust, L_{cd}) must be included.

Hydrodynamic escape of a primary atmosphere around Mars is thought to have been an important process in the first 100 Myr of Mars' history as it can explain the observed Xe abundance and isotopic fractionation (Hunten et al., 1987; Pepin, 1991, 1994). Such models result in significant loss of primordial atmospheric noble gases lighter than Xe. We assume, then, that any ^{36}Ar or ^{38}Ar in the atmosphere prior to 4.4 Gya was lost through hydrodynamic escape and we note that the long (1.28 Gyr) half-life of ^{40}K ensures that very little ^{40}Ar would have been released from the interior during the first 100 Myr (Pepin, 1994), so our initial atmospheric reservoir contains no Ar. If ^{36}Ar and ^{38}Ar abundances remaining after hydrodynamic escape were comparable to the present-day abundances and heavily fractionated, we may overestimate the amount of fractionation that has occurred since 4.0 Gya. We discuss this further in Section 4.5.1.

4.2.3.1 Escape to space via sputtering

In our model, atmospheric sputtering, the removal of exospheric species from collisions with impacting pickup ions, is the process through which Ar atoms can be lost to space. Several estimates of the sputtering rate of CO_2 have been made (despite the lack of useful data) which we utilize to estimate the escape rate of Ar. After describing the basic concept of sputtering and its effect on isotope ratios, we briefly review previous works that have modeled sputtering rates of CO_2 at different times in Martian history, explain how we account for the uncertainties in these models, and show how we scale from CO_2 sputtering rates to Ar sputtering rates.

Thermal and non-thermal processes can remove atmospheric species from the Martian atmosphere. Of the escape mechanisms active throughout Mars' history (see Chassefière et al. (2007) for more detail), sputtering is the most important for escape of Ar. Ionization and escape may also be responsible for some loss and fractionation of Ar (see Chassefière and Leblanc (2004)), but the escape energies of Ar isotopes are greater than particle energies from common photochemical

reactions in the upper atmosphere (Leblanc et al., 2012). This process is not well understood and therefore, outside the scope of this paper. Neutral species are sputtered from the exobase (~ 200 km) via collisions with O^+ ions – O atoms can be ionized by UV photons, electron impacts, or charge exchange in the upper atmosphere and are subsequently picked up in the exosphere by the interplanetary magnetic field. Many of these ions may be lost to space, but due to gyroradii on the order of Mars’ radius, they frequently re-impact the upper atmosphere. Those colliding with sufficient energy can eject neutrals from the exobase (Luhmann et al., 1992; Jakosky et al., 1994; Chassefière et al., 2007). Diffusion acts on shorter timescales than large-scale mixing above the homopause (~ 120 km), allowing the profile of each species to be represented by a different scale height. Since lighter species have larger scale heights, they are preferentially removed from the exobase, which in turn causes isotopes to fractionate from their initial ratio in the lower atmosphere. Sputtering of neutrals is a time-dependent process driven by the solar wind and EUV flux, so evolving solar conditions must be taken into account (Luhmann et al., 1992; Chassefière et al., 2007). To calculate argon sputtering rates, we scaled to estimates of the CO_2 sputtering rates using ratios of the yields, fractionation factors, and relative abundances of Ar species and CO_2 . A description of estimates that have been made for Mars’ CO_2 sputtering history follows.

Fig. 4.3 shows CO_2 sputtering evolutions as calculated by Luhmann et al. (1992), Chassefière et al. (2007), and Chassefière and Leblanc (2011). Because this process depends on the EUV intensity, when calculating escape rates through time most authors have considered three EUV epochs: 1, 3, and $6 \times$ the present-day solar intensity (Zhang et al., 1993). In turn, the EUV epochs are converted to ages through studies of solar type stars (Zahnle and Walker, 1982; Ribas et al., 2005). 3 and $6 \times$ today’s average EUV flux correspond to roughly 2.7 and 3.5 Gya, respectively. At each epoch the rate of precipitating O^+ ions and the interaction of these ions with the upper atmosphere have been modeled to determine the CO_2 yield, the number of CO_2 molecules removed for every colliding ion, and the sputtering rate of CO_2 . Luhmann et al. (1992) presented the first of these calculations, Chassefière et al. (2007) used revised sputtering yields from Leblanc and Johnson (2002), and Chassefière and Leblanc (2011) further revised the CO_2 sputtering rate using

considerably smaller fluxes of re-impacting pickup ions based on a 3D model of the interaction of the solar wind and Mars' exobase by Chaufray et al. (2007).

These estimates of the CO₂ sputtering rates at different EUV fluxes have varied substantially between different models. Currently there is little data to constrain models of atmospheric escape, though measurements by the MAVEN instruments will allow for more accurate calculations of escape rates and their dependence on solar wind conditions. Chassefière et al. (2007) note that since the EUV flux varies over the solar cycle by a factor of 2, the escape rate today depends strongly on how this is averaged. Additionally, the variation over a solar cycle in the past is unknown, compiling more uncertainty. To compensate, we adopt a range of sputtering evolutions between the rates Chassefière and Leblanc (2011) rates and up to 100 times these values using a multiplicative factor, s_f . The lower and upper limits are shown by the red solid lines in Fig. 4.3.

To estimate atmospheric Ar sputtering rates from CO₂ sputtering rates, we follow the scaling of Hutchins and Jakosky (1996) for the loss of Ar, L_{sput} at some time:

$$L_{sput} = CO_{2sput} \frac{Y(^XAr)}{Y(CO_2)} \frac{{}^XAr_{hp}}{CO_{2hp}} R_{X/44} s_f \quad (4.11)$$

CO_{2sput} is the rate of sputtered CO₂, which changes with time as described above. $Y(^XAr)/Y(CO_2)$ is the ratio of the yields per concentration of Ar and CO₂. As in Hutchins and Jakosky (1996) we use yields of 2 and 0.7 for Ar and CO₂ given in Jakosky et al. (1994). These yields likely vary with EUV flux (Leblanc and Johnson, 2002), but we assume their ratio will remain about the same through time. ${}^XAr_{hp}/CO_{2hp}$ is the ratio of Ar to CO₂ at the homopause, which is just the ratio of the concentrations in the atmospheric reservoir as described in Section 4.2.3 – the CO₂ abundance at any point in time is determined by the CO₂ evolution (exponentially or linearly decreasing) from some initial pressure assumed for a particular model run. s_f is the sputtering factor, a multiplicative factor from 1-100 that allows us to explore a wide range of sputtering histories because the true history is unknown. Since sputtering happens above the exobase, diffusive separation above the homopause must be accounted for. The density of some species above the homopause is given by Eq. 3.4 and the fractionation of two species at the exobase has been derived in Eq. 3.8. $R_{X/44}$ is

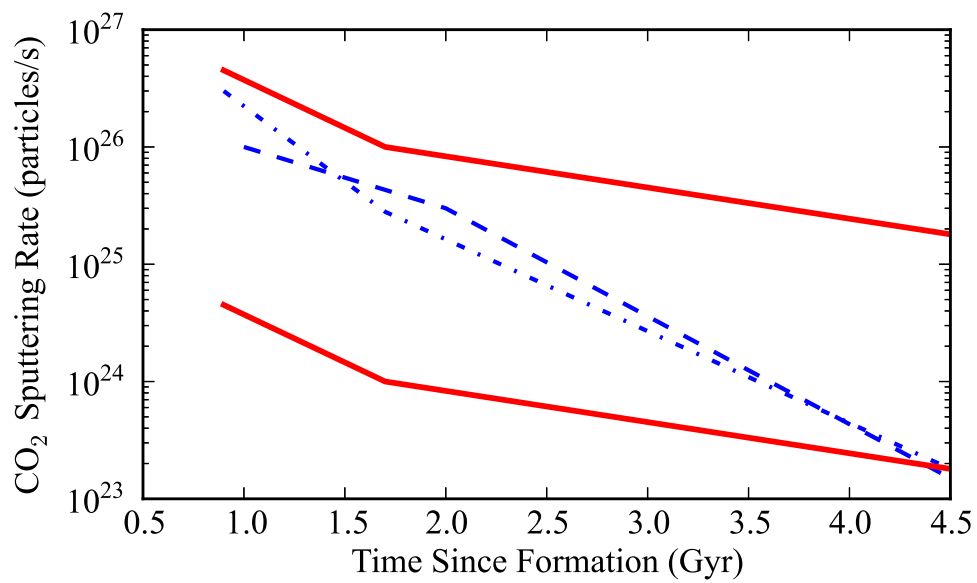


Figure 4.3: Examples of the CO_2 sputtering evolution from Luhmann et al. (1992) (blue dashed), Chassefière et al. (2007) (blue dashed-dotted), Chassefière and Leblanc (2011) (red solid, lower), and $100\times$ Chassefière and Leblanc (2011) (red solid, upper).

used in Eq. 4.11 since the calculation is for some isotope of argon, ^XAr relative to that of CO_2 . Using $\Delta z=80$ km and $T=200$ K, the fractionation factors for ^{36}Ar , ^{38}Ar , and ^{40}Ar with respect to CO_2 are 4.17, 2.92, and 2.04. For comparison with Section 3.3, the equivalent value of $a_{36/38}$ is 1.43. However, we also run a suite of simulations with $\Delta z/T$ values corresponding to the fractionation observed by NGIMS measurements in section 3. We choose 7 values of $a_{36/38}$ between 1–2.7 to test how the real geophysical variability of the upper atmosphere affects the model results.

Though the model begins 4.4 Gyr ago, sputtering does not turn-on in the model until 4.0 Gyr. Evidence for a global magnetic field exists in remnant magnetization of the crust, and according to Lillis et al. (2008) the cessation of this field likely occurred around 4 Gyr ago. A global magnetic field could have reduced or prohibited sputtering of the upper atmosphere. Here, we consider the latter case such that no sputtering occurred while a magnetic field was present, so we use 4 Gyr ago as the sputtering turn-on time. This results in an unhindered accumulation of argon in the atmosphere governed by the outgassing and impact models.

4.2.3.2 Impact delivery and erosion

Impacts can act as both a source and sink for atmospheric Ar because some volatiles contained within an impactor are released, while some of the target atmosphere escapes. There have been several studies in recent years that have investigated the relative importance of erosion and delivery of volatiles due to impacts from asteroids and comets. Previous calculations have suggested that erosion may have removed a significant fraction of Mars' early atmosphere (Melosh and Vickery, 1989), though these effects were unlikely to contribute substantially to atmospheric loss since the Noachian (Brain and Jakosky, 1998; Pham et al., 2009). And the effects of erosion have likely been overestimated in the past, as shown by recent hydrocode simulations (Shuvalov and Artemieva, 2002; Shuvalov, 2009). (For a review of impact erosion studies and proposed mechanisms see de Niem et al. (2012).) Additionally, the mass of volatiles delivered to an atmosphere during an impact can exceed the mass removed (Svettsov, 2000; de Niem et al., 2012). Here, we consider the effects of impacts on Martian atmospheric argon since the onset of the geologic record and the effects during

the LHB.

We estimated the abundance of Ar delivered to the atmosphere since the LHB from the crater database compiled by Robbins and Hynek (2012). First, using the crater densities (diameter, $D > 3$ km) for Amazonian, Hesperian, and Noachian units from Table 5 of Tanaka et al. (2014), we extrapolated across the surface of the planet to determine the total number of craters with $D > 3$ km formed during each epoch. Then, from the size-frequency distribution for all craters with $D > 1$ km from Robbins and Hynek (2012) and assuming the same distribution in each epoch, we converted the total number of craters with $D > 3$ km to a distribution of craters. For each crater size, we estimated a projectile diameter according to Stewart and Valiant (2006) and found a mass for each projectile assuming a density of 2.8 g/cm^3 . Considering the concentration of ^{36}Ar to be 1.3×10^{-9} g/g (Zahnle, 1993) in asteroids and summing over each epoch (assuming all Ar is released into the atmosphere), we calculated that only about 1% of the present-day ^{36}Ar could have been delivered during the Amazonian and about 2.5% during the Hesperian if all of the Ar from each impactor was retained in the atmosphere. Spread over 3.7 Gyr, this mass of Ar is negligible. Similarly, the total atmospheric loss due to impact erosion is thought to have been small during this time – using a tangent plane model, Pham et al. (2009) found that over a range of erosion efficiencies essentially no loss occurs over the last 3.5 Gyr (though it could have been important earlier). Therefore, we chose to ignore post-LHB impacts as an additional source or sink of atmospheric Ar in our investigation.

Performing the same calculation as above for Ar delivered during the Noachian, we found that impactors could have supplied about 7% of the present-day ^{36}Ar . This is small enough to be indistinguishable from slightly varying v_f values within the chosen range, but may not be reflective of the impactor flux at Mars if a late heavy bombardment occurred. de Niem et al. (2012) model atmospheric changes from the LHB for Earth and Mars and find changes of several bar, with delivery being the stronger effect. To test whether or not such a cataclysm could be an important source or sink of atmospheric Ar, we turn to a more sophisticated erosion and delivery model (Heath and Brain, 2013) than our simple calculation. Based on de Niem et al. (2012), this model calculates atmospheric losses from the escape of part of a vapor plume due to an impactor reaching

the surface after traveling through an atmosphere (Svetsov, 2000). de Niem et al. (2012) compared various other atmospheric erosion models (Svetsov, 2007; Genda and Abe, 2003; Shuvalov, 2009) and illustrated sufficient justification for the (Svetsov, 2000) analytic model. Atmospheric gains in the Heath and Brain (2013) model are calculated from impactor retention models by Zahnle (1990) and Svetsov (2007). The fraction of the impactor that is lost after colliding with the planet depends on its size and (for impactors with sizes below some threshold) properties of the atmosphere. Below that limit, the fraction lost is proportional to the amount of atmosphere lost. The amount of volatiles added to the atmosphere from the impactor equals the mass of the impactor retained after impact multiplied by the fraction of the impactor that is composed of volatiles. The available reservoir of volatiles contained in an impactor is a difficult value to determine – the Heath and Brain (2013) model uses the same volatile fraction, 2%, as de Niem et al. (2012), which is based on the results of a study of carbonaceous chondrite meteorites containing 1-5% C (2% is typical for C-type asteroids) (Grady and Wright, 2003).

Now, to determine the effects of these processes on the total Ar inventory we examined results of the model given different target atmospheric pressures over a range of impacting masses, scaled the results, and converted the volatile gains and losses to changes in Ar isotopic abundances. Since our model begins with an initial atmospheric pressure between 7 mbar and 10 bar, we chose to run the simulations with target atmospheres of 0.001, 0.01, 0.1, 0.5, 1.0, 5.0, and 10.0 bar. Additionally, 25 asteroid ensembles were generated with sizes from main-belt-asteroid size-frequency distributions and velocities from outputs of Nice model simulations. We held the total impacting mass between $\sim 2\text{--}5 \times 10^{20}$ kg (Gomes et al., 2005; Gråe Jørgensen et al., 2009; Martin et al., 2006; de Niem et al., 2012). Each of the impacting asteroid ensembles was simulated at each target pressure. The range of the resulting losses and gains of all volatiles (Caldwell and Brain, personal communication, 2014) are displayed in Fig. 4.4. The total volatile gain from impacts ($\sim 1\text{--}2.5$ bar) is independent of the target pressure at the onset of the LHB. Also, atmospheric gains are much larger than losses (< 500 mbar) for target atmospheres up to a few bar.

Erosion does not preferentially remove any atmospheric species, so the loss of each isotope

from the atmosphere (L_{imp}) is simply proportional to the concentration of a given Ar isotope in the atmosphere, where the total amount of atmosphere removed due to impactors is determined by Fig. 4.4. For an initial atmospheric pressure of 100 mbar, over half is lost through the LHB. This blowoff process is non-fractionating, so although the Ar abundances will be diminished, the ratio of $^{36}\text{Ar}/^{38}\text{Ar}$ will not be affected, only changing due to sputtering. For the supply term in Eq. 4.10, we assume the Ar concentration of asteroids is 1.3×10^{-9} g/g with an isotopic ratio of $^{36}\text{Ar}/^{38}\text{Ar} = 5.3$ (Zahnle, 1993). For ^{40}Ar , we assume ^{40}K has decayed in the asteroids since 4.56 Gyr from an initial K content in the impactors of 550 ppm McDonough and Sun (1995) as in Cassata et al. (2012) and we chose an initial $^{40}\text{K}/\text{K}$ ratio of 10^{-3} . For simplicity, we assume the atmospheric changes from gains and losses happens at a constant rate from 4.1–3.8 Gyr ago. So, $0.5\text{--}1.3 \times 10^{-4}$ mbar of ^{36}Ar , $0.94\text{--}2.5 \times 10^{-5}$ mbar of ^{38}Ar , and 6.3×10^{-4} mbar of ^{40}Ar are added during this time. The amount of ^{36}Ar added during the LHB is 1–2 times the present-day abundance. Thus, as will be discussed in Section 4.3.3.3, we run simulations over the full parameter space of outgassing and sputtering with and without the effects of impact delivery and erosion during the LHB.

As discussed in Section 4.2.3, we do not track CO_2 , but allow it to decrease linearly or exponentially. So although the supply and removal from impacts would certainly have affected CO_2 abundances, we ignore the spike in atmospheric pressure that may have resulted. However, by choosing such a wide range of initial pressures, the range of resulting pressures after the LHB effects (Fig. 4.4) are sampled. This allows us to examine the possible change in Ar isotopic concentrations without imposing strict constraints on the evolution of CO_2 .

4.3 Results

The results of our model will be presented in three subsections. The first will show the effect each process has on atmospheric Ar abundances and isotope ratios in the absence of any other processes. Then, we will combine the processes one-by-one and examine the effects as certain parameters are varied. Finally, we use the observations from the Sample Analysis at Mars (SAM) instrument onboard MSL (presented in Table 4.1) as constraints and evaluate the parameter space

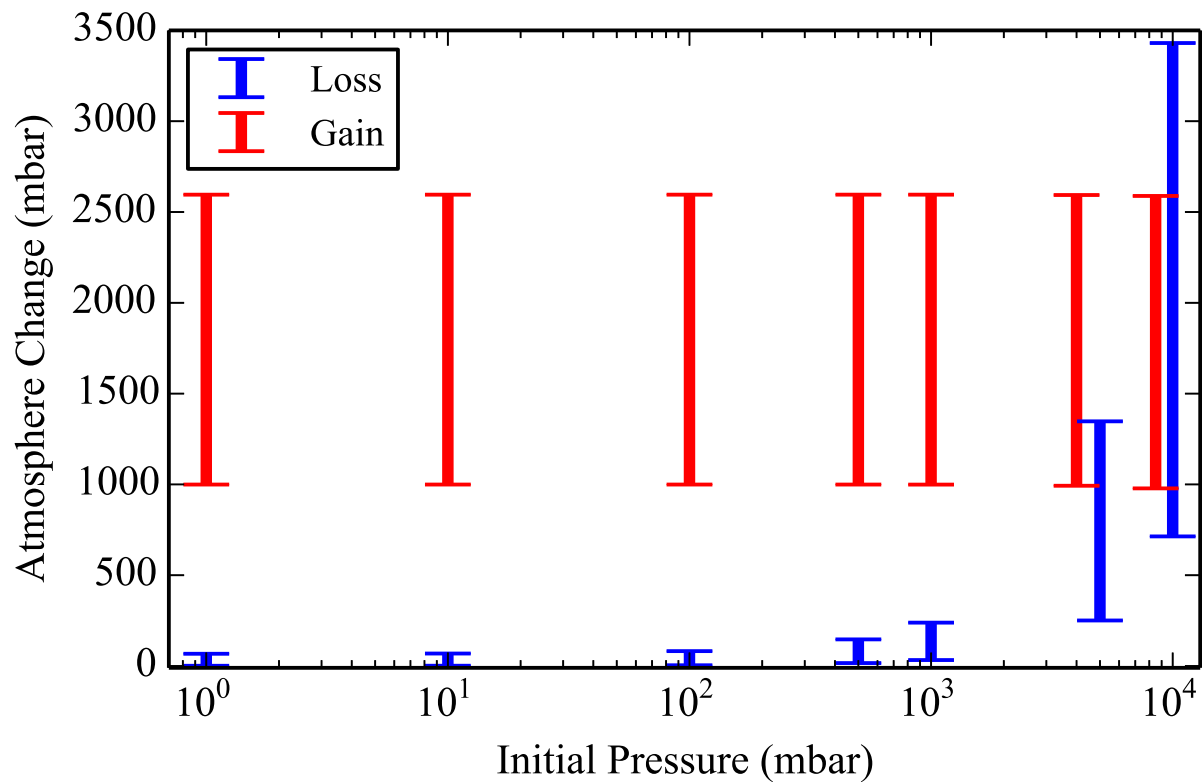


Figure 4.4: Range of atmospheric gains and losses on Mars as a function of initial atmospheric pressure from model simulations (Caldwell and Brain, personal communication, 2014) for 25 impacting ensembles at 7 initial pressures as described in text. Red shows the range of gains and blue the losses for the 25 ensembles at each initial pressure. Gains at 5 and 10 bar slightly offset.

in which the present-day isotopic ratios can be reproduced.

4.3.1 Comparing individual processes

4.3.1.1 Volcanic outgassing

The range of volcanic outgassing rates is shown in Fig. 4.2 and discussed in 4.2.1.1. The changes in each of the atmospheric ^{36}Ar abundance, $^{36}\text{Ar}/^{38}\text{Ar}$ ratio, and $^{40}\text{Ar}/^{36}\text{Ar}$ ratio are shown in Fig. 4.5 as v_f is varied between 0.2 and 5.0. Most of atmospheric ^{36}Ar is delivered in the first half billion years before the outgassing rate decreases significantly to a low, nearly constant value over the past 3.5 Gyr. If no loss processes are considered, three times the present-day ^{36}Ar abundance is outgassed into the atmosphere for $v_f = 1.0$ and $^{36}\text{Ar}/^{38}\text{Ar}$ remains constant for any v_f . Less than 10% of the observed ^{40}Ar is supplied to the atmosphere for $v_f = 0.4$ and only 86% for $v_f = 5.0$, so as seen in Fig. 4.5, the $^{40}\text{Ar}/^{36}\text{Ar}$ remains far below the observed value.

4.3.1.2 Crustal degassing

Only ^{40}Ar is released through crustal erosion, so ^{36}Ar and ^{38}Ar abundances remain unaffected. In the second column of Fig. 4.5 we show crustal degassing rates equivalent to 0–100% release of crustal ^{40}Ar (with $v_f = 1$), apparent only in the bottom plot. Again, no fractionation occurs for $^{36}\text{Ar}/^{38}\text{Ar}$. The $^{40}\text{Ar}/^{36}\text{Ar}$ ratio increases with time significantly in comparison to Fig. 4.5. Generally, the increase in $^{40}\text{Ar}/^{36}\text{Ar}$ is more rapid in the first billion years as crustal production rates are very high, so even though more ^{40}Ar builds up in the crust as ^{40}K decays with no delay in the release, the evolution of atmospheric ^{40}Ar will mimic that of crustal production, though multiplied due to the factor of 5 enhancement of K into the crust.

4.3.1.3 Sputtering factor, s_f

The rightmost column of Fig. 4.5 shows how sputtering changes the evolution of Ar in a very simple case. Here, we start with atmospheric argon isotopic abundances at 0.5 Gyr after formation equal to what is supplied to the atmosphere at that time by outgassing with $v_f = 1$. The

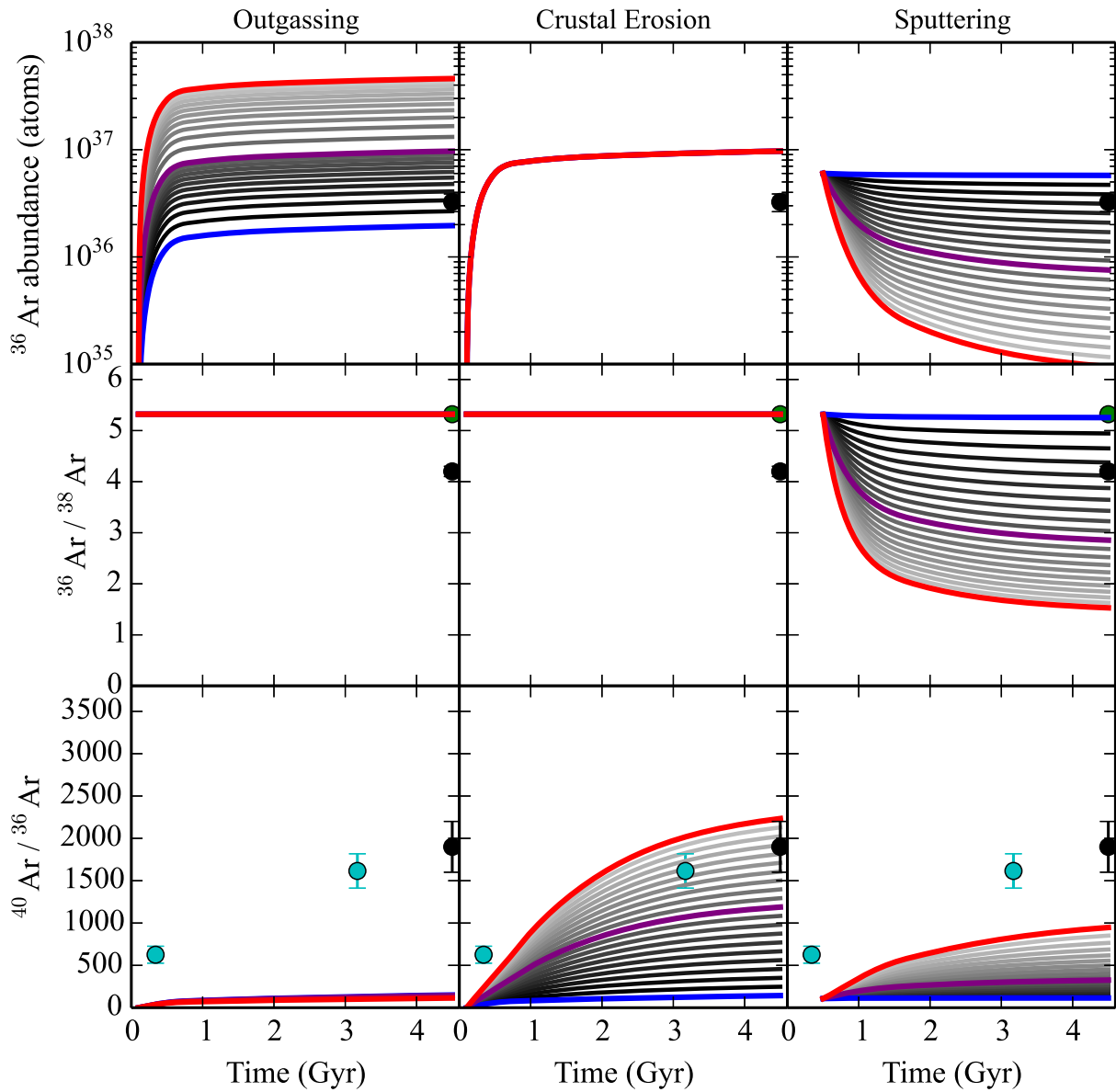


Figure 4.5: Evolution of atmospheric ^{36}Ar (top), $^{36}\text{Ar}/^{38}\text{Ar}$ (middle), and $^{40}\text{Ar}/^{36}\text{Ar}$ (bottom) for 3 cases. Left - considering only volcanic outgassing v_f is varied between 0.2 (blue), 1.0 (purple), and 5.0 (red). Middle - here, crustal degassing is varied between 0% (blue), 50% (purple) and 100% (red) with $v_f=1$. Right - for a constant 1 bar atmosphere, only sputtering operates with s_f of 0 (blue), 50 (purple) and 100 (red). Measurements from SAM (black circles), meteorites (cyan), and Earth's atmosphere (green) are shown as well.

atmospheric pressure is held at a constant 1 bar. For the case of $s_f = 1$ (blue line), very little Ar is sputtered – the ^{36}Ar abundance, $^{36}\text{Ar}/^{38}\text{Ar}$ ratio, and $^{40}\text{Ar}/^{36}\text{Ar}$ ratio remain constant – but as the sputtering factor is increased, Ar is increasingly removed. For $s_f = 100$, the ^{36}Ar abundance drops by nearly two orders of magnitude. ^{38}Ar is removed as well, but less efficiently, such that the $^{36}\text{Ar}/^{38}\text{Ar}$ ratio drops from 5.3 to below 2. Though no ^{40}Ar is released from the crust, the final $^{40}\text{Ar}/^{36}\text{Ar}$ ratios have increased compared to the left column due solely to preferential escape of ^{36}Ar . This implies that to match observations, both will likely have to be included. These fractionation effects will be enhanced if smaller atmospheric pressures are considered – increasing the ratio of Ar/ CO_2 at the homopause enables more efficient sputtering of Ar. We discuss this in the following sections.

4.3.1.4 CO_2 history

Though Fig. 4.5 is useful to gain an intuition as to how sputtering affects the Ar isotopic evolution, a constant 1 bar CO_2 atmosphere is a bad approximation for the pressure history, if only because the atmosphere today is much thinner. Instead, we let the CO_2 pressure decrease either linearly or exponentially from some initial value. The left two columns of Fig. 4.6 use the same conditions described above except that the 1 bar of CO_2 at 0.5 Gyr decreases to 6 mbar by 4.5 Gyr. For the $s_f = 1$ cases (blue lines), very little sputtering occurs just as with constant pressure. But it is clear that for a given value of s_f both the linearly and exponentially decreasing pressures result in more overall Ar loss – lower ^{36}Ar abundances, lower $^{36}\text{Ar}/^{38}\text{Ar}$ ratios, and higher $^{40}\text{Ar}/^{36}\text{Ar}$ ratios. There are also some obvious differences between the linear and exponential cases. Once CO_2 begins to decrease after 0.5 Gyr, sputtering (and thus, fractionation) is more efficient in the exponential case because the CO_2 abundance is always lower. This is amplified early on because the CO_2 sputtering history is highest in the first 1.5 Gyr. For $s_f = 100$, we see in Fig. 4.6 that the ^{36}Ar abundance drops by two orders of magnitude in less than a billion years after sputtering begins. Virtually all the ^{36}Ar is removed, driving $^{36}\text{Ar}/^{38}\text{Ar}$ to 0 and $^{40}\text{Ar}/^{36}\text{Ar}$ to very high values.

4.3.1.5 Initial pressure, P_0

Starting again with the same Ar abundances at 0.5 Gyr, we now hold the sputtering factor constant ($s_f = 10$) and examine the dependence of sputtering on initial pressures (Fig. 4.6, right two columns), whereas above we had used an initial pressure of 1 bar. The pressure still declines either linearly or exponentially to 6 mbar today as in the previous section. Initial pressures less than about 100 mbar produce Ar evolutions in which nearly all the Ar is lost within a billion years of the turn-on time, though this varies with s_f . On the other hand, P_0 above a bar can prohibit Ar from being sputtered. In the linearly decreasing pressure case this is true at all times, but for the exponential case the pressure is reduced to low pressures earlier, so even for $P_0 = 10$ bar a significant amount of Ar is lost and $^{36}\text{Ar}/^{38}\text{Ar}$ is heavily fractionated during the last 1 Gyr. High values of P_0 keep sputtering rates at the turn-on time low and low values of P_0 allow huge amounts of Ar to be lost as soon as sputtering begins.

Though we only show the variation associated with different pressures for $s_f = 10$, it is clear that high values of s_f , combined with small initial pressures, will lead to extreme amounts of Ar loss over 4.5 Gyr. Conversely, the effects of high s_f values can be mitigated with large initial pressures. We will investigate this further below.

4.3.2 Combining processes

Now that the general effect of each individual process has been shown, we can combine processes to see how they interact and which processes dominate at different times as the various parameters are changed. First we examine volcanic outgassing and sputtering together. See the first two columns of Fig. 4.7 for examples with linearly and exponentially decreasing pressures, respectively, where outgassing operates over all of Mars history and s_f is varied between 1–100. These figures illustrate a few apparent differences from the individual cases.

Though the efficiency of Ar sputtering at the turn-on time is still very strong for high s_f values, much less ^{36}Ar is immediately lost (compare with the plots of Fig. 4.6) because outgassing is

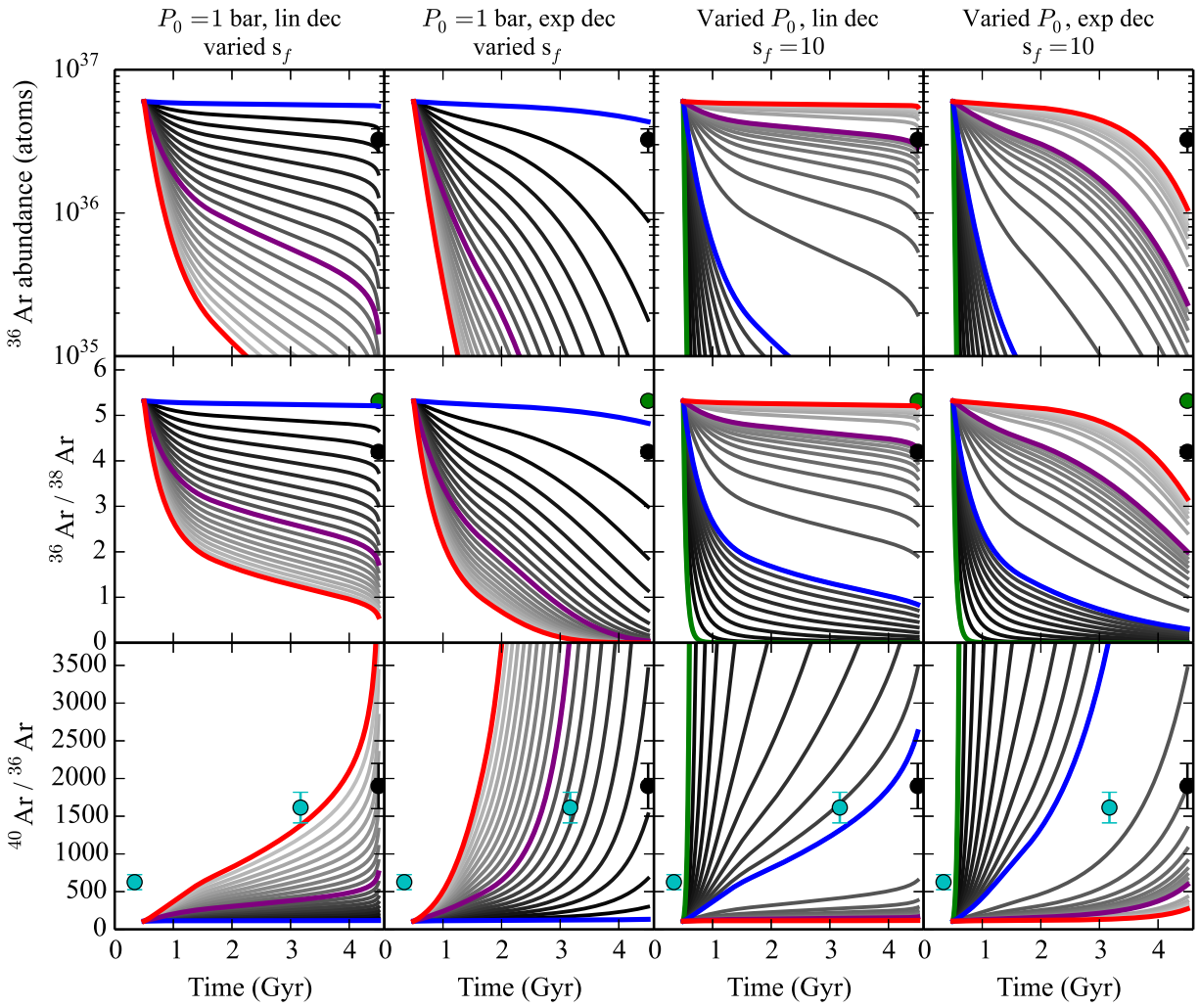


Figure 4.6: Evolution of atmospheric ^{36}Ar (top), $^{36}\text{Ar}/^{38}\text{Ar}$ (middle), and $^{40}\text{Ar}/^{36}\text{Ar}$ (bottom) when only sputtering is considered. Columns 1 and 2 show a range of s_f - 0 (blue), 50 (purple) and 100 (red) - for an initial pressure of 1 bar decaying to 6 mbar linearly and exponentially, respectively. The evolutions in the rightmost columns all have $s_f = 10$, but the initial pressure ranges from 10mbar (green) to 10 bar (red) decreasing linearly (column 3) and exponentially (column 4).

constantly replenishing atmospheric Ar, even if at lower rates than during the first billion years. In fact, in the linear case at high s_f outgassing and sputtering are nearly balanced such that the ^{36}Ar abundance decreases at a relatively low rate from about 2–3.5 Gyr. However, after 4.0 Gyr, runs with high s_f values show a sharp increase in sputtering, as in Fig. 4.6, as the pressure becomes drops below 100 mbar. Sputtering always dominates outgassing for high s_f values and an exponentially decreasing atmosphere, though the replenishment from outgassing significantly decreases the rate at which Ar is lost.

In the second column of Fig. 4.7 we see that the $^{36}\text{Ar}/^{38}\text{Ar}$ ratio actually begins to increase sometime after 1 Gyr. This is due to the extremely low Ar abundances generated in these runs along with continual replenishment from outgassing. The mass of Ar being added to the atmosphere is comparable to the mass of Ar in the atmosphere at these times, and the ratio of outgassed Ar ($^{36}\text{Ar}/^{38}\text{Ar} = 5.3$) is much higher than the heavily fractionated atmosphere. This leads to an increase in $^{36}\text{Ar}/^{38}\text{Ar}$ even as Ar continues to leak into space.

The evolution of the ^{36}Ar abundance and $^{36}\text{Ar}/^{38}\text{Ar}$ ratio also varies greatly with the initial pressure and subsequent evolution (Fig. 4.7, columns 3 and 4). In all cases once sputtering begins, the evolutions diverge – argon sputtering is immediately efficient for cases with low atmospheric pressures (100 mbar), but is inefficient for high pressures (5 bar). When $s_f = 1$ (solid lines), the Ar isotopic evolutions are very similar regardless of pressure. In the decreasing 100 mbar examples (both pressure history cases) with high s_f , the abundance of ^{36}Ar is reduced by a factor of ten within a few 100 Myr, and over 4.0 Gyr 99% of outgassed argon escapes to space. When $P_0 = 5$ bar, essentially no sputtering occurs if the pressure decreases linearly, but 99% if it decreases exponentially. The same behaviors were seen in Fig. 4.6. What differs are the $^{36}\text{Ar}/^{38}\text{Ar}$ and $^{40}\text{Ar}/^{36}\text{Ar}$ evolutions. Here, because of outgassing, $^{36}\text{Ar}/^{38}\text{Ar}$ does not decrease continuously over 4.0 Gyr; $^{36}\text{Ar}/^{38}\text{Ar}$ is often balanced or decreases very slowly. Similarly, the release of ^{36}Ar from outgassing prevents the $^{40}\text{Ar}/^{36}\text{Ar}$ ratio from rapidly increasing at the sputtering turn-on time - the ratio still increases as ^{36}Ar is sputtered, but the effect is heavily diluted.

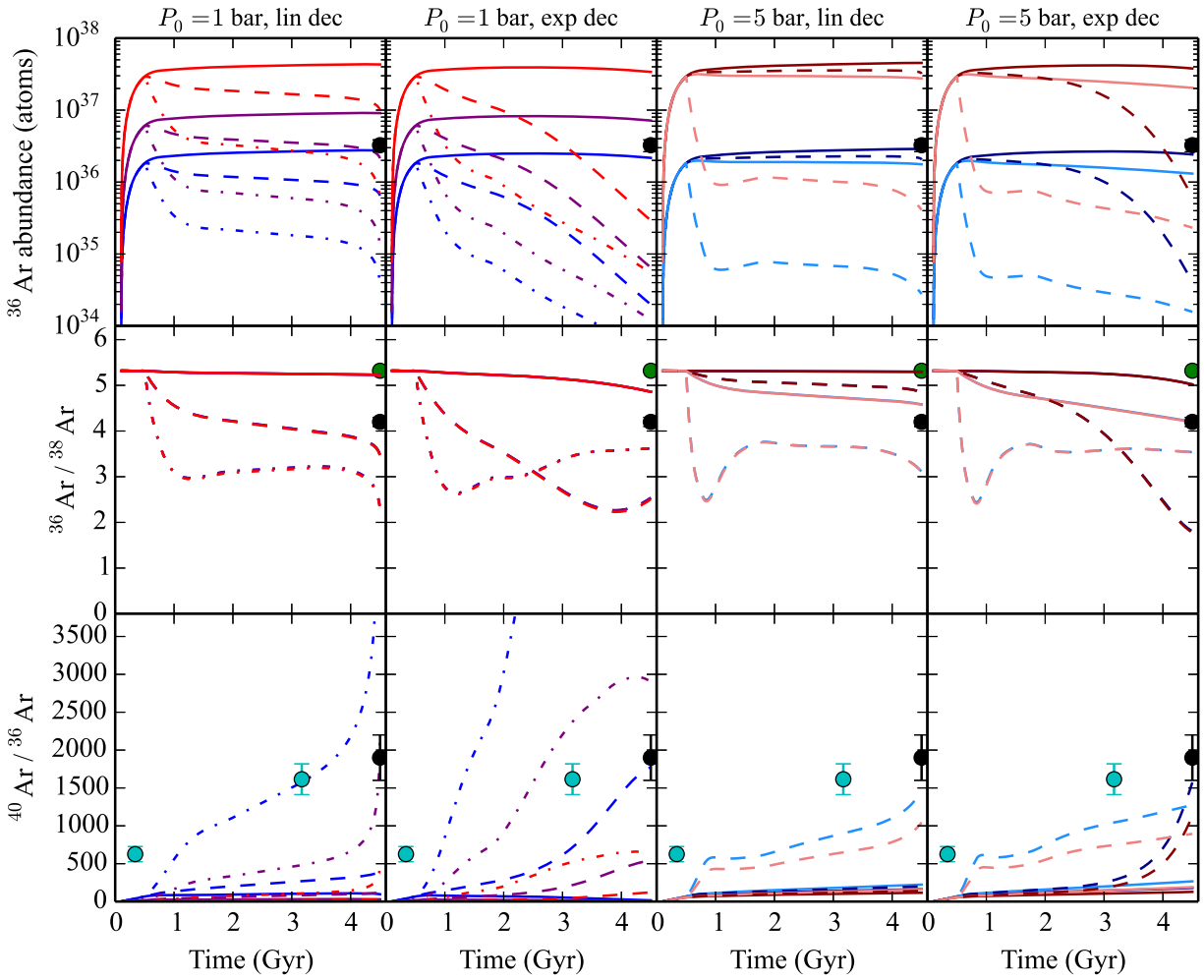


Figure 4.7: Ar evolution for a variety of cases. $v_f = 0.3$ (blue), 1 (purple), or 5 (red) and $s_f = 1$ (solid), 25 (dashed), or 100 (dashed-dotted). In the first 2 columns $P_0 = 1$ bar and in the last 2 $P_0 = 5$ bar (dark) or 100 mbar (light).

4.3.3 Constraining the parameter space

4.3.3.1 ^{36}Ar and ^{38}Ar

Now that we have shown how each individual process and combinations of processes effect the evolution of Ar, next we determine the parameter space that generates present-day values (Table 3). To accomplish this we compare simulation results of Ar isotopic abundances after 4.4 Gyr of evolution to measurements made by SAM. First, we eliminated any runs in which the present-day ^{36}Ar abundance is not reproduced within 2σ . For a CO_2 abundance linearly decreasing with time with some initial pressure, the present-day ^{36}Ar can be reproduced for $0.4 \leq v_f \leq 5.0$ and the full range of s_f . For an exponentially decreasing pressure this is the case again for $0.4 \leq v_f \leq 5.0$, but only for $s_f < 20$. In fact in those simulations, for $v_f < 1.2$, successful runs are only reproduced for $s_f < 9$. A high s_f compounds the effects discussed above for an exponentially decreasing pressure, substantially limiting the parameter space that reproduces present-day values. The range of initial pressures for which the observations can be matched varies significantly with v_f and s_f . For a normal case, with v_f and $s_f = 1$, the present-day ^{36}Ar is matched for initial CO_2 surface pressures of 24–54 mbar for a linearly decreasing pressure and 30–92 mbar for an exponentially decreasing pressure.

We further narrow the parameter space by comparing model results of $^{36}\text{Ar}/^{38}\text{Ar}$ to the observed atmospheric value of 4.2 (within 2σ). A range of $^{36}\text{Ar}/^{38}\text{Ar}$ exists at any v_f and s_f because the ^{36}Ar abundance is reproduced for several initial pressures. The present-day values of $^{36}\text{Ar}/^{38}\text{Ar}$ obtained from those simulations successful in reproducing the ^{36}Ar abundance for a few s_f are shown in Fig. 4.8. A general trend is seen in this figure – that $^{36}\text{Ar}/^{38}\text{Ar}$ decreases with v_f for a given s_f . At first, this may seem counter-intuitive; if the amount of outgassing is increased and more ^{36}Ar and ^{38}Ar are introduced into the atmosphere, further fractionation should be impeded. But since we are specifically examining those runs where ^{36}Ar is reproduced successfully more total outgassed argon means more argon must have been sputtered to match present-day ^{36}Ar . More sputtering always leads to higher fractionation because sputtering is more efficient for ^{36}Ar . So, for successful runs reproducing ^{36}Ar abundance, a higher v_f results in a lower value of $^{36}\text{Ar}/^{38}\text{Ar}$ for a

Table 4.3: Range of parameters explored and constrained by present-day measurements. First the parameters are constrained by the ^{36}Ar abundance, then $^{36}\text{Ar}/^{38}\text{Ar}$, and finally by $^{40}\text{Ar}/^{36}\text{Ar}$.

Parameter	Initial Range	^{36}Ar	$^{36}\text{Ar}/^{38}\text{Ar}$	$^{40}\text{Ar}/^{36}\text{Ar}$
Without Impacts, Linearly Decreasing Pressure (Exponentially Decreasing Pressure)				
v_f	0.4–5.0	0.4–5.0 (0.4–5.0)	0.5–1.1 (0.5–1.1)	
s_f	1–100	1–100 (1–20)	1–100 (1–5)	
P_0 (bar)	0.006–10	0.006–10 (0.006–10)	0.044–10 (0.068–10)	
γ	0–1			0.31–0.65 (0.32–0.67)
With Impacts, Linearly Decreasing Pressure (Exponentially Decreasing Pressure)				
v_f	0.4–5.0	0.4–5.0 (0.4–5.0)	0.4–0.6 (0.4–0.6)	
s_f	1–100	1–100 (1–20)	1–100 (1–5)	
P_0 (bar)	0.006–10	0.006–10 (0.006–10)	0.046–10 (0.074–10)	
γ	0–1			0.55–0.67 (0.66–0.92)

given s_f .

It is clear from Fig. 4.8 that the present-day ^{36}Ar and ^{38}Ar abundances are generated for only a small subset of v_f and s_f for both the linearly and exponentially decreasing pressure cases. For $v_f > 1.1$, excessive fractionation prohibits $^{36}\text{Ar}/^{38}\text{Ar} > 4.0$ for those initial pressures that could also reproduce the ^{36}Ar abundance. Ultimately, the parameter space for which both present-day abundances agree with observations is larger for a linearly decreasing pressure (larger s_f range), though for both pressure histories if $v_f > 1.1$ there is no combination of v_f , s_f , and P_0 which can reproduce observations.

For the lower limit of v_f (0.5), $3.6\text{--}4.4 \times 10^{-5}$ mbar of ^{36}Ar (48–58% of the total ^{36}Ar outgassed into the atmosphere), is lost over 4.0 Gyr. For the upper limit ($v_f = 1.1$), 1.0×10^{-4} mbar of ^{36}Ar (61–63%) is lost. These results are independent of the pressure history, though the combinations of s_f and P_0 that reproduce the present-day values vary significantly.

4.3.3.2 ^{40}Ar

^{40}Ar is the dominant isotope of argon in the atmosphere, but we have not used it up to this point to constrain the parameter space further because the present-day ^{40}Ar cannot be reproduced considering just volcanic outgassing and escape to space. We stated in the beginning of this section that even with $v_f = 5$, only 86% of the total atmospheric argon content is produced. However, since crustal degassing can add ^{40}Ar to the atmosphere, when it is included in the model today's argon mixing ratio as well as the observed isotopic ratios can be replicated. We determined the range of crustal degassing that must have occurred for those scenarios which have reproduced ^{36}Ar and ^{38}Ar abundances to also reproduce the ^{40}Ar abundance and the $^{40}\text{Ar}/^{36}\text{Ar}$ ratio. Again, we consider those matching the SAM measurements (Table 4.1) as successful runs, though meteoritic evidence provide $^{40}\text{Ar}/^{36}\text{Ar}$ ratios from much earlier epochs.

Since the upper limit for the set of parameters that reproduce ^{36}Ar and ^{38}Ar is $v_f = 1.1$, without crustal degassing only 25% of present-day ^{40}Ar is supplied to the atmosphere over 4.4 Gyr. Less remains when escape is considered, though the extent to which ^{40}Ar is sputtered from

the atmosphere is considerably less than ^{36}Ar . Thus, the most important factor for reproducing the present-day ^{40}Ar abundance is crustal degassing. For those simulations in which ^{36}Ar and ^{38}Ar are matched, at least 31% of ^{40}Ar generated in the crust to the atmosphere is required to reproduce ^{40}Ar as well. This lower limit of crustal release occurs for the upper limit of v_f , while at $v_f = 0.5$, up to 67% of the crustal ^{40}Ar must be degassed into the atmosphere. Thus, given the parameters sufficient to reproduce ^{36}Ar and ^{38}Ar abundances, the present-day ^{40}Ar abundance can be reproduced as well if 31–67% of the ^{40}Ar formed by the decay of ^{40}K in the K-enriched crust must be supplied to the atmosphere over 4.4 Gyr. Over the range of $0.5 \leq v_f \leq 1.1$, $2.2\text{--}5.9 \times 10^{-2}$ mbar (18–37% of the total ^{40}Ar supplied to the atmosphere) must escape to space.

4.3.3.3 Including impacts

Next, we included impact delivery and erosion in the model as described in Section 4.2.3.2 with the other processes. We follow the same procedure as above and the results are displayed in Table 3; first, we find the parameters consistent with the present-day ^{36}Ar abundance, then the ^{38}Ar abundance, and finally the ^{40}Ar abundance. As was the case without impacts, for both linearly and exponentially decreasing pressures, the ^{36}Ar abundance can be matched over $0.4 \leq v_f \leq 5.0$, again for all s_f for linearly decreasing pressures and only $s_f < 20$ for exponentially decreasing pressures. However, the additional Ar supplied by impacts during the LHB requires more efficient sputtering from 0.8 Gyr. Consequently, the intensified sputtering needed to match ^{36}Ar values drives further fractionation such that the resulting $^{36}\text{Ar}/^{38}\text{Ar}$ values for any v_f are lower than those in Fig 4.8. In fact, for all $v_f > 0.6$, we find $^{36}\text{Ar}/^{38}\text{Ar} < 4.0$ at present-day. So, the subset of v_f values capable of reproducing both the present-day ^{36}Ar abundance and the $^{36}\text{Ar}/^{38}\text{Ar}$ ratio is much smaller ($0.4 \leq v_f \leq 0.6$ for both pressure cases) than when impacts are ignored.

Though impacts deliver significant amounts of ^{36}Ar and ^{38}Ar , crustal degassing is the most important factor in reproducing the observed ^{40}Ar abundance. About twice as much ^{40}Ar is supplied via outgassing than from impacts. Even with an additional source, ~ 6 times the amount of ^{40}Ar from outgassing and impact supply is required to be released from the crust – roughly the

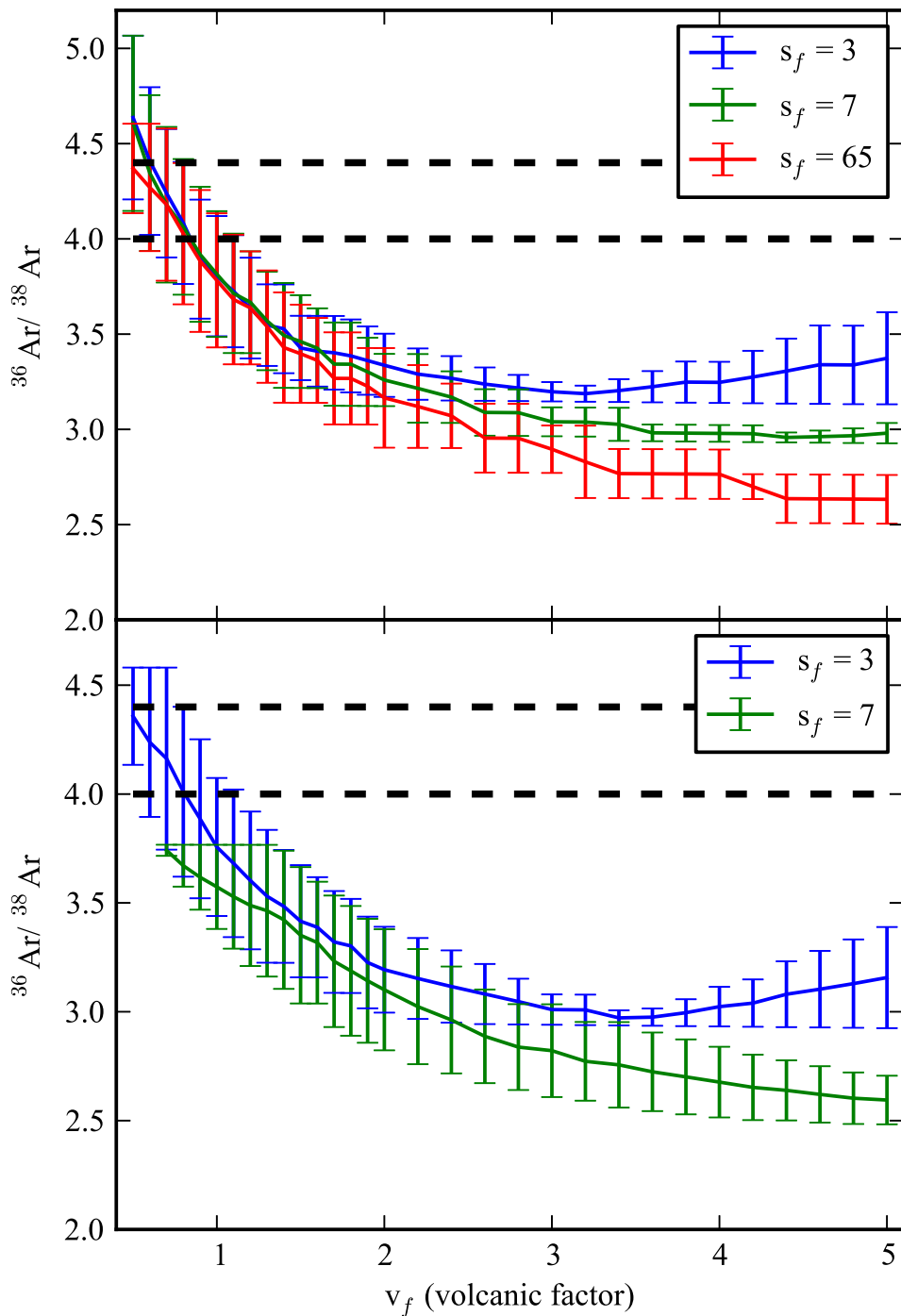


Figure 4.8: $^{36}\text{Ar}/^{38}\text{Ar}$ ratios are shown over the ranges of v_f , s_f , and P_0 for which the present-day ^{36}Ar abundance is reproduced given a linearly (top) or exponentially (bottom) decreasing atmosphere. The dashed black lines indicate our limits chosen for a simulation to have successfully reproduced $^{36}\text{Ar}/^{38}\text{Ar}$ measured by SAM.

same as the results without impacts for this range of v_f . However, since sputtering is more efficient in these simulations (more ^{36}Ar and ^{38}Ar must be removed), slightly more ^{40}Ar must be degassed than in simulations ignoring impacts. We find at least 54% of crustal ^{40}Ar is released for $v_f=0.4$ and at least 87% for $v_f=0.6$ for a linearly decreasing pressure, while the values increase to 66% and 92% for an exponentially decreasing pressure.

With impacts included in the model, the resultant parameter space that can successfully reproduce present-day observations is smaller than when impacts are ignored. The inclusion of impact delivery increases the total amount of argon supplied to the atmosphere, necessitating a small increase in the total lost due to sputtering. The minimum amount of atmospheric ^{36}Ar that must escape to space increases by nearly a factor of 2 (to 6.7×10^{-5} mbar), such that 54–72% of ^{36}Ar supplied to the atmosphere is lost. The minimum ^{40}Ar lost increases as well – 25–33% must be lost ($3.4\text{--}7 \times 10^{-2}$ mbar).

4.4 Varying the fractionation factor

In Chapter 3 we showed that the homopause-exobase separation distance and the upper atmospheric temperatures vary significantly with season and location. This leads to a range of fractionation of all species at the exobase. In the model, sputtering at the exobase is proportional to the relative abundance of Ar to CO_2 . An increase in the separation distance or a decrease in the thermospheric temperature increases the relative abundance of Ar isotopes ($R_{X/44}$ in Eq. 4.11). The $\Delta\mu$ term in the exponential of Eq. 3.8 enhances the fractionation more for lighter isotopes. Thus, an increase in the fractionation removes a larger proportion of light isotopes at each time step. We examine a few consequences below. Impacts have not been included in order to focus solely on the fractionation.

Increased fractionation has the effect of removing more total Ar and reducing the $^{36}\text{Ar}/^{38}\text{Ar}$ value for a given sputtering factor. For instance, all curves in the ‘‘Sputtering’’ column in the top two rows of Fig. 4.5 and the top two rows of Figs. 4.6 and 4.8 decrease more rapidly and reach lower present-day values.

If we first restrict those simulations that reproduce the present-day ^{36}Ar as in the preceding section the change from the results presented is minimal. In the linearly decreasing pressure case, the ^{36}Ar abundance can be reproduced for the full range of v_f and s_f values. In the exponential case, the range of s_f values decreases to offset the increase in $R_{36/44}$. However, those simulations that also reproduce the present-day $^{36}\text{Ar}/^{38}\text{Ar}$ ratio do so for a slightly lower v_f range and s_f range. The increased fractionation between ^{36}Ar and ^{38}Ar at every time step has two main effects. One is that the present-day abundances and ratios are reproduced with lower amounts of total ^{36}Ar (lower v_f range). And also, for a given v_f , $^{36}\text{Ar}/^{38}\text{Ar}$ is reproduced for those runs where a smaller fraction of the outgassed ^{36}Ar is removed. The lower limit of the present-day $^{36}\text{Ar}/^{38}\text{Ar}$ ($^{36}\text{Ar}/^{38}\text{Ar}=4.0$) is the limiting factor.

Conversely, for less fractionation at the exobase (smaller Δz or T), less Ar is removed at each time step, the drop in $^{36}\text{Ar}/^{38}\text{Ar}$ is less precipitous, and both more total ^{36}Ar is lost (from $v_f > 1.1$) and a higher fraction of the ^{36}Ar inventory is lost.

In Fig. 4.9 we present the same exobase-homopause separation distances and scale heights from Fig. 3.6, though the dashed lines have been changed. Here, the dashed lines represent the mean percentage of ^{36}Ar lost when the fractionation from the homopause to the exobase is varied between $a_{36/38} = 1.1$ (93%) and $a_{36/38}=2.7$ (36%). The fractionation and loss decrease as clockwise in the figure. The mean percentage reported for a given fractionation factor are derived from the range of ^{36}Ar loss in those simulations that reproduce the present-day ^{36}Ar abundance and $^{36}\text{Ar}/^{38}\text{Ar}$ ratio. There is variation about those mean values from a few to $\sim 10\%$, with an average of 4.5%. As discussed, less fractionation leads to higher total loss. For the centroid of the distribution, we find that 66% of any Ar introduced has been lost to space via sputtering .

4.5 Discussion and conclusions

The results given above illustrate the combinations of possible outgassing rates and sputtering rates that generate argon isotopic evolution scenarios consistent with observations. Along with crustal release of ^{40}Ar and impactor delivery and erosion, these processes have shaped the isotopic

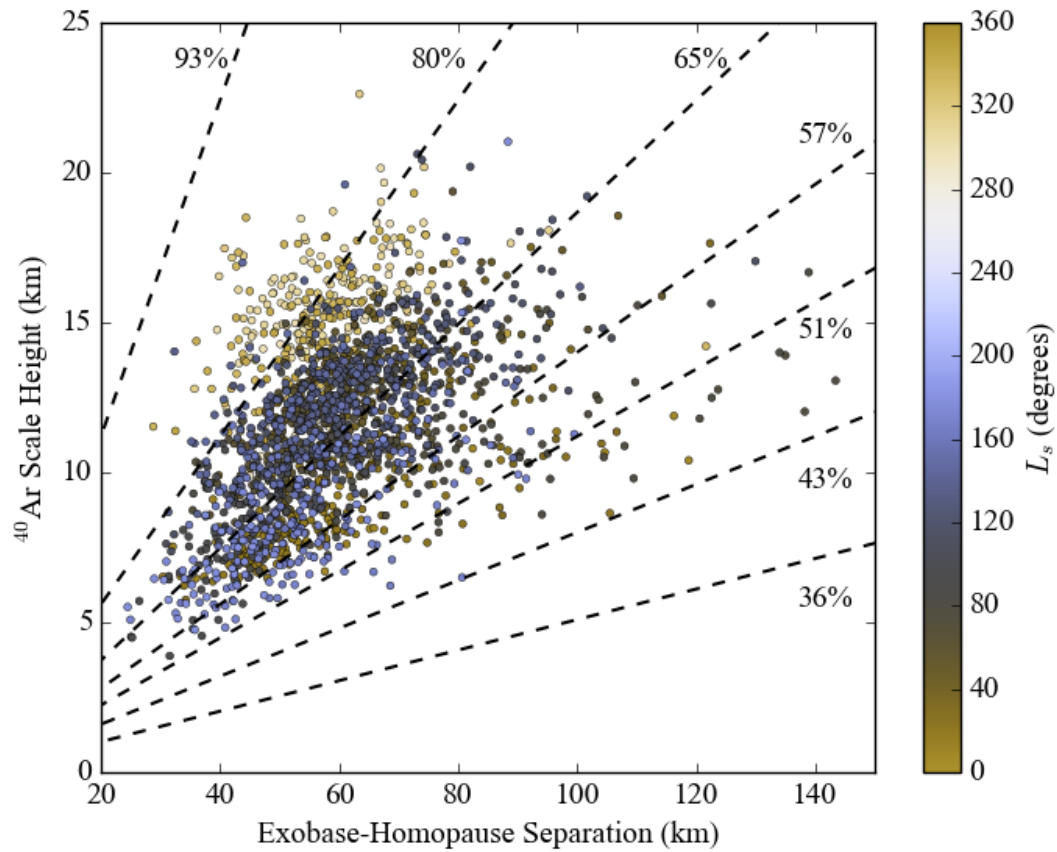


Figure 4.9: Separation distance between the exobase and homopause H_{Ar} scale heights derived in Chapter 3 from NGIMS densities. Dashed lines are lines of constant fractionation for $a_{36/36} = 1.1, 1.2, 1.3, 1.4, 1.6, 1.9, 2.7$ from the top left clockwise. Percentages shown are the mean percent loss of ^{36}Ar of simulations consistent with the present-day $^{36}\text{Ar}/^{38}\text{Ar}$ for a given fractionation.

ratios observed in Mars' atmosphere today. These results have implications for our understanding of the escape history of the Martian atmosphere and the outgassing history of the interior. Below, we discuss the context of the results for Martian atmospheric evolution and the robustness of the model given our assumptions regarding outgassing, sputtering, and the CO₂ history.

4.5.1 Sputtering

Given the amount of ³⁶Ar and ³⁸Ar outgassed from the crustal production function we use, loss and fractionation are required from 4.0 Gya. We have shown that our model reproduces the observed isotopic abundances via sputtering over a range of parameters considered. In Section 4.2.3.1, we described the difficulties in modeling sputtering; few measurements exist to accurately determine the present rate and, though it is likely a function of the solar EUV flux, estimating the rates during earlier Martian epochs produces a wide range of scenarios. We have accounted for such uncertainties by considering present and past rates (based on the estimates of Chassefière and Leblanc (2011)) within a range of two orders of magnitude, by introducing the variable s_f . However, fractionation of the isotopes due to sputtering is calculated by their relative separation between the homopause and exobase. Less fractionation leads to more total Ar lost for consistency with present-day measurements.

Argon escape rates depend on the mixing ratio of Ar, so these rates are tied to CO₂ abundances, which mitigate the amount of argon that is sputtered for a given s_f . So we find that for a linearly decreasing pressure, a sputtering rate of 1–100× that of Chassefière and Leblanc (2011) can reproduce the observed argon isotopic abundances (possibly also for $s_f > 100$, though that is our upper limit), but for an exponentially decreasing pressure, s_f must be less than 6. That is, a slowly decaying pressure reduces argon sputtering for higher s_f values, whereas a quick decrease in pressure causes intense sputtering and fractionation necessitating low s_f values. Since we do not know the shape of CO₂ abundance through time, we cannot conclude which s_f is most likely, though we prefer an early, rapid pressure decrease, and thus, lower s_f values. We have found that, over the full parameter space considered, 48–63% of atmospheric ³⁶Ar (~60 – 70% with the mean

fractionation from Chapter 3) and 18–37% of atmospheric ^{40}Ar were lost over the last 4.0 Gyr. Though we have not simultaneously modeled other atmospheric species (CO_2 , N, etc), they would also have been subject to sputtering in the upper atmosphere. These findings suggest that the evolutions of other atmospheric species may also have been influenced significantly by sputtering.

If, after a period of hydrodynamic escape, a large fractionated reservoir of ^{36}Ar and ^{38}Ar remains 4.4 Gya, our assumption of an initially Ar-free atmosphere is not valid. The revised model of Pepin (1994), suggests 10^{-13} g/g-Mars (about half the present-day abundance) could have existed in the atmosphere after hydrodynamic escape. Though $^{36}\text{Ar}/^{38}\text{Ar}$ was likely only fractionated about 10% from its primordial value (with only one stage of escape), we ran simulations with an isotopic ratio equal to today's (4.2). In this end-member case, we find the present-day ^{36}Ar and ^{38}Ar value can be reproduced if, at minimum, 45% of ^{36}Ar is lost to space via sputtering. This reduces our lower limit of the fraction of ^{36}Ar sputtered by only a small amount.

4.5.2 Outgassing of the mantle and crust

Compared to estimates based on photogeologic evidence, thermochemical models of the interior, e.g., Morschhauser et al. (2011), indicate that crustal production and outgassing were likely very strong early in Martian history. An earlier study of argon isotopic evolution (Hutchins and Jakosky, 1996) used an outgassing model based on Greeley and Schneid (1991) and concluded that the outgassing rate must have been a few to a hundred times greater to produce the observed argon abundances or that other processes must have played a role. Here, we found that with the added strong early release of volatiles prior to 3.7 Gya, 0.5–5.0 times the outgassing rate is consistent with ^{36}Ar abundances. Only v_f between 0.5 and 1.1 is also consistent with the $^{36}\text{Ar}/^{38}\text{Ar}$ ratio, though, because higher quantities of atmospheric argon require more total sputtering that excessively fractionates ^{36}Ar and ^{38}Ar . If exogenic argon is supplied via impactors during the LHB, the range of v_f values decreases further.

However, within these ranges of v_f , at least 4–10 times more ^{40}Ar must have been released from the interior. Early outgassing and impactors add little more ^{40}Ar than the Greeley and Schneid

(1991) rate due to the lack of decayed ^{40}K , so the conclusion regarding the paucity of outgassed ^{40}Ar of Hutchins and Jakosky (1996) and Leblanc et al. (2012) remains: crustal degassing must have been a significant source of atmospheric argon. We find that at least 30% of crustal ^{40}Ar must be released, though in some cases more than 90% is necessary. We have also run simulations with initial mantle ^{40}K concentrations of 0.36 and 0.45 ppm (see Section 4.2.1) and find that the lower and upper limits of γ given in Table 3 vary by less than ± 0.1 . The amount of volcanically outgassed ^{40}Ar increases with higher initial $[^{40}\text{K}]$ such that slightly less crustal degassing is required.

Our lower limit is similar to estimates of Earth’s crustal release Pujol et al. (2013) and may suggest significant crustal erosion over Mars’ history was likely, but the lack of a developed model for a mechanism that extracts Ar from minerals and transports it to the surface precludes a quantitative interpretation of crustal erosion. In general, our findings are higher than results from Leblanc et al. (2012), likely a result of using only $v_f < 1.2$ (from $^{36}\text{Ar}/^{38}\text{Ar}$ constraints), using a slightly lower mantle ^{40}K concentration (0.4 ppm compared to 0.44 ppm), and allowing sputtering rates to be 100 times larger than the nominal case. Less outgassing and lower mantle ^{40}K values increase the amount of atmospheric ^{40}Ar that must be supplied by the crust, resulting in higher values of γ . Higher sputtering rates require more replenishment of atmospheric ^{40}Ar , so for a given v_f more crustal degassing is required.

4.5.3 Early $^{40}\text{Ar}/^{36}\text{Ar}$ values

Though inclusion of crustal degassing allowed us to reproduce the present-day $^{40}\text{Ar}/^{36}\text{Ar}$ ratio, one feature of the evolution of atmospheric argon that is not reproduced in our model is the high $^{40}\text{Ar}/^{36}\text{Ar}$ ratio (626) at 4.16 Gya measured in the ALH 84001 meteorite by Cassata et al. (2012) (Table 4.1). In our model, even for efficient outgassing of the mantle and crust, not enough radiogenic argon is released by this time to increase the early $^{40}\text{Ar}/^{36}\text{Ar}$ ratio. Cassata et al. (2012) suggest a few possibilities that could cause the isotopic ratio to jump early in Martian history: high magmatic K concentrations, low magmatic ^{36}Ar concentrations, low initial atmospheric ^{36}Ar concentrations, or very efficient outgassing. They include effects of impacts during this period, whereas

we have not, though they may have underestimated the effects of impact delivery, which could have been another mechanism increasing the ratio. Impact erosion is non-fractionating, so it should not play an important role in changing isotopic ratios. Cassata et al. (2012) conclude that low initial pressures (< 1 bar) and thus, little initial atmospheric ^{36}Ar , best reproduce the measured value of $^{40}\text{Ar}/^{36}\text{Ar}$ 4.16 Gya, as the higher $^{40}\text{Ar}/^{36}\text{Ar}$ of degassed argon more easily dominated the atmospheric ratio.

All of our simulations begin with no ^{36}Ar in the atmosphere, yet we cannot reproduce the observed ratio with high outgassing rates. This difference is largely accounted for by magmatic abundances. Cassata et al. (2012) used an initial magmatic K concentration of 1300-3300 ppm, corresponding to a crustal enrichment in K of 5-10, and an ^{36}Ar concentration in outgassed magmas $\sim 3\text{-}50\times$ smaller than our concentration. Because their outgassed $^{40}\text{Ar}/^{36}\text{Ar}$ ratio is higher at all times, the atmospheric ratio increases more quickly. If outgassing and loss prior to 4.4 Gya depleted the mantle in ^{36}Ar , a reduced $^{36}\text{Ar}/^{40}\text{K}$ ratio could explain the early elevated $^{40}\text{Ar}/^{36}\text{Ar}$ value. Similarly, we may be underestimating the mantle $^{40}\text{K}/\text{K}$, which will have the same effect. Or, if early catastrophic outgassing released a substantial amount of gas and little was lost, the ratio may have been elevated by the time our model begins. Pujol et al. (2013) find that a high $^{40}\text{Ar}/^{36}\text{Ar}$ ratio on Earth (143 ± 24) requires such a process within the first ~ 170 Myr. While increased ^{40}K concentrations alone cannot account for this difference, we have not run simulations with reduced proportions of mantle ^{36}Ar or significant amounts of atmospheric argon prior to 4.4 Gya. These changes would force the atmospheric $^{40}\text{Ar}/^{36}\text{Ar}$ to increase more rapidly and require less crustal degassing to reproduce measurements from both ALH 84001 and present-day. Alternatively, processes that will fractionate atmospheric argon may also be important. We have assumed that a global magnetic field prevents any sputtering prior to the disappearance of the field ~ 4.0 Gya. In simulations with a sputtering turn-on time prior to 4.1 Gya, the ALH 84001 $^{40}\text{Ar}/^{36}\text{Ar}$ ratio can be reproduced quite easily with low initial pressures. Though we consider sputtering at such a time in Mars' history unlikely, this result illustrates that some fractionation process may be responsible for the observed $^{40}\text{Ar}/^{36}\text{Ar}$ ratio.

4.5.4 Impacts

Impacts have not likely been an important process driving atmospheric volatile evolution during the past few billion years, but models of impact delivery during the LHB suggest significant amounts of volatiles could have been supplied in a few hundred million years. Atmospheric erosion, a non-fractionating process, would have occurred as well, but probably played a much smaller role. LHB impactors could have supplied an amount of ^{36}Ar and ^{38}Ar roughly equal to today's total reservoir. For a wide range of pressures, sputtering is able to remove a significant amount of the combined outgassed-impactor supplied Ar and can fractionate the isotopes to the observed ratio. In our model, impacts have a similar effect as early increased volcanic outgassing – additional ^{36}Ar and ^{38}Ar are supplied to the atmosphere prior to 3.8 Gya. Since outgassing diminishes rapidly by this time, including impacts in a simulation has the same outcome as increasing the value of v_f . So when impacts are included, we find the range of v_f values consistent with present-day measurements to be lower than without, but the the total amount of Ar that was lost over time does not drastically change.

4.5.5 Early atmospheric pressure

The atmospheric conditions of Noachian and pre-Noachian times are of great interest, yet remain fairly uncertain. We considered a wide range of possible atmospheric pressures for early Mars in our simulations (6 mbar – 10 bar) and nearly all were consistent with present-day Ar isotopic ratios, given some values of v_f and s_f . At the lower limit ($s_f = 1$), the minimum P_0 is 44 mbar for a linearly decreasing pressure atmosphere and 68 mbar for the exponentially decreasing case, while at the highest s_f values the maximum P_0 is 10 bar.

With such a vast range of possible sputtering histories, the initial pressure cannot be constrained. But we have treated CO_2 in a very simple way – given some initial pressure, CO_2 decreases either linearly or exponentially, constrained by the present-day atmospheric pressure. This has allowed us to understand how several parameters affect argon evolution, but is not a simultaneous

treatment of the processes that affect CO₂. CO₂ is outgassed from the interior and subject to sputtering, but also interacts with the crust through carbonate formation, is involved in more complicated chemistry in the upper atmosphere, and is lost to space through mechanisms other than sputtering. Though we have not attempted to track these rates through time, we can compare the amounts of sputtered CO₂ (related only to s_f) and the total CO₂ loss ($P_0 - P_f$) that allow Ar abundances to be reproduced over the full range of other parameters (Fig. 4.10). We see that when 10 mbar of CO₂ is sputtered, our model requires a total of nearly 100 mbar (up to 1 bar) for a linearly (exponentially) decreasing pressure to be removed from the atmosphere. When we increase s_f to 10 (50 mbar of sputtered CO₂), the results are consistent with other processes removing 500-1000 mbar of additional CO₂. All our results suggest that other CO₂ processes must be responsible for additional CO₂ loss not attributable to sputtering, though changes in some of our chosen parameters like the fractionation factors and yields would certainly effect these results. If we have systematically overestimated the amount of Ar sputtered relative to CO₂ or ³⁶Ar relative to ³⁸Ar, a higher fraction of total CO₂ loss would have been due to sputtering (the ranges in Fig. 4.10 would shift downward). Indeed, the observed $a_{36/38}$ values are consistent with higher values of s_f , such that >100 mbar in the linear case and > 10 mbar in the exponential case are common in simulation results.

Furthermore, while we have discussed Ar and CO₂ sputtering, we have neglected sputtering of oxygen. Luhmann et al. (1992) found that sputtering to remove 30 times as much O as CO₂. O in the thermosphere is a product of the photodissociation of CO₂ and H₂O. If we assume all the O came from CO₂, our integrated sputtered CO₂ values increase by 15. This pushes the range of sputtered CO₂ to a few hundred mbar up to a bar, with smaller fraction of the reported CO₂ loss required from other processes. Of course, some fraction surely came from H₂O, so lower values are plausible but entail significant water loss from the early atmosphere.

Useful future work would be to model the time-history of all CO₂ and Ar sources and sinks to see how they change together. If the true atmospheric pressure did not oscillate substantially throughout Mars' history and decreased with time, our results are robust regardless of what pro-

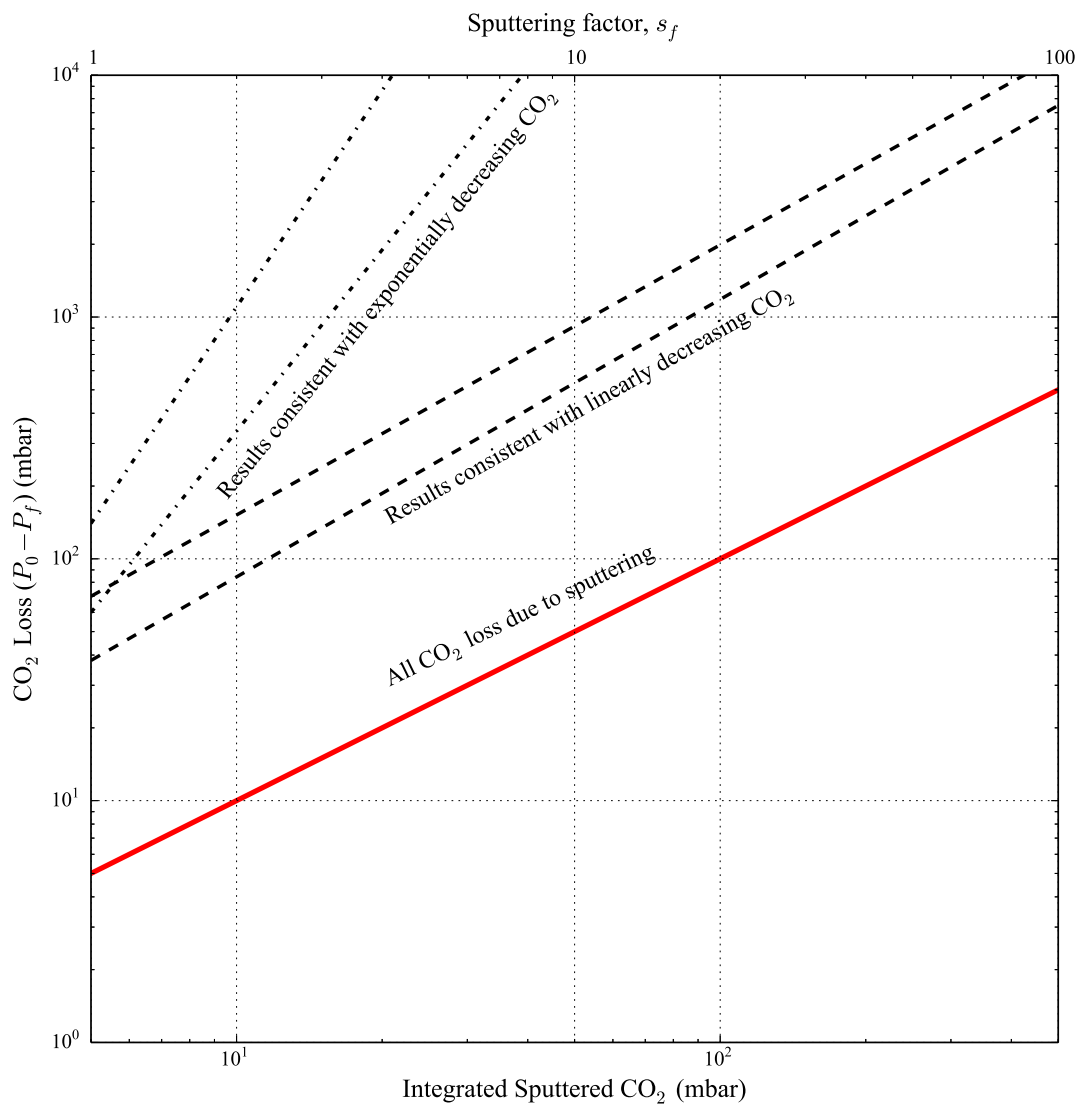


Figure 4.10: Entire range of s_f (and corresponding integrated sputtered CO_2) and P_0 (expressed as total CO_2 lost) values considered in our standard model. The solid one-one line shows where CO_2 loss is equal to the total CO_2 sputtered. The ranges of these parameters for which the Ar isotopic abundances can be reproduced are shown for the linearly decreasing case (dashed) and exponentially decreasing case (dashed-dotted). There is no significant change when impacts are included.

cesses have been most important in driving CO₂ evolution.

4.5.6 “Restored” ⁴⁰Ar/³⁶Ar value

By adding the amounts of time-integrated loss of ³⁶Ar and ⁴⁰Ar we determined to be compatible with observations to their respective present-day abundances, a “restored” value of the ⁴⁰Ar/³⁶Ar ratio can be calculated. This value is useful in that it represents what the atmospheric ratio would be in the absence of any escape. The observed ⁴⁰Ar/³⁶Ar value in Mars’ atmosphere today is 1900 (Table 4.1), over 6× that of the terrestrial atmosphere. If we assume that both Earth and Mars have had similar outgassing histories, than we should expect Mars’ restored ⁴⁰Ar/³⁶Ar to be nearly equivalent to Earth’s atmospheric ratio. Our results have a range of restored values from 930–1470 (Fig. 4.11), still ~3–5 times that of Earth’s present-day atmospheric ratio. This difference could reflect problems with the model or inherent distinctions in the evolutions of Earth and Mars.

In our model, more ³⁶Ar would have had to been added to the atmosphere and subsequently removed for a lower restored value to be achieved. However, sputtering is so efficient at all times, that for any $v_f > 1.1$, the ³⁶Ar/³⁸Ar ratio could not be matched. It is possible that for sputtering evolutions with a low rate today yet still very strong early (like the shape of the Luhmann et al. (1992) curve in 4.3), the argon abundances can increase over the past few billion years as outgassing becomes more dominant than sputtering. In this scenario, the present-day ³⁶Ar/³⁸Ar ratio could be reproduced for higher v_f values, which translates to more total escape of ³⁶Ar. Such an underestimation of the total ³⁶Ar loss would lower the restored value closer to that of Earth’s atmosphere because ³⁶Ar is lost more readily than ⁴⁰Ar. Any loss prior to 4.0 Gya would also reduce the restored value, since little ⁴⁰Ar would have been in the atmosphere, possibly from hydrodynamic escape. Based on results of Pepin (1994), if we assume $\sim 2 \times 10^{-12}$ g/g-Mars of ³⁶Ar could have been lost from a primary atmosphere, our restored ⁴⁰Ar/³⁶Ar lower limits are ~ 250 and 100 for runs with and without impacts.

Alternatively, the higher restored value could be a result of the crustal degassing rates we cal-

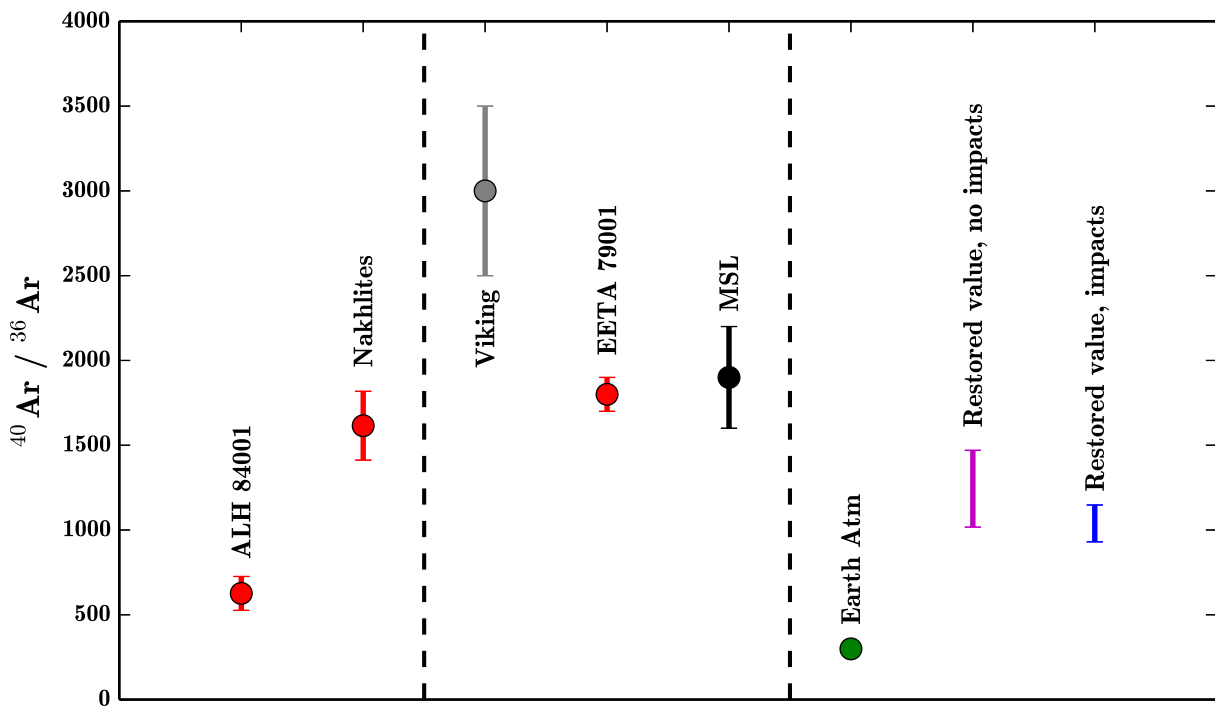


Figure 4.11: Values of $^{40}\text{Ar}/^{36}\text{Ar}$ from past epochs (left) and the current Martian atmosphere (middle), along with the restored values from this work (right). The present-day terrestrial value is shown in green.

culated. We have shown that the ^{40}Ar abundance is determined by the amount of crustal degassing, though the range of this degassing remains relatively unconstrained (30–93%). In modeling Earth's atmospheric ^{40}Ar evolution, Pujol et al. (2013) found solutions consistent with 0–50% crustal degassing of Ar. If release of Ar from the crust was indeed a more active process on Mars than on Earth, the higher rate of $^{40}\text{Ar}/^{36}\text{Ar}$ supplied to the atmosphere over time can account for some of the discrepancy between the restored value and the terrestrial value. In fact, if we remove all the ^{40}Ar contributed by crustal degassing in our models, the $^{40}\text{Ar}/^{36}\text{Ar}$ value can be reduced to 372, much closer to the terrestrial value. Unfortunately, without a better understanding of the history of Martian sputtering, hydrodynamic escape, or the crustal degassing efficiency of either Earth or Mars disentangling the difference in the restored $^{40}\text{Ar}/^{36}\text{Ar}$ values is difficult.

Chapter 5

Summary

Geomorphic and mineralogical evidence indicate that liquid water was once prevalent on Mars and isotopes of major atmospheric species demonstrate that atmospheric loss from an early atmosphere has occurred. This thesis has quantified the amount of Ar that has escaped from ancient Mars and found that it has been significant – about 2/3 of any ^{36}Ar introduced into the atmosphere has been lost. Quantifying the Ar loss required the completion of three main tasks, each of which I summarize below.

First, I determined homopause altitudes by extrapolating ratios of N_2/Ar densities measured in the upper atmosphere by the NGIMS instrument onboard the MAVEN spacecraft downward to the known value in the well mixed atmosphere measured by the SAM instrument on the Curiosity rover. The mean homopause altitude is 110 km, though there is substantial variability with latitude, local time, and season. Homopause altitudes are higher on the dayside and in southern summer and lowest around 5 a.m. at $L_s \sim 90^\circ$. Estimates of the wave-turbopause based on gravity wave activity reflected in profiles of static stability and temperature standard deviations (from NGIMS and MCS) show similar variations. Wave dissipation generates the turbulence responsible for the mixing that defines the homosphere. At higher altitudes, waves propagate more freely, wave dissipation is weaker, and molecular diffusion dominates such that species separate according to their individual scale heights. The homo/turbopause does not occur at a constant density level, suggesting differences in the dominant breaking waves.

Exobase altitudes and scale heights were also derived from NGIMS densities for ~ 1 Martian

year. From the exobase-homopause separation distance and the thermospheric temperature, I determined the degree of fractionation of ^{36}Ar and ^{38}Ar from the lower atmosphere to the exobase, where escape to space occurs. This derived fractionation is consistent with observations of the $^{36}\text{Ar}/^{38}\text{Ar}$ ratio during the fourth deep dip campaign. Accounting for the variability in the derived parameters, on average there is 1.3 times as much ^{36}Ar relative to ^{38}Ar at the exobase than in the well-mixed lower atmosphere. Using Rayleigh distillation, which describes the change in an isotopic ratio as particles are removed from the system, I find that the present-day Ar isotopic ratios indicate a loss 63% of Ar from its initial inventory. However, this method ignores other processes that have supplied or removed atmospheric Ar during Mars' history.

For a more accurate interpretation of the isotopic record, I developed a box model that tracks the supply and loss of Ar from volcanic outgassing, impacts, crustal erosion, and sputtering from 4.4 Gyr ago to the present-day. Over a wide range of parameters, the present-day abundance of ^{36}Ar is reproduced, but atmospheric sputtering efficiently lowers $^{36}\text{Ar}/^{38}\text{Ar}$ such that only a limited range of Ar loss is compatible with the present-day ratio. The percent of all ^{36}Ar ever introduced into the atmosphere that has escaped to space using the mean fractionation derived from NGIMS measurements is $66 \pm 5\%$. ^{36}Ar is a trace species, but these results suggest that several hundred mbar of CO_2 were removed from sputtering. Of course, CO_2 has also been lost to space through photochemical escape and pickup by the solar wind and locked up in subsurface rocks as carbonates.

A substantial loss of CO_2 seems unavoidable, though an intensely studied question remains: What were the exact conditions of the early Martian atmosphere? I believe this work has provided some constraints for the numerous scientists focused on answering that question. It is down this path that the inquiries can continue about the extent of the water, the timescale of clement conditions, and, ultimately, about whether life could form.

Bibliography

- Anders, E. and Owen, T. (1977). Mars and earth: Origin and abundance of volatiles. Science, 198(4316):453–465.
- Arevalo, R., McDonough, W. F., and Luong, M. (2009). The K/U ratio of the silicate Earth: Insights into mantle composition, structure and thermal evolution. Earth and Planetary Science Letters, 278:361–369.
- Atreya, S. K., Trainer, M. G., Franz, H. B., Wong, M. H., Manning, H. L. K., Malespin, C. A., Mahaffy, P. R., Conrad, P. G., Brunner, A. E., Leshin, L. A., Jones, J. H., Webster, C. R., Owen, T. C., Pepin, R. O., and Navarro-González, R. (2013). Primordial argon isotope fractionation in the atmosphere of Mars measured by the SAM instrument on Curiosity and implications for atmospheric loss. Geophys. Res. Lett. , 40:5605–5609.
- Baker, V. R. (2001). Water and the martian landscape. Nature, 412(6843):228.
- Baker, V. R. (2006). Geomorphological evidence for water on mars. Elements, 2(3):139–143.
- Barlow, N. (2008). Mars: An introduction to its interior, surface and atmosphere, volume 8. Cambridge University Press.
- Barnes, J. R. (1990). Possible effects of breaking gravity waves on the circulation of the middle atmosphere of mars. Journal of Geophysical Research: Solid Earth, 95(B2):1401–1421.
- Basilevsky, A. T. and Head, J. W. (2003). The surface of venus. Reports on Progress in Physics, 66(10):1699.
- Bibring, J.-P., Langevin, Y., Mustard, J. F., Poulet, F., Arvidson, R., Gendrin, A., Gondet, B., Mangold, N., Pinet, P., Forget, F., et al. (2006). Global mineralogical and aqueous mars history derived from omega/mars express data. science, 312(5772):400–404.
- Bishop, J. L., Dobreá, E. Z. N., McKeown, N. K., Parente, M., Ehlmann, B. L., Michalski, J. R., Milliken, R. E., Poulet, F., Swayze, G. A., Mustard, J. F., et al. (2008). Phyllosilicate diversity and past aqueous activity revealed at mawrth vallis, mars. Science, 321(5890):830–833.
- Blamont, J.-E. (2001). Alkali metal cloud experiments in the upper atmosphere. In Bleeker, J. A., Geiss, J., and Huber, M. C. E., editors, The Century of Space Science, Volume I, chapter 7, pages 189–202. Kluwer Academic Publishers, Dordrecht.
- Bland, P. A., Moore, E. A., Wright, I., and Widdowson, M. (2004). An introduction to the solar system. Cambridge University Press.

- Bogard, D. D., Clayton, R. N., Marti, K., Owen, T., and Turner, G. (2001). Martian Volatiles: Isotopic Composition, Origin, and Evolution. Space Sci. Rev., 96:425–458.
- Bougher, S., Engel, S., Roble, R., and Foster, B. (1999). Comparative terrestrial planet thermospheres: 2. solar cycle variation of global structure and winds at equinox. Journal of Geophysical Research, 104(E7):16591–16611.
- Bougher, S., Fesen, C., Ridley, E., and Zurek, R. (1993). Mars mesosphere and thermosphere coupling: Semidiurnal tides. Journal of Geophysical Research: Planets, 98(E2):3281–3295.
- Bougher, S., Jakosky, B., Halekas, J., Grebowsky, J., Luhmann, J., Mahaffy, P., Connerney, J., Eparvier, F., Ergun, R., Larson, D., et al. (2015). Early maven deep dip campaign reveals thermosphere and ionosphere variability. Science, 350(6261):aad0459.
- Bougher, S. W., Bell, J. M., Murphy, J. R., Lopez-Valverde, M. A., and Withers, P. G. (2006). Polar warming in the Mars thermosphere: Seasonal variations owing to changing insolation and dust distributions. Geophys. Res. Lett., 33:L02203.
- Bougher, S. W., Brain, A., Fox, J. L., Gonzalez-Galindo, F., Simon-Wedlund, C., and Withers, P. G. (2017). Upper neutral atmosphere and ionosphere. The atmosphere and climate of Mars, 18:433.
- Bougher, S. W. and Dickinson, R. (1988). Mars mesosphere and thermosphere: 1. global mean heat budget and thermal structure. Journal of Geophysical Research: Space Physics, 93(A7):7325–7337.
- Bougher, S. W., Pawlowski, D., Bell, J. M., Nelli, S., McDunn, T., Murphy, J. R., Chizek, M., and Ridley, A. (2015). Mars Global Ionosphere-Thermosphere Model: Solar cycle, seasonal, and diurnal variations of the Mars upper atmosphere. Journal of Geophysical Research (Planets), 120:311–342.
- Bougher, S. W., Roeten, K. J., Olsen, K., Mahaffy, P. R., Benna, M., Elrod, M., Jain, S. K., Schneider, N. M., Deighan, J., Thiemann, E., Eparvier, F. G., Stiepen, A., and Jakosky, B. M. (2017). The structure and variability of Mars dayside thermosphere from MAVEN NGIMS and IUVS measurements: Seasonal and solar activity trends in scale heights and temperatures. Journal of Geophysical Research (Space Physics), 122:1296–1313.
- Boynton, W., Ming, D., Kounaves, S., Young, S., Arvidson, R., Hecht, M., Hoffman, J., Niles, P., Hamara, D., Quinn, R., et al. (2009). Evidence for calcium carbonate at the mars phoenix landing site. Science, 325(5936):61–64.
- Brain, D. A. and Jakosky, B. M. (1998). Atmospheric loss since the onset of the Martian geologic record: Combined role of impact erosion and sputtering. J. Geophys. Res., 103:22689–22694.
- Briggs, G. A. and Leovy, C. B. (1974). Mariner 9 observations of the mars north polar hood. Bulletin of the American Meteorological Society, 55(4):278–296.
- Cabrol, N. A. and Grin, E. A. (1999). Distribution, classification, and ages of martian impact crater lakes. Icarus, 142(1):160–172.
- Carr, M. H. (1979). Formation of martian flood features by release of water from confined aquifers. Journal of Geophysical Research: Solid Earth, 84(B6):2995–3007.

- Carr, M. H. and Head, J. W. (2010). Geologic history of mars. Earth and Planetary Science Letters, 294(3-4):185–203.
- Carter, J., Loizeau, D., Mangold, N., Poulet, F., and Bibring, J.-P. (2015). Widespread surface weathering on early mars: A case for a warmer and wetter climate. Icarus, 248:373–382.
- Cassata, W. S., Shuster, D. L., Renne, P. R., and Weiss, B. P. (2010). Evidence for shock heating and constraints on Martian surface temperatures revealed by $^{40}\text{Ar}/^{39}\text{Ar}$ thermochronometry of Martian meteorites. Geochim. Cosmochim. Acta , 74:6900–6920.
- Cassata, W. S., Shuster, D. L., Renne, P. R., and Weiss, B. P. (2012). Trapped Ar isotopes in meteorite ALH 84001 indicate Mars did not have a thick ancient atmosphere. Icarus, 221:461–465.
- Chabrilat, S., Kockarts, G., Fonteyn, D., and Brasseur, G. (2002). Impact of molecular diffusion on the CO_2 distribution and the temperature in the mesosphere. Geophysical research letters, 29(15):19–1.
- Chassefière, E. and Leblanc, F. (2004). Mars atmospheric escape and evolution; interaction with the solar wind. Planetary and Space Science, 52(11):1039–1058.
- Chassefière, E. and Leblanc, F. (2011). Methane release and the carbon cycle on Mars. Planet. Space Sci. , 59:207–217.
- Chassefière, E., Leblanc, F., and Langlais, B. (2007). The combined effects of escape and magnetic field histories at Mars. Planet. Space Sci. , 55:343–357.
- Chaufray, J. Y., Modolo, R., Leblanc, F., Chanteur, G., Johnson, R. E., and Luhmann, J. G. (2007). Mars solar wind interaction: Formation of the Martian corona and atmospheric loss to space. Journal of Geophysical Research (Planets), 112:9009.
- Coplen, T. B., Hoppo, J., Boehike, J., Peiser, H., and Rieder, S. (2002). Compilation of minimum and maximum isotope ratios of selected elements in naturally occurring terrestrial materials and reagents. U.S. Geological Survey WaterResources Investigations Report.
- Craddock, R. A. and Howard, A. D. (2002). The case for rainfall on a warm, wet early mars. Journal of Geophysical Research: Planets, 107(E11):21–1.
- Creasey, J. E., Forbes, J. M., and Hinson, D. P. (2006). Global and seasonal distribution of gravity wave activity in mars' lower atmosphere derived from mgs radio occultation data. Geophysical research letters, 33(1).
- Danilov, A. (1979). Ua kalgin. aa pokhunkov. variation of the turbopause level at polar region. Space Research XIX, 173.
- Danilov, A. D. (1984). Direct and indirect estimates of turbulence around the turbopause. Advances in Space Research, 4:67–78.
- de Niem, D., Kührt, E., Morbidelli, A., and Mutschmann, U. (2012). Atmospheric erosion and replenishment induced by impacts upon the Earth and Mars during a heavy bombardment. Icarus , 221:495–507.
- Dreibus, G. and Wanke, H. (1985). Mars, a volatile-rich planet. Meteoritics, 20:367–381.

- Dreibus, G. and Wanke, H. (1987). Volatiles on earth and Mars - A comparison. *Icarus*, 71:225–240.
- Ehlmann, B., Anderson, F., Andrews-Hanna, J., Catling, D., Christensen, P., Cohen, B., Dressing, C., Edwards, C., Elkins-Tanton, L., Farley, K., et al. (2016). The sustainability of habitability on terrestrial planets: Insights, questions, and needed measurements from mars for understanding the evolution of earth-like worlds. *Journal of Geophysical Research: Planets*, 121(10):1927–1961.
- Ehlmann, B. L. and Edwards, C. S. (2014). Mineralogy of the martian surface. *Annual Review of Earth and Planetary Sciences*, 42:291–315.
- Ehlmann, B. L., Mustard, J. F., Murchie, S. L., Bibring, J.-P., Meunier, A., Fraeman, A. A., and Langevin, Y. (2011). Subsurface water and clay mineral formation during the early history of mars. *Nature*, 479(7371):53.
- Ehlmann, B. L., Mustard, J. F., Murchie, S. L., Poulet, F., Bishop, J. L., Brown, A. J., Calvin, W. M., Clark, R. N., Des Marais, D. J., Milliken, R. E., et al. (2008). Orbital identification of carbonate-bearing rocks on mars. *Science*, 322(5909):1828–1832.
- England, S., Liu, G., Yiğit, E., Mahaffy, P., Elrod, M., Benna, M., Nakagawa, H., Terada, N., and Jakosky, B. (2017). Maven ngims observations of atmospheric gravity waves in the martian thermosphere. *Journal of Geophysical Research: Space Physics*, 122(2):2310–2335.
- Fassett, C. I. and Head, J. W. (2008). Valley network-fed, open-basin lakes on mars: Distribution and implications for noachian surface and subsurface hydrology. *Icarus*, 198(1):37–56.
- Forget, F., Hourdin, F., Fournier, R., Hourdin, C., Talagrand, O., Collins, M., Lewis, S. R., Read, P. L., and Huot, J.-P. (1999). Improved general circulation models of the Martian atmosphere from the surface to above 80 km. *J. Geophys. Res.*, 104:24155–24176.
- Forget, F., Montmessin, F., Bertaux, J.-L., González-Galindo, F., Lebonnois, S., Quemerais, E., Reberac, A., Dimarellis, E., and López-Valverde, M. A. (2009). Density and temperatures of the upper martian atmosphere measured by stellar occultations with mars express spicam. *Journal of Geophysical Research: Planets*, 114(E1).
- Forsberg-Taylor, N. K., Howard, A. D., and Craddock, R. A. (2004). Crater degradation in the martian highlands: Morphometric analysis of the sinus sabaesus region and simulation modeling suggest fluvial processes. *Journal of Geophysical Research: Planets*, 109(E5).
- Franz, H. B., Trainer, M. G., Malespin, C. A., Mahaffy, P. R., Atreya, S. K., Becker, R. H., Benna, M., Conrad, P. G., Eigenbrode, J. L., Freissinet, C., et al. (2017). Initial sam calibration gas experiments on mars: Quadrupole mass spectrometer results and implications. *Planetary and Space Science*, 138:44–54.
- Franz, H. B., Trainer, M. G., Malespin, C. A., Mahaffy, P. R., Atreya, S. K., Benna, M., Conrad, P. G., Eigenbrode, J. L., Freissinet, C., Manning, H. L. K., Prats, B. D., Raaen, E., and Wong, M. H. (2017). Revised $40\text{Ar}/14\text{N}$ for the Martian Atmosphere Based on SAM Calibration Gas Cell Results. In *Lunar and Planetary Science Conference*, volume 48 of *Lunar and Planetary Inst. Technical Report*, page 1449.
- Franz, H. B., Trainer, M. G., Wong, M. H., Mahaffy, P. R., Atreya, S. K., Manning, H. L., and Stern, J. C. (2015). Reevaluated martian atmospheric mixing ratios from the mass spectrometer on the curiosity rover. *Planetary and Space Science*, 109:154–158.

- Frey, H. and Schultz, R. A. (1988). Large impact basins and the mega-impact origin for the crustal dichotomy on mars. Geophysical Research Letters, 15(3):229–232.
- Fritts, D. C. (1982). Shear excitation of atmospheric gravity waves. Journal of the Atmospheric Sciences, 39(9):1936–1952.
- Fritts, D. C. (1984). Gravity wave saturation in the middle atmosphere: A review of theory and observations. Reviews of Geophysics, 22(3):275–308.
- Fritts, D. C., Wang, L., and Tolson, R. H. (2006). Mean and gravity wave structures and variability in the mars upper atmosphere inferred from mars global surveyor and mars odyssey aerobraking densities. Journal of Geophysical Research: Space Physics, 111(A12).
- Gardner, C. S., Zhao, Y., and Liu, A. Z. (2002). Atmospheric stability and gravity wave dissipation in the mesopause region. Journal of Atmospheric and Solar-Terrestrial Physics, 64:923–929.
- Genda, H. and Abe, Y. (2003). Survival of a proto-atmosphere through the stage of giant impacts: the mechanical aspects. Icarus, 164:149–162.
- Gillmann, C., Lognonné, P., Chassefière, E., and Moreira, M. (2009). The present-day atmosphere of Mars: Where does it come from? Earth and Planetary Science Letters, 277(3):384–393.
- Golombek, M. P., Grant, J. A., Crumpler, L. S., Greeley, R., Arvidson, R. E., Bell, J. F., Weitz, C. M., Sullivan, R., Christensen, P. R., Soderblom, L., et al. (2006). Erosion rates at the mars exploration rover landing sites and long-term climate change on mars. Journal of Geophysical Research: Planets, 111(E12).
- Gomes, R., Levison, H. F., Tsiganis, K., and Morbidelli, A. (2005). Origin of the cataclysmic Late Heavy Bombardment period of the terrestrial planets. Nature, 435:466–469.
- González-Galindo, F., Forget, F., López-Valverde, M. A., Angelats i Coll, M., and Millour, E. (2009). A ground-to-exosphere Martian general circulation model: 1. Seasonal, diurnal, and solar cycle variation of thermospheric temperatures. Journal of Geophysical Research (Planets), 114:E04001.
- Gråe Jørgensen, U., Appel, P. W. U., Hatsukawa, Y., Frei, R., Oshima, M., Toh, Y., and Kimura, A. (2009). The Earth-Moon system during the late heavy bombardment period - Geochemical support for impacts dominated by comets. Icarus, 204:368–380.
- Grady, M. M. and Wright, I. P. (2003). Elemental and Isotopic Abundances of Carbon and Nitrogen in Meteorites. Space Sci. Rev., 106:231–248.
- Greeley, R. and Schneid, B. D. (1991). Magma generation on Mars - Amounts, rates, and comparisons with earth, moon, and Venus. Science, 254:996–998.
- Gröller, H., Montmessin, F., Yelle, R., Lefèvre, F., Forget, F., Schneider, N., Koskinen, T., Deighan, J., and Jain, S. (2018). Maven/iuvs stellar occultation measurements of mars atmospheric structure and composition. Journal of Geophysical Research: Planets.
- Grott, M., Baratoux, D., Hauber, E., Sautter, V., Mustard, J., Gasnault, O., Ruff, S. W., Karato, S.-I., Debaille, V., Knapmeyer, M., Sohl, F., Van Hoolst, T., Breuer, D., Morschhauser, A., and Toplis, M. J. (2013). Long-Term Evolution of the Martian Crust-Mantle System. Space Sci. Rev., 174:49–111.

- Grott, M., Morschhauser, A., Breuer, D., and Hauber, E. (2011). Volcanic outgassing of CO₂ and H₂O on Mars. Earth and Planetary Science Letters, 308(3-4):391–400.
- Guzewich, S. D., Talaat, E. R., and Waugh, D. W. (2012). Observations of planetary waves and nonmigrating tides by the mars climate sounder. Journal of Geophysical Research: Planets, 117(E3).
- Haberle, R. M., Catling, D. C., Carr, M. H., and Zahnle, K. J. (2017). The early mars climate system. The atmosphere and climate of Mars, Edited by RM Haberle et al. ISBN: 9781139060172. Cambridge University Press, 2017, p. 497-525, pages 497–525.
- Hall, C. M., Holmen, S. E., Meek, C. E., Manson, A. H., and Nozawa, S. (2016). Change in turbopause altitude at 52 and 70deg N. Atmospheric Chemistry & Physics, 16:2299–2308.
- Hall, C. M. and Hoppe, U.-P. (1998). Estimates of turbulent energy dissipation rates from determinations of characteristic vertical wavenumber by EISCAT. Geophys. Res. Lett. , 25:4075–4078.
- Hall, C. M., Manson, A. H., and Meek, C. E. (1998). Seasonal variation of the turbopause: One year of turbulence investigation at 69degN by the joint University of Tromsø University of Saskatchewan MF radar. J. Geophys. Res. , 103:28.
- Hall, C. M., Meek, C. E., Manson, A. H., and Nozawa, S. (2008). Turbopause determination, climatology, and climatic trends using medium frequency radars at 52degN and 70degN. Journal of Geophysical Research (Atmospheres), 113(D12):D13104.
- Halliday, A. N. (2013). The origins of volatiles in the terrestrial planets. Geochimica et Cosmochimica Acta, 105:146–171.
- Hartmann, W. K. (1973). Martian cratering, 4, mariner 9 initial analysis of cratering chronology. Journal of Geophysical Research, 78(20):4096–4116.
- Heath, C. and Brain, D. A. (2013). Influence of Asteroid and Comet Impacts on Atmospheric Abundances at Venus, Earth, and Mars. In AAS/Division for Planetary Sciences Meeting Abstracts, volume 45 of AAS/Division for Planetary Sciences Meeting Abstracts, page 118.10.
- Heavens, N., Richardson, M., Lawson, W., Lee, C., McCleese, D., Kass, D., Kleinböhl, A., Schofield, J., Abdou, W., and Shirley, J. (2010). Convective instability in the martian middle atmosphere. Icarus, 208(2):574–589.
- Hocking, W. (2011). A review of mesosphere–stratosphere–troposphere (mst) radar developments and studies, circa 1997–2008. Journal of Atmospheric and Solar-Terrestrial Physics, 73(9):848–882.
- Hodges, R. (1969). Eddy diffusion coefficients due to instabilities in internal gravity waves. Journal of Geophysical Research, 74(16):4087–4090.
- Holmen, S. E., Hall, C. M., and Tsutsumi, M. (2016). Neutral atmosphere temperature trends and variability at 90 km, 70 n, 19 e, 2003–2014. Atmospheric Chemistry and Physics, 16(12):7853–7866.
- Hu, R., Kass, D. M., Ehlmann, B. L., and Yung, Y. L. (2015). Tracing the fate of carbon and the atmospheric evolution of Mars. Nature Communications, 6:10003.

- Hunten, D. M., Pepin, R. O., and Walker, J. C. G. (1987). Mass fractionation in hydrodynamic escape. Icarus , 69:532–549.
- Hutchins, K. and Jakosky, B. (1997). Role of the Crust in the Evolution of the Martian Atmosphere. In Early Mars: Geologic and Hydrologic Evolution, Physical and Chemical Environments, and the Implications for Life, volume 916, page 42.
- Hutchins, K. S. (1998). Coupled Evolution of the Martian Atmosphere and Crust Through Geologic Time. PhD thesis, University of Colorado at Boulder.
- Hutchins, K. S. and Jakosky, B. M. (1996). Evolution of Martian atmospheric argon: Implications for sources of volatiles. J. Geophys. Res. , 101:14933–14950.
- Hynek, B. M., Beach, M., and Hoke, M. R. (2010). Updated global map of martian valley networks and implications for climate and hydrologic processes. Journal of Geophysical Research: Planets, 115(E9).
- Imamura, T., Watanabe, A., and Maejima, Y. (2016). Convective generation and vertical propagation of fast gravity waves on mars: One-and two-dimensional modeling. Icarus, 267:51–63.
- Irwin, R. P., Tanaka, K. L., and Robbins, S. J. (2013). Distribution of early, middle, and late noachian cratered surfaces in the martian highlands: Implications for resurfacing events and processes. Journal of Geophysical Research: Planets, 118(2):278–291.
- Ivanov, B. A. (2001). Mars/moon cratering rate ratio estimates. Space Science Reviews, 96(1-4):87–104.
- Jakosky, B. M. (1991). Mars volatile evolution - Evidence from stable isotopes. Icarus , 94:14–31.
- Jakosky, B. M., Grebowsky, J. M., Luhmann, J. G., and Brain, D. A. (2015a). Initial results from the MAVEN mission to Mars. Geophys. Res. Lett. , 42:8791–8802.
- Jakosky, B. M. and Jones, J. H. (1997). The history of martian volatiles. Reviews of Geophysics, 35(1):1–16.
- Jakosky, B. M., Lin, R. P., Grebowsky, J. M., Luhmann, J. G., Mitchell, D. F., Beutelschies, G., Priser, T., Acuna, M., Andersson, L., Baird, D., Baker, D., Bartlett, R., Benna, M., Bougher, S., Brain, D., Carson, D., Cauffman, S., Chamberlin, P., Chaufray, J.-Y., Cheatom, O., Clarke, J., Connerney, J., Cravens, T., Curtis, D., Delory, G., Demcak, S., DeWolfe, A., Eparvier, F., Ergun, R., Eriksson, A., Espley, J., Fang, X., Folta, D., Fox, J., Gomez-Rosa, C., Habenicht, S., Halekas, J., Holsclaw, G., Houghton, M., Howard, R., Jarosz, M., Jedrich, N., Johnson, M., Kasprzak, W., Kelley, M., King, T., Lankton, M., Larson, D., Leblanc, F., Lefevre, F., Lillis, R., Mahaffy, P., Mazelle, C., McClintock, W., McFadden, J., Mitchell, D. L., Montmessin, F., Morrissey, J., Peterson, W., Possel, W., Sauvaud, J.-A., Schneider, N., Sidney, W., Sparacino, S., Stewart, A. I. F., Tolson, R., Toubanc, D., Waters, C., Woods, T., Yelle, R., and Zurek, R. (2015b). The Mars Atmosphere and Volatile Evolution (MAVEN) Mission. Space Sci. Rev. , 195:3–48.
- Jakosky, B. M., Pepin, R. O., Johnson, R. E., and Fox, J. L. (1994). Mars atmospheric loss and isotopic fractionation by solar-wind-induced sputtering and photochemical escape. Icarus , 111:271–288.

- Jakosky, B. M. and Phillips, R. J. (2001). Mars' volatile and climate history. *Nature*, 412:237–244.
- Jakosky, B. M. and Shock, E. L. (1998). The biological potential of Mars, the early Earth, and Europa. *J. Geophys. Res.*, 103:19359–19364.
- Jakosky, B. M., Slipski, M., Benna, M., Mahaffy, P., Elrod, M., Yelle, R., Stone, S., and Alsaeed, N. (2017). Mars' atmospheric history derived from upper-atmosphere measurements of $^{38}\text{Ar}/^{36}\text{Ar}$. *Science*, 355:1408–1410.
- John, S. R. and Kishore Kumar, K. (2012). The concept of wave-turbopause layer and its signature in the global mesosphere-lower thermospheric gravity wave activity. *Journal of Geophysical Research (Space Physics)*, 117(A16):A10310.
- Johnson, R. and Luhmann, J. (1998). Sputter contribution to the atmospheric corona on Mars. *Journal of Geophysical Research: Planets (1991–2012)*, 103(E2):3649–3653.
- Johnson, S. S., Mischna, M. A., Grove, T. L., and Zuber, M. T. (2008). Sulfur-induced greenhouse warming on early Mars. *Journal of Geophysical Research (Planets)*, 113:8005.
- Joussaume, S., Sadourny, R., and Jouzel, J. (1984). A general circulation model of water isotope cycles in the atmosphere. *Nature*, 311(5981):24.
- Jouzel, J., Merlivat, L., Petit, J.-R., and Lorius, C. (1983). Climatic information over the last century deduced from a detailed isotopic record in the south pole snow. *Journal of Geophysical Research: Oceans*, 88(C4):2693–2703.
- Kendall, C. and Caldwell, E. A. (1998). Fundamentals of isotope geochemistry. In *Isotope tracers in catchment hydrology*, pages 51–86. Elsevier.
- Kleinböhl, A., John Wilson, R., Kass, D., Schofield, J. T., and McCleese, D. J. (2013). The semidiurnal tide in the middle atmosphere of Mars. *Geophys. Res. Lett.*, 40:1952–1959.
- Kleinböhl, A., Schofield, J. T., Abdou, W. A., Irwin, P. G. J., and de Kok, R. J. (2011). A single-scattering approximation for infrared radiative transfer in limb geometry in the Martian atmosphere. *J. Quant. Spec. Radiat. Transf.*, 112:1568–1580.
- Kleinböhl, A., Schofield, J. T., Kass, D. M., Abdou, W. A., Backus, C. R., Sen, B., Shirley, J. H., Lawson, W. G., Richardson, M. I., Taylor, F. W., Teanby, N. A., and McCleese, D. J. (2009). Mars Climate Sounder limb profile retrieval of atmospheric temperature, pressure, and dust and water ice opacity. *Journal of Geophysical Research (Planets)*, 114(E13):E10006.
- Krasnopolsky, V. A., Mumma, M. J., and Randall Gladstone, G. (1998). Detection of Atomic Deuterium in the Upper Atmosphere of Mars. *Science*, 280:1576.
- Kurokawa, H., Usui, T., and Sato, M. (2015). Interactive Evolution of Multiple Water-Ice Reservoirs on Mars: Insights from Hydrogen Isotope Compositions. *ArXiv e-prints*.
- Lammer, H., Chassefière, E., Karatekin, Ö., Morschhauser, A., Niles, P. B., Mousis, O., Odert, P., Möstl, U. V., Breuer, D., Dehant, V., Grott, M., Gröller, H., Hauber, E., and Pham, L. B. S. (2013). Outgassing History and Escape of the Martian Atmosphere and Water Inventory. *Space Sci. Rev.*, 174:113–154.

- Laskar, J., Correia, A., Gastineau, M., Joutel, F., Levrard, B., and Robutel, P. (2004). Long term evolution and chaotic diffusion of the insolation quantities of mars. *Icarus*, 170(2):343–364.
- Leblanc, F., Chassefière, E., Gillmann, C., and Breuer, D. (2012). Mars' atmospheric ^{40}Ar : A tracer for past crustal erosion. *Icarus*, 218:561–570.
- Leblanc, F. and Johnson, R. E. (2002). Role of molecular species in pickup ion sputtering of the Martian atmosphere. *Journal of Geophysical Research (Planets)*, 107:5010.
- Leblanc, F., Modolo, R., Curry, S., Luhmann, J., Lillis, R., Chaufray, J.-Y., Hara, T., Mcfadden, J., Halekas, J., Eparvier, F., et al. (2015). Mars heavy ion precipitating flux as measured by mars atmosphere and volatile evolution. *Geophysical Research Letters*, 42(21):9135–9141.
- Lee, J.-Y., Marti, K., Severinghaus, J. P., Kawamura, K., Yoo, H.-S., Lee, J. B., and Kim, J. S. (2006). A redetermination of the isotopic abundances of atmospheric Ar. *Geochim. Cosmochim. Acta*, 70:4507–4512.
- Lehmacher, G. A., Scott, T. D., Larsen, M. F., Bilén, S. G., Croskey, C. L., Mitchell, J. D., Rapp, M., Lübken, F.-J., and Collins, R. L. (2011). The Turbopause experiment: atmospheric stability and turbulent structure spanning the turbopause altitude. *Annales Geophysicae*, 29:2327–2339.
- Leovy, C. B. (1982). Control of the homopause level. *Icarus*, 50(2-3):311–321.
- Lewkow, N. and Kharchenko, V. (2014). Precipitation of energetic neutral atoms and induced non-thermal escape fluxes from the martian atmosphere. *The Astrophysical Journal*, 790(2):98.
- Lillis, R. J., Brain, D. A., Bougher, S. W., Leblanc, F., Luhmann, J. G., Jakosky, B. M., Modolo, R., Fox, J., Deighan, J., Fang, X., et al. (2015). Characterizing atmospheric escape from mars today and through time, with maven. *Space Science Reviews*, 195(1-4):357–422.
- Lillis, R. J., Frey, H. V., Manga, M., Mitchell, D. L., Lin, R. P., Acuña, M. H., and Bougher, S. W. (2008). An improved crustal magnetic field map of Mars from electron reflectometry: Highland volcano magmatic history and the end of the martian dynamo. *Icarus*, 194:575–596.
- Lindzen, R. S. (1981). Turbulence and stress owing to gravity wave and tidal breakdown. *Journal of Geophysical Research: Oceans*, 86(C10):9707–9714.
- Liu, G., England, S., Lillis, R. J., Mahaffy, P. R., Elrod, M., Benna, M., and Jakosky, B. (2017). Longitudinal structures in mars' upper atmosphere as observed by maven/ngims. *Journal of Geophysical Research: Space Physics*, 122(1):1258–1268.
- Luhmann, J. G., Johnson, R. E., and Zhang, M. H. G. (1992). Evolutionary impact of sputtering of the Martian atmosphere by O(+) pickup ions. *Geophys. Res. Lett.*, 19:2151–2154.
- Lundin, R., Barabash, S., Holmström, M., Nilsson, H., Yamauchi, M., Dubinin, E., and Fraenz, M. (2009). Atmospheric origin of cold ion escape from Mars. *Geophysical Research Letters*, 36(17).
- Magalhães, J. A., Schofield, J. T., and Seiff, A. (1999). Results of the Mars Pathfinder atmospheric structure investigation. *J. Geophys. Res.*, 104:8943–8956.
- Mahaffy, P. R., Benna, M., Elrod, M., Yelle, R. V., Bougher, S. W., Stone, S. W., and Jakosky, B. M. (2015a). Structure and composition of the neutral upper atmosphere of Mars from the MAVEN NGIMS investigation. *Geophys. Res. Lett.*, 42:8951–8957.

- Mahaffy, P. R., Benna, M., King, T., Harpold, D. N., Arvey, R., Barciniak, M., Bendt, M., Carrigan, D., Errigo, T., Holmes, V., Johnson, C. S., Kellogg, J., Kimvilakani, P., Lefavor, M., Hengemihle, J., Jaeger, F., Lyness, E., Maurer, J., Melak, A., Noreiga, F., Noriega, M., Patel, K., Prats, B., Raaen, E., Tan, F., Weidner, E., Gundersen, C., Battel, S., Block, B. P., Arnett, K., Miller, R., Cooper, C., Edmonson, C., and Nolan, J. T. (2015b). The Neutral Gas and Ion Mass Spectrometer on the Mars Atmosphere and Volatile Evolution Mission. *Space Sci. Rev.*, 195:49–73.
- Mahaffy, P. R., Niemann, H. B., Alpert, A., Atreya, S. K., Demick, J., Donahue, T. M., Harpold, D. N., and Owen, T. C. (2000). Noble gas abundance and isotope ratios in the atmosphere of Jupiter from the Galileo Probe Mass Spectrometer. *J. Geophys. Res.*, 105:15061–15072.
- Mahaffy, P. R., Webster, C. R., Atreya, S. K., Franz, H., Wong, M., Conrad, P. G., Harpold, D., Jones, J. J., Leshin, L. A., Manning, H., and et al. (2013). Abundance and Isotopic Composition of Gases in the Martian Atmosphere from the Curiosity Rover. *Science*, 341:263–266.
- Mahaffy, P. R., Webster, C. R., Atreya, S. K., Franz, H., Wong, M., Conrad, P. G., Harpold, D., Jones, J. J., Leshin, L. A., Manning, H., et al. (2013). Abundance and isotopic composition of gases in the martian atmosphere from the curiosity rover. *Science*, 341(6143):263–266.
- Malin, M. C., Edgett, K. S., Posiolova, L. V., McColley, S. M., and Dobra, E. Z. N. (2006). Present-day impact cratering rate and contemporary gully activity on mars. *science*, 314(5805):1573–1577.
- Martin, H., Albarède, F., Claeys, P., Gargaud, M., Marty, B., Morbidelli, A., and Pinti, D. L. (2006). From Suns to Life: A Chronological Approach to the History of Life on Earth 4. Building of a Habitable Planet. *Earth Moon and Planets*, 98:97–151.
- Marty, B. (2012). The origins and concentrations of water, carbon, nitrogen and noble gases on Earth. *Earth and Planetary Science Letters*, 313:56–66.
- McCleese, D. and Schofield, J., editors (2006). *Mars Reconnaissance Orbiter Mars Climate Sounder Derived Data Record Version 4*, volume MROM.2102-MROM.2122. NASA Planetary Data System.
- McCleese, D., Schofield, J., Taylor, F., Abdou, W., Aharonson, O., Banfield, D., Calcutt, S., Heavens, N., Irwin, P., Kass, D., et al. (2008). Intense polar temperature inversion in the middle atmosphere on mars. *Nature Geoscience*, 1(11):745.
- McCleese, D. J., Schofield, J. T., Taylor, F. W., Calcutt, S. B., Foote, M. C., Kass, D. M., Leovy, C. B., Paige, D. A., Read, P. L., and Zurek, R. W. (2007). Mars Climate Sounder: An investigation of thermal and water vapor structure, dust and condensate distributions in the atmosphere, and energy balance of the polar regions. *Journal of Geophysical Research (Planets)*, 112:E05S06.
- McDonough, W. F. and Sun, S.-S. (1995). The Composition of the Earth. *Chemical Geology*, 120(3):223–253.
- McElroy, M. B., Kong, T. Y., and Yung, Y. L. (1977). Photochemistry and evolution of mars' atmosphere: A viking perspective. *Journal of Geophysical Research*, 82(28):4379–4388.
- McElroy, M. B. and Yung, Y. L. (1976). Isotopic composition of the martian atmosphere. *Science*, 194(4260):68–70.

- McKeown, N. K., Bishop, J. L., Noe Dobrea, E. Z., Ehlmann, B. L., Parente, M., Mustard, J. F., Murchie, S. L., Swayze, G. A., Bibring, J.-P., and Silver, E. A. (2009). Characterization of phyllosilicates observed in the central mawrth vallis region, mars, their potential formational processes, and implications for past climate. Journal of Geophysical Research: Planets, 114(E2).
- Medvedev, A. S. and Klaassen, G. P. (2003). Thermal effects of saturating gravity waves in the atmosphere. Journal of Geophysical Research (Atmospheres), 108:4040.
- Medvedev, A. S. and Yiğit, E. (2012). Thermal effects of internal gravity waves in the Martian upper atmosphere. Geophys. Res. Lett., 39:L05201.
- Medvedev, A. S., Yiğit, E., Hartogh, P., and Becker, E. (2011). Influence of gravity waves on the Martian atmosphere: General circulation modeling. Journal of Geophysical Research (Planets), 116(E15):E10004.
- Melosh, H. J. and Vickery, A. M. (1989). Impact erosion of the primordial atmosphere of Mars. Nature, 338:487–489.
- Michalski, J. R. and Niles, P. B. (2010). Deep crustal carbonate rocks exposed by meteor impact on mars. Nature Geoscience, 3(11):751.
- Millour, E., Forget, F., Lopez-Valverde, M., Lefevre, F., Gonzalez-Galindo, F., Lewis, S., Chaufray, J.-Y., Montabone, L., Zakharov, V., Spiga, A., et al. (2018). Exploring the interannual variability of the martian atmosphere with the mars climate database v5. 3. In 42nd COSPAR Scientific Assembly, volume 42.
- Millour, E., Forget, F., Spiga, A., Navarro, T., Madeleine, J.-B., Montabone, L., Pottier, A., Lefèvre, F., Montmessin, F., Chaufray, J.-Y., et al. (2015). The mars climate database (mcd version 5.2). In European Planetary Science Congress 2015, volume 10, pages EPSC2015–438. EPSC.
- Montmessin, F., Smith, M. D., Langevin, Y., Mellon, M. T., and Fedorova, A. (2017). The water cycle. The Atmosphere and Climate of Mars, 18:338.
- Morris, R. V., Ruff, S. W., Gellert, R., Ming, D. W., Arvidson, R. E., Clark, B. C., Golden, D., Siebach, K., Klingelhöfer, G., Schröder, C., et al. (2010). Identification of carbonate-rich outcrops on mars by the spirit rover. Science, page 1189667.
- Morschhauser, A., Grott, M., and Breuer, D. (2011). Crustal recycling, mantle dehydration, and the thermal evolution of Mars. Icarus, 212:541–558.
- Nier, A. O. and McElroy, M. B. (1977). Composition and structure of Mars' upper atmosphere - Results from the neutral mass spectrometers on Viking 1 and 2. J. Geophys. Res., 82:4341–4349.
- Offermann, D., Friedrich, V., Ross, P., and von Zahn, U. (1981). Neutral gas composition measurements between 80 and 120 km. Planet. Space Sci., 29:747–764.
- Offermann, D., Jarisch, M., Oberheide, J., Gusev, O., Wohltmann, I., Russell, J. M., and Mlynczak, M. G. (2006). Global wave activity from upper stratosphere to lower thermosphere: A new turbopause concept. Journal of Atmospheric and Solar-Terrestrial Physics, 68:1709–1729.

- Offermann, D., Jarisch, M., Schmidt, H., Oberheide, J., Grossmann, K. U., Gusev, O., Russell, III, J. M., and Mlynczak, M. G. (2007). The “wave turbopause”. Journal of Atmospheric and Solar-Terrestrial Physics, 69:2139–2158.
- Owen, T., Biemann, K., Biller, J. E., Laffleur, A. L., Rushneck, D. R., and Howarth, D. W. (1977). The composition of the atmosphere at the surface of Mars. J. Geophys. Res. , 82:4635–4639.
- Ozima, M. and Podosek, F. (2002). Noble Gas Geochemistry. Cambridge University Press.
- Parker, T. J., Gorsline, D. S., Saunders, R. S., Pieri, D. C., and Schneeberger, D. M. (1993). Coastal geomorphology of the martian northern plains. Journal of Geophysical Research: Planets, 98(E6):11061–11078.
- Pepin, R. O. (1991). On the origin and early evolution of terrestrial planet atmospheres and meteoritic volatiles. Icarus , 92:2–79.
- Pepin, R. O. (1994). Evolution of the martian atmosphere. Icarus , 111:289–304.
- Pepin, R. O. (2006). Atmospheres on the terrestrial planets: Clues to origin and evolution. Earth and Planetary Science Letters, 252(1-2):1–14.
- Pepin, R. O., Schlutter, D. J., Becker, R. H., and Reisenfeld, D. B. (2012). Helium, neon, and argon composition of the solar wind as recorded in gold and other Genesis collector materials. Geochim. Cosmochim. Acta , 89:62–80.
- Pham, L., Karatekin, Ö., and Dehant, V. (2011). Effects of impacts on the atmospheric evolution: Comparison between Mars, Earth, and Venus. Planetary and Space Science, 59(10):1087–1092.
- Pham, L. B. S., Karatekin, Ö., and Dehant, V. (2009). Effects of Meteorite Impacts on the Atmospheric Evolution of Mars. Astrobiology, 9:45–54.
- Pollack, J. B., Kasting, J. F., Richardson, S. M., and Poliakov, K. (1987). The case for a wet, warm climate on early Mars. Icarus , 71:203–224.
- Preusse, P., Ern, M., Eckermann, S. D., Warner, C. D., Picard, R. H., Knieling, P., Krebsbach, M., Russell III, J. M., Mlynczak, M. G., Mertens, C. J., et al. (2006). Tropopause to mesopause gravity waves in august: Measurement and modeling. Journal of atmospheric and solar-terrestrial physics, 68(15):1730–1751.
- Pujol, M., Marty, B., Burgess, R., Turner, G., and Philippot, P. (2013). Argon Isotopic Composition of Archaean Atmosphere Probes Early Earth Geodynamics. Nature, 498(7452):87–90.
- Ramirez, R. M. R., Kopparapu, R. K., Zuger, M. E. Z., Robinson, T. D. R., Freedman, R. F., and Kasting, J. F. K. (2014). Warming Early Mars with CO₂ and H₂. NatGeo, 7:59–63.
- Rapp, M., Strelnikov, B., Müllemann, A., Lübken, F.-J., and Fritts, D. (2004). Turbulence measurements and implications for gravity wave dissipation during the macwave/midas rocket program. Geophysical research letters, 31(24).
- Ribas, I., Guinan, E. F., Güdel, M., and Audard, M. (2005). Evolution of the Solar Activity over Time and Effects on Planetary Atmospheres. I. High-Energy Irradiances (1-1700 Å). ApJ , 622:680–694.

- Robbins, S. J. and Hynek, B. M. (2012). A new global database of Mars impact craters >1 km: 1. Database creation, properties, and parameters. Journal of Geophysical Research (Planets), 117:5004.
- Rodriguez, J. A., Sasaki, S., Kuzmin, R. O., Dohm, J. M., Tanaka, K. L., Miyamoto, H., Kurita, K., Komatsu, G., Fairén, A., and Ferris, J. C. (2005). Outflow channel sources, reactivation, and chaos formation, xanthe terra, mars. Icarus, 175(1):36–57.
- Rodriguez, J. A. P., Fairén, A. G., Tanaka, K. L., Zarroca, M., Linares, R., Platz, T., Komatsu, G., Miyamoto, H., Kargel, J. S., Yan, J., et al. (2016). Tsunami waves extensively resurfaced the shorelines of an early martian ocean. Scientific reports, 6:25106.
- Rodriguez, J. A. P., Kargel, J. S., Baker, V. R., Gulick, V. C., Berman, D. C., Fairén, A. G., Linares, R., Zarroca, M., Yan, J., Miyamoto, H., et al. (2015). Martian outflow channels: How did their source aquifers form, and why did they drain so rapidly? Scientific reports, 5:13404.
- Sagan, C. and Mullen, G. (1972). Earth and mars: evolution of atmospheres and surface temperatures. Science, 177(4043):52–56.
- Schneider, A., Wagner, J., Söder, J., Gerding, M., and Lübken, F.-J. (2017). Case study of wave breaking with high-resolution turbulence measurements with litos and wrf simulations. Atmospheric Chemistry and Physics, 17(12):7941.
- Schoeberl, M. R. and Strobel, D. F. (1984). Nonzonal gravity wave breaking in the winter mesosphere. Dynamics of the Middle Atmosphere, pages 45–64.
- Schofield, J., Barnes, J. R., Crisp, D., Haberle, R. M., Larsen, S., Magalhaes, J., Murphy, J. R., Seiff, A., and Wilson, G. (1997). The mars pathfinder atmospheric structure investigation/meteorology (asi/met) experiment. Science, 278(5344):1752–1758.
- Segura, T. L., Toon, O. B., Colaprete, A., and Zahnle, K. (2002). Environmental Effects of Large Impacts on Mars. Science, 298:1977–1980.
- Sephton, M., Verchovsky, A., Bland, P., Gilmour, I., Grady, M., and Wright, I. (2003). Investigating the variations in carbon and nitrogen isotopes in carbonaceous chondrites. Geochimica et Cosmochimica Acta, 67(11):2093–2108.
- Shuvalov, V. (2009). Atmospheric erosion induced by oblique impacts. Meteoritics and Planetary Science, 44:1095–1105.
- Shuvalov, V. and Artemieva, N. A. (2002). Atmospheric Erosion and Radiation Impulse Induced by Impacts. Geological Society of America Special Papers, 356:695–703.
- Sleep, N. H. (1994). Martian plate tectonic. Journal of Geophysical Research, 99(E3):5639–5655.
- Sleep, N. H. and Zahnle, K. (2001). Carbon dioxide cycling and implications for climate on ancient earth. Journal of Geophysical Research: Planets, 106(E1):1373–1399.
- Sleep, N. H., Zahnle, K. J., Kasting, J. F., and Morowitz, H. J. (1989). Annihilation of ecosystems by large asteroid impacts on the early Earth. Nature, 342(6246):139–142.
- Slipski, M. and Jakosky, B. M. (2016). Argon isotopes as tracers for martian atmospheric loss. Icarus, 272:212–227.

- Smith, M. D., Bougher, S. W., Encrenaz, T., Forget, F., and Kleinbohl, A. (2017). Thermal structure and composition. The Atmosphere and Climate of Mars, 18:42.
- Snowden, D., Yelle, R. V., Cui, J., Wahlund, J.-E., Edberg, N. J. T., and Ågren, K. (2013). The thermal structure of Titan's upper atmosphere, I: Temperature profiles from Cassini INMS observations. Icarus, 226:552–582.
- Spiga, A., González-Galindo, F., López-Valverde, M.-Á., and Forget, F. (2012). Gravity waves, cold pockets and co₂ clouds in the martian mesosphere. Geophysical Research Letters, 39(2).
- Spinrad, H., Münch, G., and Kaplan, L. D. (1963). Letter to the editor: the detection of water vapor on mars. The Astrophysical Journal, 137:1319.
- Stewart, S. T. and Valiant, G. J. (2006). Martian subsurface properties and crater formation processes inferred from fresh impact crater geometries. Meteoritics and Planetary Science, 41:1509–1537.
- Stone, S. W., Yelle, R. V., Benna, M., Elrod, M. K., and Mahaffy, P. R. (2015). Thermal structure of the martian upper atmosphere from maven ngims. Journal of Geophysical Research: Planets.
- Svetsov, V. V. (2007). Atmospheric erosion and replenishment induced by impacts of cosmic bodies upon the Earth and Mars. Solar System Research, 41:28–41.
- Svetsov, V. V. (2000). On the Efficiency of the Impact Mechanism of Atmospheric Erosion. Solar System Research, 34:398.
- Tanaka, K. L., Isbell, N. K., Scott, D. H., Greeley, R., and Guest, J. E. (1988). The resurfacing history of Mars - A synthesis of digitized, viking-based geology. In Ryder, G., editor, Lunar and Planetary Science Conference Proceedings, volume 18 of Lunar and Planetary Science Conference Proceedings, pages 665–678.
- Tanaka, K. L., Robbins, S. J., Fortezzo, C. M., Skinner, J. A., and Hare, T. M. (2014). The digital global geologic map of Mars: Chronostratigraphic ages, topographic and crater morphologic characteristics, and updated resurfacing history. Planet. Space Sci., 95:11–24.
- Terada, N., Leblanc, F., Nakagawa, H., Medvedev, A. S., Yiğit, E., Kuroda, T., Hara, T., England, S. L., Fujiwara, H., Terada, K., et al. (2017). Global distribution and parameter dependences of gravity wave activity in the martian upper thermosphere derived from maven/ngims observations. Journal of Geophysical Research: Space Physics, 122(2):2374–2397.
- Tian, F., Chassefière, E., Leblanc, F., and Brain, D. (2013). Atmospheric Escape and Climate Evolution of Terrestrial Planets, pages 567–581.
- Torgersen, T. (1989). Terrestrial Helium Degassing Fluxes and the Atmospheric Helium Budget: Implications with Respect to the Degassing Processes of Continental Crust. Chemical Geology: Isotope Geoscience section, 79(1):1–14.
- Vaille, A., Tenishev, V., Bougher, S. W., Combi, M. R., and Nagy, A. F. (2009). Three-dimensional study of Mars upper thermosphere/ionosphere and hot oxygen corona: 1. General description and results at equinox for solar low conditions. Journal of Geophysical Research (Planets), 114(E13):E11005.

- Vlasov, M. and Kelley, M. (2010). Estimates of eddy turbulence consistent with seasonal variations of atomic oxygen and its possible role in the seasonal cycle of mesopause temperature. In Annales Geophysicae, volume 28, page 2103. Copernicus GmbH.
- Vogel, N., Heber, V. S., Baur, H., Burnett, D. S., and Wieler, R. (2011). Argon, krypton, and xenon in the bulk solar wind as collected by the Genesis mission. Geochim. Cosmochim. Acta , 75:3057–3071.
- Wallis, M. K. (1989). C, n, o isotope fractionation on mars: Implications for crustal h₂o and snc meteorites. Earth and planetary science letters, 93(3-4):321–324.
- Walterscheid, R. (1981). Dynamical cooling induced by dissipating internal gravity waves. Geophysical Research Letters, 8(12):1235–1238.
- Wang, Y.-C., Luhmann, J. G., Fang, X., Leblanc, F., Johnson, R. E., Ma, Y., and Ip, W.-H. (2014). Statistical studies on Mars atmospheric sputtering by precipitating pickup O⁺: Preparation for the MAVEN mission. Journal of Geophysical Research: Planets.
- Wanke, H. and Dreibus, G. (1994). Chemistry and Accretion History of Mars. Philosophical Transactions of the Royal Society of London Series A, 349:285–293.
- Watson, E. B., Thomas, J. B., and Cherniak, D. J. (2007). ⁴⁰Ar retention in the terrestrial planets. Nature , 449:299–304.
- Webster, C. R., Mahaffy, P. R., Flesch, G. J., Niles, P. B., Jones, J. H., Leshin, L. A., Atreya, S. K., Stern, J. C., Christensen, L. E., Owen, T., Franz, H., Pepin, R. O., Steele, A., and aff9 (2013). Isotope Ratios of H, C, and O in CO₂ and H₂O of the Martian Atmosphere. Science, 341:260–263.
- Werner, S. C. (2009). The global martian volcanic evolutionary history. Icarus , 201:44–68.
- Wilhelms, D. E. and Squyres, S. W. (1984). The martian hemispheric dichotomy may be due to a giant impact. Nature, 309(5964):138.
- Wong, M. H., Atreya, S. K., Mahaffy, P. N., Franz, H. B., Malespin, C., Trainer, M. G., Stern, J. C., Conrad, P. G., Manning, H. L., Pepin, R. O., et al. (2013). Isotopes of nitrogen on Mars: Atmospheric measurements by Curiosity's mass spectrometer. Geophysical Research Letters, 40(23):6033–6037.
- Wordsworth, R. D. (2016). The climate of early mars. Annual Review of Earth and Planetary Sciences, 44:381–408.
- Wright, C. J. (2012). A one-year seasonal analysis of martian gravity waves using mcs data. Icarus, 219(1):274–282.
- Yiğit, E., Aylward, A. D., and Medvedev, A. S. (2008). Parameterization of the effects of vertically propagating gravity waves for thermosphere general circulation models: Sensitivity study. Journal of Geophysical Research: Atmospheres, 113(D19).
- Yiğit, E., England, S. L., Liu, G., Medvedev, A. S., Mahaffy, P. R., Kuroda, T., and Jakosky, B. M. (2015). High-altitude gravity waves in the Martian thermosphere observed by MAVEN/NGIMS and modeled by a gravity wave scheme. Geophys. Res. Lett. , 42:8993–9000.

- Yiğit, E. and Medvedev, A. S. (2009). Heating and cooling of the thermosphere by internal gravity waves. Geophys. Res. Lett. , 36:L14807.
- Zahnle, K. (1993). Planetary noble gases. In Levy, E. H. and Lunine, J. I., editors, Protostars and Planets III, pages 1305–1338.
- Zahnle, K. and Sleep, N. (1997). Impacts and the early evolution of life. In Comets and the Origin and Evolution of Life, pages 175–208. Springer.
- Zahnle, K. J. (1990). Atmospheric Chemistry by Large Impacts. Geological Society of America Special Papers, 247:271–288.
- Zahnle, K. J. and Walker, J. C. G. (1982). The evolution of solar ultraviolet luminosity. Reviews of Geophysics and Space Physics, 20:280–292.
- Zhang, M. H. G., Luhmann, J. G., Bougher, S. W., and Nagy, A. F. (1993). The ancient oxygen exosphere of Mars - Implications for atmosphere evolution. J. Geophys. Res. , 98:10915.
- Zhong, S. and Zuber, M. T. (2001). Degree-1 mantle convection and the crustal dichotomy on mars. Earth and Planetary Science Letters, 189(1-2):75–84.
- Zurek, R., Tolson, R., Bougher, S., Lugo, R., Baird, D., Bell, J., and Jakosky, B. (2017). Mars thermosphere as seen in maven accelerometer data. Journal of Geophysical Research: Space Physics, 122(3):3798–3814.